Università degli Studi di Cagliari

DOTTORATO DI RICERCA

Ingegneria Civile, Ambientale e Architettura

Ciclo XXX

TITOLO TESI

Flexural Wave Propagation in Microstructured Media. Perfectly Matched Layers and Elastic Metamaterials.

Settore/i scientifico disciplinari di afferenza

Ingegneria Civile, Ambientale e Architettura

Presentata da:	Maryam MORVARIDI
Coordinatore Dottorato:	Prof. Roberto DEIDDA
Tutor:	Prof. Michele BRUN
Co-Tutor:	Dr. Eng. Giorgio CARTA

Esame finale anno accademico 2016 – 2017
Tesi discussa nella sessione d'esame Marzo 2018

Declaration of Authorship

I, Eng. Maryam MORVARIDI, declare that this thesis titled, 'Flexural Wave Propagation in Microstructured Media. Perfectly Matched Layers and Elastic Metamaterials.' and the work presented in it are my own. I confirm that:

- This work was done wholly or mainly while in candidature for a research degree at this University.
- Where any part of this thesis has previously been submitted for a degree or any other qualification at this University or any other institution, this has been clearly stated.
- Where I have consulted the published work of others, this is always clearly attributed.
- Where I have quoted from the work of others, the source is always given. With the exception of such quotations, this thesis is entirely my own work.
- I have acknowledged all main sources of help.
- Where the thesis is based on work done by myself jointly with others, I have made clear exactly what was done by others and what I have contributed myself.

Signed: Maryam Morvaridi

Date: 14/02/2018

Acknowledgements

Firstly, I would like to express my sincere gratitude to my advisor Prof. Michele Brun for the continuous support of my Ph.D study and related research, for his patience, motivation, and immense knowledge. His guidance helped me in all the time of research and writing of this thesis. I could not have imagined having a better advisor and mentor for my Ph.D study.

My sincere thanks also goes to Dr.Giorgio Carta, who provided me supports and guidance in research field.

The financial support of Regione Autonoma della Sardegna, project NAMEFOAMS "Fabrication, characterization and modeling of NAnoporous MEtal FOAMS", CUP F72F16003180002, is gratefully acknowledged.

Last but not the least, I would like to thank my family: my parents and to my sister for supporting me spiritually throughout doing Ph.D and writing this thesis and my life in general. ...

Contents

List of Figures

List of Tables

Symbols

Roman symbols

Symbol	Name	Unit
A	Cross-sectional area of the beam	$[m^2]$
$G(X)$	Coordinate transformation	
E	Young's modulus of the material	$[N/m^2]$
n	Axial force in beam structure	$[N]$
p	Axial force in plate structure	$[N]$
M	Bending moment in the structure	[Nm]
$\mathbf{M}$	Bending moment tensor in the structure	[Nm]
r	Vertical force in beam structure	$[N]$
R	Vertical force in plate structure	$[N]$
B	Bending stiffness in plate structure	$[Nm]$
$\overline{EA}$	Nonhomogenous linear stiffness of the beam structure	$[Nm]$
h	Thickness of plate structure	$[m]$
J	Moment of inertia of beam structure	$[m^4]$
$U(X)$	Longitudinal displacement of rod structure before transformation	$[m]$
$u(x)$	Longitudinal displacement of rod structure after transformation	$[m]$
$V(X)$	Transverse displacement of beam structure before transformation	$[m]$
$v(x)$	Transverse displacement of beam structure after transformation	$[m]$
$W(X)$	Transverse displacement of plate structure before transformation	$[m]$
$w(x)$	Transverse displacement of plate structure after transformation	$[m]$
$\mathbb{D}^{(0)}$	Constituitive tensor in plate structure	$[Nm]$
F	Transformation gradient in plate structure	
V	Transverse force vector in single resonator	$[N]$
a	Dimension of single resonator unit cell	$[m]$
R_0	Circular inclusion radius of single resonator	$[m]$

R_1	Central hole radius of single resonator	$[m]$
s	Thickness of slender spiral	$[m]$
$y(\theta)$	Radial position of spiral	$[m]$
$C(\theta)$	Parametric form of spiral	$[m]$
L	Length of spiral	$[m]$
$\mathbf{k}$	Wave number vector	$[m]$
$M_b^{(1)}$	Bending component of moment in single resonator	$[Nm]$
$M_t^{(1)}$	Torsional component of moment in single resonator	$[Nm]$
I_p	Polar moment of inertia of the spiral	$[mm^4]$
I	Second moment of inertia of the spiral	$[mm^4]$
A^*	Shear area of the spiral	$[mm^2]$

Greek symbols

Symbol	Name	Unit
β	Frequency parameter	$[m^{-1}]$
ρ	Non homogenous mass density of plate structure	$[kg/m^3]$
ω	Radian frequency	$[rad/sec]$
ϱ	Homogenous density of rod, beam and plate structure	$[kg/m^3]$
Φ_N	Normal rotation component of plate structure	$[rad]$
$\overline{\rho A}$	Non homogenous linear density of the beam structure	$[kg/m^2]$
$\bar{\omega}_{\alpha_1\alpha_2}$	Numerical natural frequencies of plate structure	$[rad/sec]$
$\omega_{\alpha_1\alpha_2}$	Analytical natural frequencies of plate structure	$[rad/sec]$
ω_1	Corresponding transverse radian frequency of single resonator	$[rad/sec]$
ω_2	Corresponding rotational radian frequency of single resonator	$[rad/sec]$
ω_3	Corresponding rotational radian frequency of single resonator	$[rad/sec]$
$\bar{\theta}$	Total angular distribution of spiral	$[rad]$
$\eta(x_i)$	Transformation function in plate structure	
$\overline{\eta}(x_i)$	Perfectly Matched Layer function in plate structure	
ξ	Relative dimension of Perfectly Matched Layer	
ζ	Normalized physical dimension of Perfectly Matched Layer	
γ	Exponent of the imaginary part of Perfectly Matched Layer transformation	
$\mathcal{Q}$	Quantitative description of performance of PML	

Preface

The work is divided into two main topics. In the first part a formulation for Perfectly Matched Layers is given. Surprisingly, such formulation was absent in the scientific literature. In the second part a new type of periodic plate is proposed.

In particular, an analytical model of Perfectly Matched Layers (PMLs) for flexural waves within elongated beam structures is given. The model is based on transformation optics techniques and it is efficient both in time harmonic and transient regimes. A comparison between flexural and longitudinal waves is detailed and it is shown that the bending problem requires special interface conditions. A connection with transformation of eigenfrequencies and eigenmodes is given and the effect of the additional boundary conditions introduced at the border of the Perfectly Matched Layer domain is discussed in detail. Such a model is particularly useful for Finite Element analyses pertaining propagating flexural waves in infinite domain.

Then, Perfectly Matched Layers for flexural waves are extended to plate structures. Again, the analytical model is based on transformation optics techniques applied on the biharmonic fourth-order partial differential equation describing flexural vibrations in Kirchhoff-Love plates. It is shown that perfect boundary conditions are not an optimal solution, since they depend on the incident waves. The full analytical form of PMLs and zero reflection conditions at the boundary between homogeneous and PML domains are given. The implementation in a Finite Element (FEM) code is described and an eigenfrequency analysis is given as a possible methodology to check the implementation. A measure of the performance of the PMLs is introduced and the effects of element discretization, boundary conditions, frequency, dimension of the PML, amount of transformation and dissipation are detailed. The model gives excellent results also when the applied load approaches the PML domain.

In the last part of the work we propose a new type of *platonic crystal*. The microstructured plate includes snail resonators with low-frequency resonant vibrations. The special dynamic effect of the resonators are highlighted by a comparative analysis of dispersion properties of homogeneous and perforated plates. Analytical and numerical estimates of classes of standing waves are given and the analysis on a macrocell shows the possibility to obtain localization, wave trapping and edge waves. Applications include transmission amplification within two plates separated by a small ligament. Finally we proposed a design procedure to suppress low-frequency flexural vibrations in an elongated plate implementing a by-pass system re-routing waves within the mechanical system.

Chapter 1

Introduction

In engineering applications the necessity to model unbounded domains is often required. This is particular important in modeling of soil-structure interaction [30, 63, 112], fluid-solid interaction [51, 100], ground-borne noise and vibration emitted by transportation systems [110, 114], geophysics [44, 99], non-destructive evaluation methods [57, 87], fluid-dynamics and traffic flow [68] and general problems of wave propagation (electromagnetic, elastic, acoustics, seismic). The list includes also hydro- and aerodynamic problems (external flows, duct flows, reacting flows, jets, boundary layers, free surfaces with aerospace, marine/naval, automotive, meteorological, industrial, and environmental applications), flows in porous media, filtration (with applications to oil recovery), magneto- hydrodynamic flows, plasma (e.g., solar wind) just to name a few.

In order to keep the computation feasible there is the necessity to truncate the models within a finite computational domain. This can be done by the boundary integral methods, infinite elements, non-reflecting boundary conditions and absorbing layers.

The boundary element method (see, for example, the monographs [2, 7, 13, 43, 120]) can be used directly for exterior problems over a finite region. It is an efficient numerical technique formulated for both static and dynamic problems, which is computationally cost effective in view of the fact that it reduces the dimensionality of the problem and only the boundary of the domain needs to be discretized. On the contrary, it is more difficult to implement with respect to Finite Element and Finite Difference algorithms and the coupling with different numerical schemes requires special attention. Also, some of the advantages of the method are lost and additional difficulties arise for non-linear problems in plasticity [9, 71, 92, 113] and finite elasticity [15, 16, 84, 89, 93].

Infinite element schemes [10, 11] represent the domain in its entirety by using elements of infinite extent where the shape functions include outwardly propagating wave-like factors. The formulation may rely on a truncated multipole expansion [21, 64], that incorporates frequency dependent interpolation functions along the radial (outward) direction [45, 53]. However, infinite elements have problems of accuracy and unwanted boundary reflections in the case of the propagation of guided or bulk waves [5, 35, 66]. Also, a region much larger than the region of interest must be implemented in order to achieve accuracy.

Absorbing boundary conditions (ABCs) and perfectly matched layers (PMLs) permit outward propagating waves and must suppress spurious reflections at least to an acceptable level. ABCs were first introduced in [69], where it is shown that, for second order wave equations and linearized shallow water equations, exact conditions are expressed in terms of integro-differential equations which are then approximated by a hierarchical system of differential equations [81].

Instead of ad-hoc boundary conditions PML is a region bordering the computational domain where waves are damped so that propagating waves become evanescent. The key property is always the absence of reflection at the interface between the physical and the absorbing domains. The problem of reflection at the interface between the physical domain and the absorbing one was solved in [8] for problems governed by Helmholtz equations. The PMLs have become the most popular absorbing conditions for finite-difference time-domain and finite element wave simulations and many examples demonstrate their superior performance as compared to 'sponge-layer' absorbing boundary condition [25, 108], paraxial conditions [50, 97], asymptotic local or non-local operators [46, 47].

PMLs correspond to a coordinate transformation in which the coordinate normal to the artificial boundary is mapped to complex values leading to decaying amplitude behavior [28]. Transformation optics has been introduced by [65, 88] for electromagnetic invisibility cloaks [62, 105]. The key property is the invariance of Maxwell's equations under coordinate transformations [94]. The same model has been successively applied to problems governed by equations isomorphic to Maxwell's equations: they include acoustics [27, 82, 102], thermodynamics [101, 104] and out-of-plane elastic waves [32, 86]. Applications and models can also be found in [40, 55]. Invisibility cloaks for flexural waves where first proposed by [37, 38] and a first experiment was given by [111]. The transformed model was successively refined in [20, 33, 54] where the transformed equation was interpreted within the 2^{nd}-order theory applied for the study of buckling elastic structures. Invariance under coordinate transformation is not satisfied in general. This is the case of elastodynamics equations and [83] demonstrated that the transformed equation requires either non-symmetric stress tensor [17] or tensorial density and dependance of the stress on velocity [75].

PMLs can be also interpreted as a viscous anisotropic material in the boundary region [98]. It is highly effective in absorbing waves over wide ranges of frequency and incidence angles, is numerically stable and needs relatively thin layers. PML was first developed for electromagnetic waves [8, 28], and then extended to the fields of acoustics [96], seismology [58, 59], dispersive waves [61] as well as to elastic waves [49, 80, 109, 123]. Surprisingly, applications to flexural waves, governed by fourth-order differential equations, are limited to a recent result, which is focused on the numerical implementation [41]. The purpose of the work is to fill this gap.

In [26] the construction of PML for elastic wave propagation was linked to conformal mapping techniques adopted for the design of invisibility cloaks [17, 75, 83], a technique implemented in the numerical simulation given in [17]. Here we implement a similar approach for the problem of flexural waves [20, 33, 54].

The presented model is studied in the time-harmonic regime. However, the simple computation given in Figure 1.1 shows that the proposed PML performs well also in the transient regime. In the Thesis we compare the case of longitudinal and transverse waves within an elongated beam in order to stress the additional issues associated to the flexural case. Also, we give particular importance to the physical interpretation of the PML.

In Section 2.1 of Chapter 2, we present the transformation optics technique for longitudinal waves in a thin rod, we detail the transformed equation, we discuss the interface boundary conditions and present a comparison with the analytical Green's function in a infinite rod. In Section 2.2, we present the model for flexural waves in beam structures. We detail the transformed equation and we discuss the

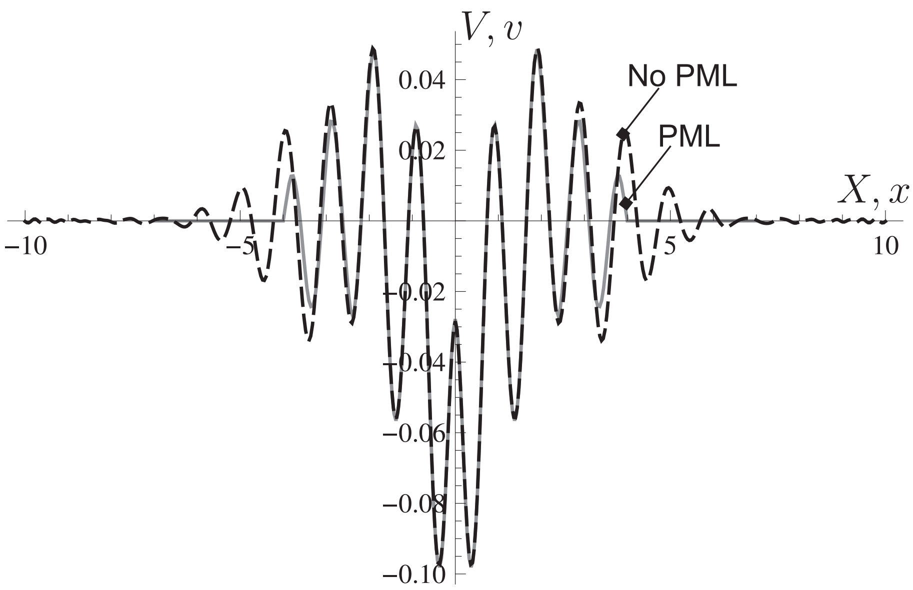

FIGURE 1.1: Transient finite element analysis. Transverse displacement at $t = 0.5\,\mathrm{s}$ in a beam subjected to a transient force $F(t)$ applied at $X = 0\,\mathrm{m}$. $F(t)$ is shown in Figure 2.8 in Chapter 2. Dashed black line shows the displacement in a large domain without PML, continuous gray line shows the displacement in a short domain with PML.

condition on the transformation in order to automatically satisfy interface conditions. We present different numerical examples concerning invariance of eigenfrequencies, transformation of eigenmodes and we discuss the effect of boundary conditions and describe the transient example of Figure 1.1.

The propagation of flexural waves in Kirchhoff-Love plates is described in Chapter 3. Adoption of PMLs for flexural waves in plates involves additional issues which are solved in the present work. The biharmonic equation of motion for Kirchhoff-Love plates under transformation does not retain its form [20, 33, 54]. The transformation affects also the interface conditions and additional constraints are set in order to avoid reflection.

In Chapter 3, we give the analytical form of PMLs for flexural waves in plates, we describe the implementation and we perform a deep quantitative analysis on the dependance of the perturbation on several parameters.

Also in this case the model is studied in the time-harmonic regime and the comparison given in Figure 1.2 between a numerical solution and analytical one, gives a qualitative indication of the accuracy of the proposed technique.

In Section 3.1, we briefly report the equation of motion and the boundary conditions for Kirchhoff-Love plates. The fields are given in tensorial form. In Section 3.2, we analyse perfect boundary conditions and we show the dependance on the direction of the wave. In Section 3.3, we detail the transformed equation of motion, we describe the physical interpretation and we analyse the transformed boundary conditions and the constraints to avoid reflection. Eigenfrequency analysis is given in Section 3.4 and several examples are reported highlighting that standard approaches lead to an erroneous evaluation of egienfrequencies. In Section 3.5 we introduce PMLs. After detailing the analytical form of the PMLs we describe in Section 3.6 the implementation and the comparison with the analytical time-harmonic Green's function in free space. Several analysis of optimality are performed to show the influence of the following aspects: discretization, frequency, type of boundary conditions, relative dimensions of the PMLs, amount of transformation, dissipation and relative position of the applied load.

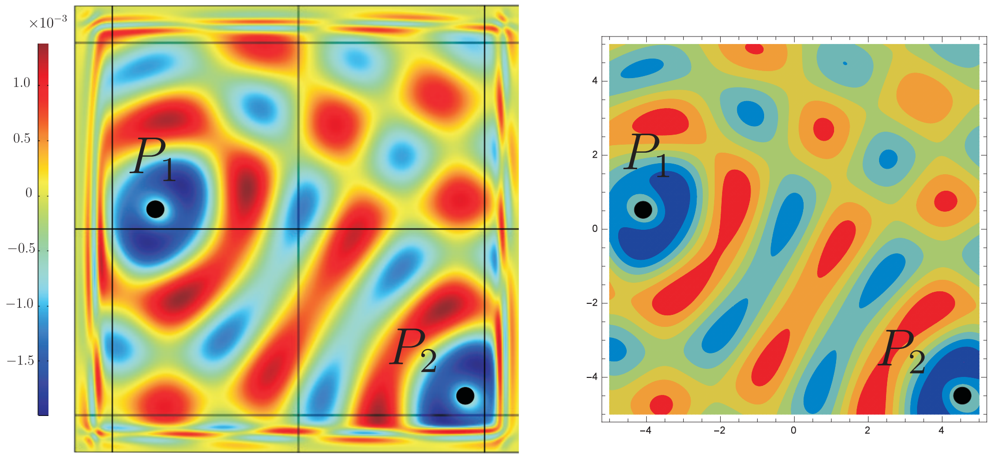

(*a*) (*b*)

FIGURE 1.2: Transverse displacement amplitude in a plate generated by the interaction of two point loads. (a) FEM analysis on a finite domain implemented in *Comsol Multiphysics*®. (b) Analytical free-space solution.

In Chapter 4 we propose a new type of metamaterial plate.

Metamaterials are microstructured media engineered to have properties that are not found in nature. The first models were developed in electromagnetism and optics and then extended to acoustic and elasticity [22, 23, 34, 36]. More recently, systems such as the Kirchhoff-Love plate equations for flexural waves, labelled as *platonics* by McPhedran et al. [72], have been addressed. This flexural systems may show many of the typical anisotropic effects from photonics such as ultrarefraction, negative refraction and Dirac-like cones [3, 39, 73, 106, 116]. Structured plates may also show the capability of cloaking applications [37, 38, 76, 111] as a result of inhomogeneous and anisotropic constitutive properties and axial prestress [20, 33, 54].

One of the main properties of the biharmonic equation of motion governing the propagation of flexural wave is the decomposition into the Helmholtz and modified Helmholtz equations, associated respectively to the presence of propagating and evanescent waves. Such waves can be coupled via the boundary or interface contact conditions. In most configurations the flexural waves are led by their Helmholtz component [72] and the homogenized equation can be of parabolic type at special frequencies [3, 73]. However, short range wave scattering and Bragg resonance can be strongly influenced by the evanescent waves.

Periodic structures play a major role in this field [14], since they create band gaps. These are frequency ranges where waves cannot propagate through the periodic system leading to possible application as acoustic and mechanical wave filters, vibration isolators, seismic shields. Partial band gap can lead to anisotropic wave response that can be used to obtain focusing and localization [12, 18, 91] as well as polarization properties [60, 70].

Two physical mechanisms can open band gaps: Bragg scattering and local resonance [52, 74]. Bragg scattering is associated to the generation of band gaps at wavelengths of the same order of the unit cell around frequencies governed by the Bragg condition $a = n(\lambda/2)$, $(n = 1, 2, 3, \cdots)$, where a is the lattice constant of the periodic system and λ the wavelength [79]. Local resonances are associated to internal resonances due to the microstructures, they can be obtained from array of resonators as suggested in the seminal work [67]. Local resonances open tiny band gaps that can be at low frequencies [48, 121, 122] and inertial amplification mechanism that can widen stop band intervals have been proposed in [1, 42].

In the Thesis we propose an alternative approach in which we combine Bragg scattering and internal resonance inserting snail resonators within a periodically perforated plate. Internal resonances can be at extremely low frequencies since the equivalent stiffness of the ligament connecting the inertial elements to the host plate is arbitrarily low. In addition, the systems present not a single but a set of different resonance frequencies within the acoustic branch. In Section 4.1, we introduce the platonic plate with snail resonators, we detail the geometry in Section 4.1.1 and we determine the dispersion properties in Section 4.2. In Section 4.3 we derive the analytical estimation of the lowest frequencies of the proposed model. Finally, in Section 4.4, we show some numerical results addressing the capability of the microstructured platonic crystal to direct the wave propagation through the media, leading to localization, wave trapping and by-pass systems.

Chapter 2

Perfectly Matched Layers for Flexural waves in Beam structures

Here, we give the analytical form of PMLs for flexural waves in Euler-Bernoulli beams, we describe the implementation and we perform a quantitative analysis on the perturbation introduced by PML for perfect and classical boundary conditions.

2.1 Longitudinal waves in a rod

We start presenting the transformation of coordinates technique for a problem governed by a second-order differential equation. We show that for a rod the transformed equation maintains its form and the interface conditions are automatically satisfied eliminating any problem of reflection at the interface.

2.1.1 Equation of motion

We consider a thin rod having Young's modulus E, mass-density ϱ and cross-sectional area A. The rod is shown in Figure 2.1.

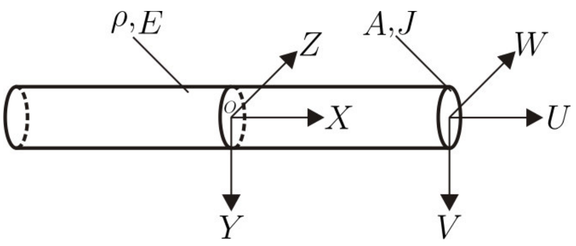

FIGURE 2.1: Beam structure. The displacement at point X and time t is $\mathbf{U} = (\mathrm{U}, \mathrm{V}, \mathrm{W})$

The longitudinal component U of the displacement vector $\mathbf{U} = (\mathrm{U}, \mathrm{V}, \mathrm{W})$, function of the position X and time t, satisfies the equation of motion [56]

$$[EA\,\mathrm{U}_X(X,t)]_X = \varrho A\,\mathrm{U}_{tt}(X,t), \tag{2.1}$$

where subscripts indicate derivative with respect to the indicated variable, i.e. $\mathrm{U}_X = \partial\mathrm{U}/\partial X$ and $\mathrm{U}_{tt} = \partial^2\mathrm{U}/\partial t^2$. The axial force is $N = EA\,\mathrm{U}_X$. For a homogeneous rod the longitudinal stiffness EA and the linear density ϱA are constant.

In the time-harmonic regime the displacement is $\mathbf{U}(\mathbf{X},\mathbf{t}) = U(\mathbf{X})\mathbf{e}^{-\mathbf{i}\omega\mathbf{t}}$, with ω the radian frequency, and the longitudinal component of the displacement satisfies the Helmholtz equation

$$[EA\,U_X(X)]_X + \varrho A\,\omega^2 U(X) = 0. \tag{2.2}$$

2.1.2 Transformed equation

We introduce a coordinate transformation $x = G(X)$, with $G(.)$ injective function, and we indicate with $g(x)$ the inverse function G^{-1}. First-order derivative in the original coordinate X and in the transformed one x are related by

$$\frac{d}{dX} = \frac{1}{g_x}\frac{d}{dx}. \tag{2.3}$$

Implementing the coordinate transformation in Eq. (2.2), we obtain the transformed equation of motion introducing a transformed displacement $u(x)$ such that $u(x) = U(X)$. The transformed equation of motion has the form

$$\left[\overline{EA}u_x(x)\right]_x + \overline{\varrho A}\omega^2 u(x) = 0, \tag{2.4}$$

which corresponds to an inhomogeneous rod having longitudinal stiffness $\overline{EA} = EA/g_x$ and linear density $\overline{\varrho A} = g_x \varrho A$. In general, the transformed longitudinal stiffness and linear density are inhomogeneous. However, for affine transformations where $g_x(x) = const$, they reduce to the homogeneous case.

2.1.3 Interface boundary conditions

Let us apply the coordinate transformation in a domain $X > X_0$, where X_0 is a given point. In such a case the problem is governed by the untransformed equation of motion (2.2) for $X < X_0$ and by the transformed equation of motion (2.4)for $X > X_0$.

The untransformed and transformed domains have to share the same interface point, which means that the transformation has to satisfy the relation $X_0 = g(x_0) = x_0$. In addition, at the interface point X_0 continuity conditions on the longitudinal displacement and on the axial force must be satisfied. We note that, if after transformation displacement $u(x)$ or axial force $n(x)$ change at the point X_0, a reflected wave will be generated. Clearly, zero reflection is required to have perfect match.

For the rod, in addition to the imposed equality $u(x) = U(X)$, we have

$$n(x) = \overline{EA}\frac{d}{dx}[u(x)] = \frac{EA}{g_x} g_x \frac{d}{dX}[u(x)] = EA\frac{d}{dX}[U(X)] = N(X). \tag{2.5}$$

Therefore, both displacement u and axial force n in the transformed point x are equal to displacement U and axial force N in the original point X. These two equalities clearly hold also at the point $X_0 = x_0$ assuring the absence of reflection at the interface.

2.1.4 Eigenfrequency Anlaysis

Here we compute eigenfrequencies and eigenmodes for longitudinal waves in a domain in which we introduce a transformation, and we compare the results with the eigenfrequencies and eigenmodes in a homogeneous system in the absence of the transformation.

We consider an homogeneous rod of length $2L$ fixed at its ends. The solution of the Helmholtz equation (2.1) is

$$U(X) = A_1 e^{i\alpha X} + A_2 e^{-i\alpha X}, \tag{2.6}$$

where $\alpha = \omega\sqrt{E/\varrho}$.

For fixed-fixed boundary conditions $U(\pm L) = 0$ the eigenfrequency need to satisfy the condition $\sin(2\alpha L) = 0$, leading to the well-known results $\omega = \sqrt{\varrho/E}(n\pi)/(2L)$, with n positive integer. The corresponding eigenmodes are $\sin[n\pi(X+L)/(2L)]$.

Now, we introduce a second structure having the same homogeneous properties for $-L \leq X \leq 0$, while the right half $0 \leq X \leq L$ is transformed into the domain $0 \leq x \leq l$ by generic transformation $G(X)$ with inverse $g(x)$. The transformation $g(x)$ has to satisfy the conditions $g(0) = 0$ and $g(l) = L$. The problem is solved by

$$\begin{cases} U(X) = B_1 e^{i\alpha X} + B_2 e^{-i\alpha X}, & \text{for } -L \leq X \leq 0, \\ u(x) = B_3 e^{i\alpha g(x)} + B_4 e^{-i\alpha g(x)}, & \text{for } 0 \leq x \leq l. \end{cases} \tag{2.7}$$

The solution is found by satysfying the boundary conditions

$$U(-L) = u(l) = 0 \tag{2.8}$$

and the interface conditions

$$U(0) = u(0), \qquad EA\,U'(0) = \overline{EA}(0)u'(0). \tag{2.9}$$

The system of boundary and interface conditions has the form

$$\begin{bmatrix} e^{-i\alpha L} & e^{i\alpha L} & 0 & 0 \\ 1 & 1 & -1 & -1 \\ i\alpha & -i\alpha & -i\alpha & i\alpha \\ 0 & 0 & e^{i\alpha g(l)} & e^{-i\alpha g(l)} \end{bmatrix} \begin{pmatrix} B_1 \\ B_2 \\ B_3 \\ B_4 \end{pmatrix} = \begin{pmatrix} 0 \\ 0 \\ 0 \\ 0 \end{pmatrix}. \tag{2.10}$$

The condition of determinant equal to zero for the matrix in Eq. (2.10) is

$$-4\alpha\sin(2\alpha L) = 0, \tag{2.11}$$

which gives exactly the same eigenfrequencies as in the homogeneous case.

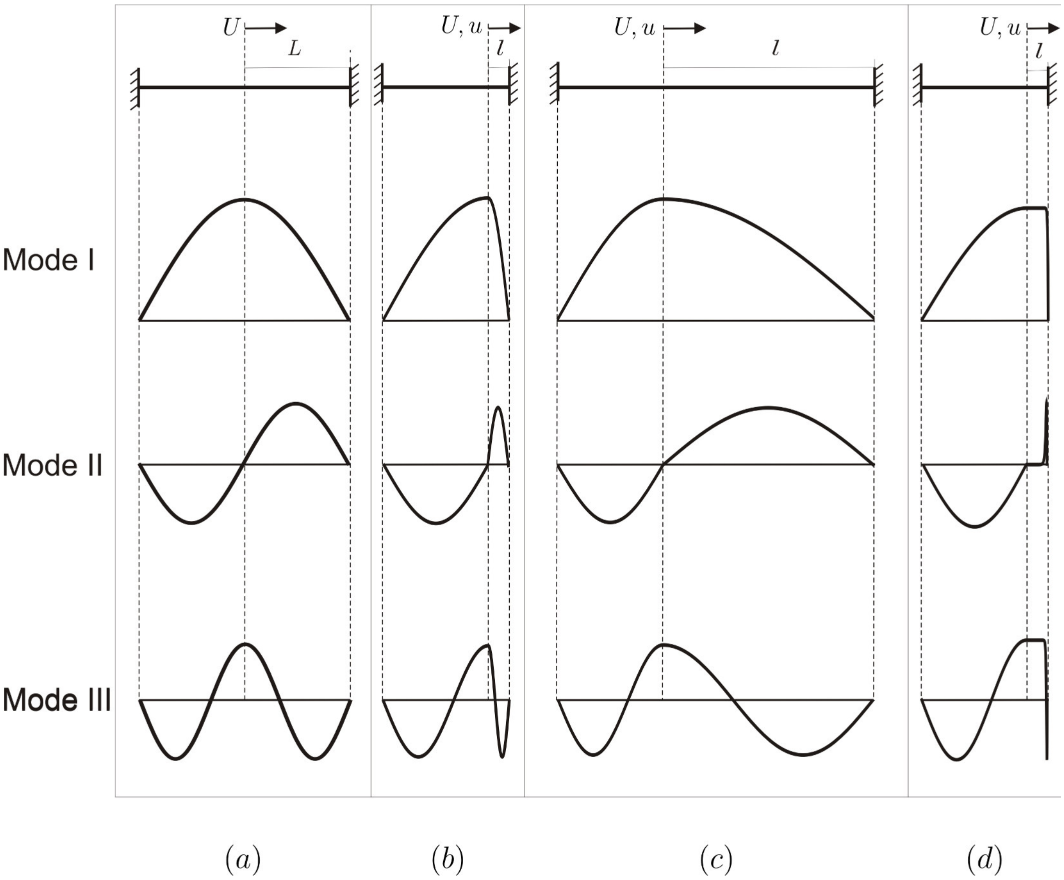

FIGURE 2.2: Eigenmodes for longitudinal waves in a rod. (a) Homogeneous rod of length $2L$. (b-d) The rods are subjected to a geometric transformation in the domain $0 \leq X \leq L$. (b) Rod subjected to the linear transformation (2.12) with $l/L = 0.2$. (c) Rod subjected to the linear transformation (2.12) with $l/L = 2$. (d) Rod subjected to the non linear transformation (2.13) with $l/L = 0.2$.

The eigenmodes for the homogeneous problem and the problem with transformation are given in Figure 2.2. We consider different transformation. We start with two linear transformations given by

$$g_a(x) = \frac{L}{l}x, \tag{2.12}$$

where we consider the two cases $l/L = 0.2$ and $l/L = 2$. Then, we show the results for the nonlinear transformation

$$g_b(x) = \frac{e^{-100x} - 1}{e^{-100l} - 1}L, \tag{2.13}$$

From the comparative analysis in Figure 2.2 it is shown that the eigenmodes are the same in the homogeneous domain while $u(x) = u[G(X)] = U(X)$ in the inhomogeneous ones. The eigenmodes in the transformed domains can be tuned by changing the transformation $g(x)$, which can be linear or not.

2.1.5 Transformation for Perfectly Matched Layers in a rod

In addition to the perfect match, the transformation must damp the incoming waves; this target can be achieved by applying a complex transformation with $g(x) = x + ih(x)$, where the real function $h(x) \geq 0$ and $h(x_0) = 0$. We note that, employing such a transformation, the generic wave $\exp[ikX]$ is transformed into the wave $\exp[k(-h(x) + ix)]$, which decays exponentially fast. Such a model, based on coordinate transformation, include previously proposed PMLs obtained introducing artificial dissipation in the form of complex linear stiffness and density, respectively. In [103] complex material parameters were used to build PMLs for electromagnetic problems, which are governed by Helmholtz equations, while the conformal mapping technique was applied in [26] in order to define PML for the plane elastodynamic problem governed by a system of second-order PDE. Here we consider the general transformation $g(x) = x + i\alpha(x - x_0)^n$, where α and n are two parameters that can be varied in order to tune the wave damping. For the purpose of illustration, we show a comparison between an analytical solution and a numerical implementation for the infinite body Green's function. For the rod problem the time-harmonic Green's function expressing the displacement in X due to a unit force applied in X_c vibrating harmonically with frequency ω is given by

$$U_g(X, X_c; \omega) = -\frac{1}{2k} \sin k|X - X_c|, \tag{2.14}$$

where $k = \omega\sqrt{\varrho/E}$ (see, for example, [56]).

In Figure 2.3a we compare the analytical solution for the infinite body Green's function with a numerical solution with $\alpha = 1$ and $n = 1$, implemented in *Comsol Multiphysics*® on a finite domain of total length of 20m and centered at $X = 0$. Two PML domains have been implemented in the boundary regions $8\text{m} \leq |X| \leq 10\text{m}$ so that $X_0 = \pm 8\text{m}$, the radian frequency is $\omega = \pi/2$. We stress the excellent agreement between the analytical and numerical solutions and the wave damping within the PML regions. The agreement between the analytical and numerical solutions demonstrates the matching at the interface points $X_0 = \pm 8$

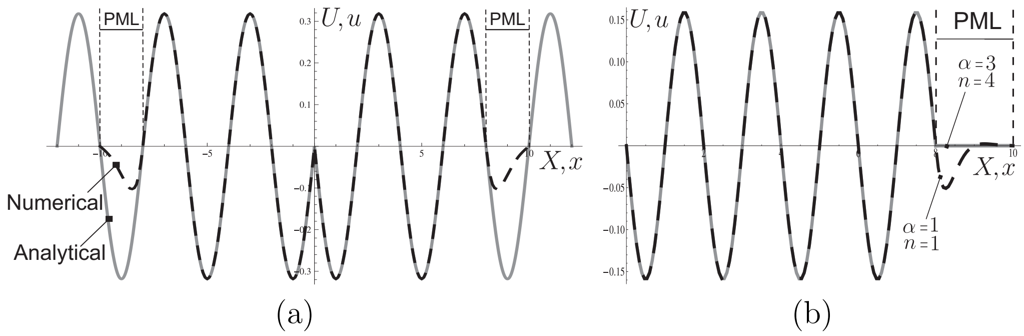

FIGURE 2.3: Time-harmonic infinite body Green's function in rod structures. Results are given for $k = 1\,\mathrm{m}^{-1}$. (a) Comparison between analytical solution (2.14) for an infinite rod and numerical solution implemented in *Comsol Multiphysics®* for a finite system, with $|X| \leq 10$m and radian frequency $\omega = \pi/2$. The PMLs have been implemented employing a transformation with $\alpha = 1$ and $n = 1$. (b) Comparison between numerical solutions with transformation parameters $\alpha = 1$, $n = 1$ and $\alpha = 3$, $n = 4$. Results are given for $\omega = \pi$ and are shown only in the region $0 \leq X \leq 10$m.

and the absence of reflection. In part (b) we compare two numerical solutions obtained applying an affine transformation with $\alpha = 1$, $n = 1$ and a non-affine transformation with $\alpha = 3$, $n = 4$. The results, given for $\omega = \pi$ and reported only in the region $X \geq 0$, show again excellent agreement in the central region and the increased damping for the second choice of material parameters.

In conclusion of this Section we note that the transformation is frequency independent and, therefore, the PMLs work equally well at different frequencies subjected to the usual limitations on the mesh size with respect to the wavelength.

2.2 Flexural waves in a beam

In this Section we apply the transformation coordinates technique for flexural waves in a slender Euler-Bernoulli beam, governed by a fourth-order differential equation. We give a physical interpretation of the transformed equations as in [20, 33]. We also show that, under coordinate transformation, the transformed medium possesses the same eigenfrequencies as the original one, a property that can be used in order to check to correctness of the transformation in finite domains with evident advantages on the implementation.

2.2.1 Equation of motion

We consider time-harmonic transverse displacements $\mathrm{V}(X,t) = V(X)e^{-i\omega t}$ in a slender Euler-Bernoulli beam structure as in Figure 2.1. The beam has cross-sectional area A, second-moment of inertia J and density ϱ. The equation of motion for $V(x)$ is

$$[EJ\,V_{XX}(X)]_{XX} - \varrho A\,\omega^2 V(X) = -T_X(X) - \varrho A\,\omega^2 V(X) = 0. \tag{2.15}$$

where $T(X) = M_X(X) = -[EJ\,V_{XX}(X)]_X$ is the shear force and $M(X)$ the bending moment. The transverse displacement component $W(X)$ is governed by an analogous fourth-order differential equation.

2.2.2 Transformed equation

Again, we introduce the transformation $x = G(X)$, with inverse transformation $X = g(x)$.

Setting this transformation on the equation of motion (2.15) leads to

$$EJ[\frac{[v_{xx}(x)]_{xx}}{g_x^3} - 6\frac{g_{xx}}{g_x^4}[v_{xx}(x)]_x + \frac{15g_{xx}^2 - 4g_{xx}g_x}{g_x^5}[v_{xx}(x)]$$
$$+\frac{10g_{xxx}g_{xx}g_{xx}^5 - g_{xxxx}g_x^6 - 15g_x^4g_{xx}^3}{g_x^{10}}[v_x(x)]] + \overline{\varrho A}(x)\,\omega^2 v(x) = 0, \tag{2.16}$$

Then, the transformed equation of motion can be recollected in

$$[t(x) + n(x)v_x(x)]_x + \overline{\varrho A}(x)\,\omega^2 v(x) = 0, \tag{2.17}$$

where $v(x)$ is the transformed transverse displacement, that we assume equal to $V(X)$. The transformed shear and axial forces are given by

$$t(x) = m_x(x) = -\left[\overline{EJ}(x)v_{xx}(x)\right]_x, \quad n(x) = \frac{3g_{xx}^2(x) - g_{xxx}(x)g_x(x)}{g_x^5(x)}EJ, \tag{2.18}$$

respectively, where $m(x)$ is the transformed bending moment. The bending stiffness and linear density transform as follows

$$\overline{EJ}(x) = \frac{EJ}{g_x^3}, \qquad \overline{\varrho A}(x) = g_x \varrho A. \tag{2.19}$$

We note that the equation of motion (2.17) represents an inhomogeneous beam in presence of axial stress (see [20, 33]). As for the Helmhotz equation transformation changes homogeneous, isotropic material in an inhomogeneous, anisotropic one. The flexural case has the additional feature that transformed equation of motion does not retain its form. We interpret the additional terms as axial forces $n(x)$.

2.2.3 Interface conditions

Again interface conditions must satify the continuity of fields between transformed and untransformed domains. A change in the boundary interface values of the fields leads to a perturbation of the original field and to consequent wave reflection. At the interface $X_0 = x_0$ between untransformed and transformed domains the following essential conditions

$$\begin{cases} V(X_0) = v(x_0), \\ V_X(X_0) = v_x(x_0), \end{cases} \tag{2.20}$$

and natural conditions

$$\begin{cases} M(X_0) = m(x_0), \\ T(X_0) = t(x_0) + n(x_0)v_x(x_0), \end{cases} \tag{2.21}$$

must be satisfied.

Expressing the interface conditions in the transformed domain as a function of the original variable X, of the original displacement V(X) and of the inverse transformation function $g(x)$, we obtain after simple algebraic manipulations

$$\begin{cases} v(x_0) = V(X_0), \\ v_x(x_0) = g_x(x_0)V_X(X_0), \\ m(x_0) = -EJ\dfrac{g_x^2(x_0)V_{XX}(X_0) + g_{xx}(x_0)V_X(X_0)}{g_x^3(x_0)}, \\ r(x_0) = t(x_0) + n(x_0)v_x(x_0) = EJ\dfrac{3g_{xx}^2(x_0) - g_{xxx}(x_0)g_x(x_0)}{g_x^4(x_0)}V(X_0) \\ \qquad -EJ\dfrac{g_x^3(x_0)V_{XXX}(X_0) + 3g_x(x_0)g_{xx}(x_0)V_{XX}(X_0) + g_{xxx}(x_0)V_X(X_0)}{g_x^3(x_0)}. \end{cases} \tag{2.22}$$

Then, the constraints

$$g_x(x_0) = 1, \quad g_{xx}(x_0) = 0, \quad g_{xxx}(x_0) = 0, \tag{2.23}$$

in Eqs. (2.22) assure that interface conditions (2.20) and (2.21) are satisfied independently on the general choice of the transformation $G(X)$ or of its inverse $g(x)$. The three conditions in Eq. (2.23) must be complemented by the additional condition $X_0 = g(x_0) = x_0$, which identifies the same interface point between untransformed and transformed domains.

We note that transformed bending stiffness and linear density, defined in Eq. (2.19), are homogeneous only for affine transformation. Hovewer, the only admissible affine transformation for the beam case is the identity in view of the constraints $g(x_0) = X_0$ and $g_x(x_0) = 1$, which means that an inhomogeneous material is needed in the transformed domain.

2.2.4 Eigenfrequency Anlaysis

Here we compare eigenfrequencies and eigenmodes for a homogeneous beam defined in the domain $-L \le X \le L$ and for a second beam structure where we apply a transformation on the right half of the structure $0 \le X \le L$ which transforms into the domain $0 \le x \le l$, as shown in Figure 2.4a. We consider a polynomial transformation $g(x)$ subjected to the constraints as in Eq. (2.23) and $x_0 = g(x_0) = X_0$ at the interface point $x_0 = X_0 = 0$. In addition, we impose

$g(l) = L$, which defines the length of the transformed domain and the additional conditions

$$g_x(l) = 1, \quad g_{xx}(l) = 0, \quad g_{xxx}(l) = 0, \tag{2.24}$$

assuring the direct identification of the same boundary conditions on rotation, moment and vertical force at the boundary point $x = l$, as demonstrated in the previous Section. The corresponding transformation is the monotonically increasing polynomial

$$g(x) = x + 35\frac{L-l}{l^4}x^4 - 84\frac{L-l}{l^5}x^5 + 70\frac{L-l}{l^6}x^6 - 20\frac{L-l}{l^7}x^7. \tag{2.25}$$

Coordinate transformation (2.25) does not depend on the boundary conditions. For specific boundary conditions it is not necessary to impose all conditions (2.24); for example, in the case of a simple support, where $V(L) = 0$, $V_{XX}(L) = 0$, $V_X(L) \neq 0$ and $V_{XXX}(L) \neq 0$, only the conditions $g_x(l) = 1$, $g_{xx}(l) = 0$ are needed to assure that the bending moment $m(l)$ is zero in addition to the displacement $v(l)$ (see Eq. (2.22)). Nevertheless, we have proposed transformation (2.24) which includes all possible boundary conditions.

We also note that, apart from satisfaction of conditions at interface and boundary points, there is complete freedom in the choice of the transformation $g(x)$ within a properly defined set of functions.

Restricting the attention to a simply supported beam, the homogeneous problem governed by the Eq. (2.15) has solution

$$V(X) = A_1 e^{i\beta X} + A_2 e^{-\beta X} + A_3 e^{-i\beta X} + A_4 e^{\beta X}, \tag{2.26}$$

where $\beta^4 = (\varrho A)/(EJ)\omega^2$; such a solution, supplemented by the boundary conditions $V(-L) = V(L) = 0$, $V_{XX}(-L) = V_{XX}(L) = 0$, gives the well known result that eigenfrequencies are $\omega = (n\pi)^2/(4L^2)\sqrt{(EJ)/(\varrho A)}$ (n positive integer number) and the corresponding eigenmodes are $V(X) = \sin[n\pi(X + L)/(2L)]$.

For the problem in which the region $0 \le X \le L$ has been transformed into the region $0 \le x \le l$ by mean of the transformation (2.25), the solution (2.26) is still valid within the domain $-L \le X \le 0$, while in the domain $0 \le x \le l$ the problem is governed by the transformed equation of motion, given in Eq. (2.17). In such a

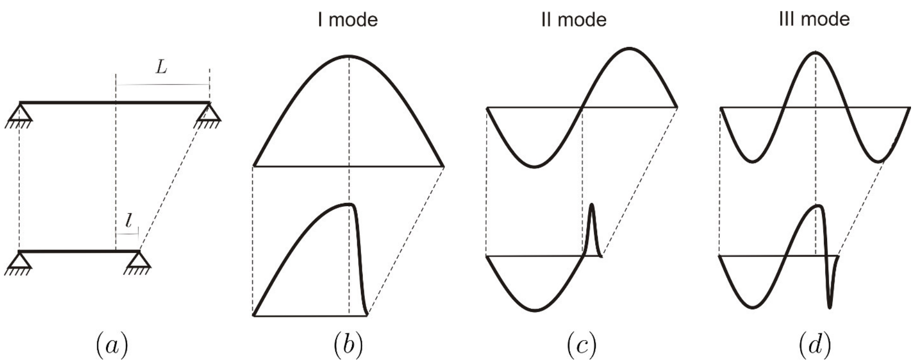

FIGURE 2.4: Eigenmodes of homogeneous beam of length $2L$ and inhomogeneous beam of length $L + l$. (a) Simply supported beams: the inhomogeneous beam has been obtained from transformation (2.25), the half-length $L = 1$ m is transformed into the length $l = 0.2$ m. (b) First eigenmodes for the two structures at $\omega = \pi^2/(4L^2)\sqrt{(EJ)/(\varrho A)}$. (c) Second eigenmodes at $\omega = 4\pi^2/(4L^2)\sqrt{(EJ)/(\varrho A)}$. (d) Third eigenmodes at $\omega = 9\pi^2/(4L^2)\sqrt{(EJ)/(\varrho A)}$.

domain the inhomogeneous bending stiffness and mass density are

$$\overline{EJ} = \frac{EJ}{\left(1 + 140\frac{L-l}{l^4}x^3 - 420\frac{L-l}{l^5}x^4 + 420\frac{L-l}{l^6}x^5 - 140\frac{L-l}{l^7}x^6\right)^3},$$
$$\overline{\varrho A} = \left(1+140\frac{L-l}{l^4}x^3-420\frac{L-l}{l^5}x^4+420\frac{L-l}{l^6}x^5-140\frac{L-l}{l^7}x^6\right)\varrho A, \quad (2.27)$$

respectively.

The equation of motion for the transformed domain has the general solution

$$v(x) = B_1e^{i\beta g(x)} + B_2e^{-\beta g(x)} + B_3e^{-i\beta g(x)} + B_4e^{\beta g(x)}, \quad (2.28)$$

The system of two equations of motion is supplemented by the four boundary conditions $V(-L) = v(l) = 0$, $V_{XX}(-L) = v_{xx}(l) = 0$ and by the four interface conditions given in Eqs. (2.20) and (2.21), where $X_0 = x_0 = 0$.

Eigenfrequencies and eigenmodes are obtained from the eigenvalues and eigenvectors of the system of equations $\mathbf{Ma} = \mathbf{0}$ given by the 8 boundary and interface conditions, where $\mathbf{a} = [A_1\ A_2\ A_3\ A_4\ B_1\ B_2\ B_3\ B_4]^T$ is the vector of the unknown amplitudes and the matrix $\mathbf{M}$ collects the coefficients of the equations. Then, the condition

$$\det \mathbf{M} = 256(EJ)^2\beta^{10}\sin(2\beta L)\sinh(2\beta L) = 0, \quad (2.29)$$

gives exactly the same eigenfrequencies of the homogeneous system, namely $\omega = (n\pi)^2/(4L^2)\sqrt{(EJ)/(\varrho A)}$ (n positive integer) and the trivial one $\omega = 0$. The first 3

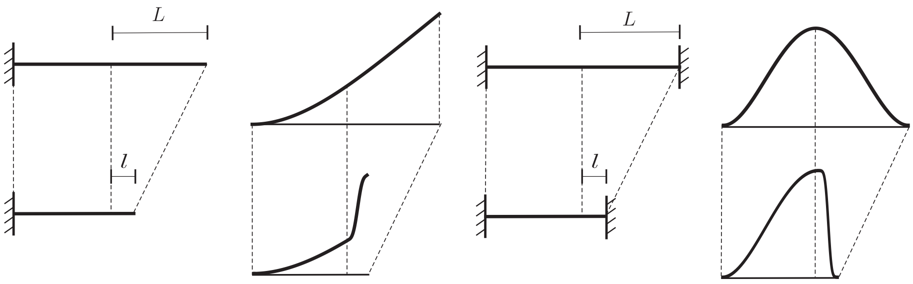

(*a*) (*b*)

FIGURE 2.5: Eigenmodes of homogeneous beam of length $2L$ and inhomogeneous beam of length $L+l$, $L=1$ m and $l=0.2$ m. (a) Clamped-free boundary conditions: the first eigenmode is shown, the eigenfrequency is $\omega=(0.597\pi)^2/(4L^2)\sqrt{(EJ)/(\varrho A)}$. (b) Clamped-clamped boundary conditions: the first eigenmode is shown, the eigenfrequency is $\omega=(1.505\pi)^2/(4L^2)\sqrt{(EJ)/(\varrho A)}$.

eigenmodes for the homogeneous and inhomogeneous systems are given in Figure 2.4 b-d. In particular, we note that the solution in the transformed domain is $v(x)=V[g(x)]=V(X)$.

In Figure 2.5 we report the first eigenmode for the two structures for different boundary conditions and the same transformation given in Eq. (2.25): clamped-free in part (a) and clamped-clamped in part (b). Again, the eigenfrequencies for the homogeneous and inhomogeneous systems coincide and the eigenmodes in the transformed domain are such that $v(x)=V(X)$.

We note that, while the coincidence of eigenfrequencies can be expected, it depends on the boundary conditions which, in the case of flexural waves, are not preserved by a general transformation, as shown previously. We also stress that, to the best of our knowledge, such a comparison has never been considered before to check the connection between the solutions before and after transformation.

2.2.5 Perfectly Matched Layers in a beam

A main feature of Perfectly Matched Layer is the damping of propagating wave avoiding any reflection. In order to introduce dissipation we consider a complex transformation such that $g(x)=g^R(x)+ig^I(x)$, where $g^R(x)$ and $g^I(x)$ stand for the real and imaginary parts. The constraints of Eq. (2.23) at the interface point

$X_0 = x_0$ plus the condition $g(x_0) = x_0$ imply that

$$\begin{cases} g^R(x_0) = x_0, \quad g^I(x_0) = 0, \\ g_x^R(x_0) = 1, \quad g_x^I(x_0) = 0, \\ g_{xx}^R(x_0) = g_{xx}^I(x_0) = 0, \\ g_{xxx}^R(x_0) = g_{xxx}^I(x_0) = 0. \end{cases} \tag{2.30}$$

Therefore, if we consider a polynomial transformation, the real and imaginary parts $g^R(x)$ and $g^I(x)$, respectively, must be at least polynomials of degree 4 in $(x - x_0)$ and, for the imaginary part, the lowest non-zero term has at least power 4.

2.2.6 Additional boundary condition

In the implementation of the Perfectly Matched Layer within a Finite Element code the infinite domain is substituted by a finite domain, which introduces an additional boundary condition at the boundary $x = x_1$ of the Perfectly Matched Layer domain. In general, this boundary condition perturbs the infinite domain solution.

By looking at the solution (2.28) of the transformed problem, we note that the propagating solution $B_1 e^{i\beta g(x)} + B_2 e^{-\beta g(x)}$ is generated at the interface at $x = x_0$, while the reflected solution $B_3 e^{-i\beta g(x)} + B_4 e^{\beta g(x)}$ is generated at the fictitious boundary $x = x_1$. Therefore, a possible approach in order to eliminate the perturbation introduced by the additional boundary conditions, is to define ad-hoc boundary conditions at $x = x_1$ that would eliminate the reflected solution, namely boundary conditions leading to $B_3 = B_4 = 0$. The fields at $x = x_1$ can be written in the partitioned form

$$\left[\begin{array}{c|c} \mathbf{A}_{11} & \mathbf{A}_{12} \\ \hline \mathbf{A}_{21} & \mathbf{A}_{22} \end{array}\right] \left(\begin{array}{c} \mathbf{b}_1 \\ \hline \mathbf{b}_2 \end{array}\right) = \left(\begin{array}{c} \mathbf{c}_1 \\ \hline \mathbf{c}_2 \end{array}\right) \tag{2.31}$$

where

$$\mathbf{b}_1 = \begin{pmatrix} B_1 \\ B_2 \end{pmatrix}, \quad \mathbf{b}_2 = \begin{pmatrix} B_3 \\ B_4 \end{pmatrix},$$
$$\mathbf{c}_1 = \begin{pmatrix} v(x_1) \\ v_x(x_1) \end{pmatrix}, \quad \mathbf{c}_2 = \begin{pmatrix} m(x_1) \\ r(x_1) \end{pmatrix}, \tag{2.32}$$

and

$$\mathbf{A}_{11} = \begin{bmatrix} e^{i\beta g(x_1)} & e^{-\beta g(x_1)} \\ i\beta g_x(x_1)e^{i\beta g(x_1)} & -\beta g_x(x_1)e^{-\beta g(x_1)} \end{bmatrix},$$

$$\mathbf{A}_{12} = \begin{bmatrix} e^{-i\beta g(x_1)} & e^{\beta g(x_1)} \\ -i\beta g_x(x_1)e^{-i\beta g(x_1)} & \beta g_x(x_1)e^{\beta g(x_1)} \end{bmatrix},$$

$$\mathbf{A}_{21} = EJ\,\beta \begin{bmatrix} \dfrac{e^{i\beta g(x_1)}[\beta g_x^2(x_1) - i g_{xx}(x_1)]}{g_x^3(x_1)} & -\dfrac{e^{-\beta g(x_1)}[\beta g_x^2(x_1) - g_{xx}(x_1)]}{g_x^3(x_1)} \\ \dfrac{i\, e^{i\beta g(x_1)}\eta_1(x)}{g_x^4(x_1)} & \dfrac{e^{-\beta g(x_1)}\eta_2(x)}{g_x^4(x_1)} \end{bmatrix},$$

$$\mathbf{A}_{22} = EJ\,\beta \begin{bmatrix} \dfrac{e^{-i\beta g(x_1)}[\beta g_x^2(x_1) + i g_{xx}(x_1)]}{g_x^3(x_1)} & -\dfrac{e^{\beta g(x_1)}[\beta g_x^2(x_1) + g_{xx}(x_1)]}{g_x^3(x_1)} \\ -\dfrac{i\, e^{-i\beta g(x_1)}\eta_1(x)}{g_x^4(x_1)} & -\dfrac{e^{\beta g(x_1)}\eta_2(x)}{g_x^4(x_1)} \end{bmatrix}, \tag{2.33}$$

with

$$\eta_1(x) = \beta^2 g_x^4(x_1) + 6g_{xx}(x_1)^2 - 2g_x(x_1)g_{xxx}(x_1)],$$
$$\eta_2(x) = \beta^2 g_x^4(x_1) - 6g_{xx}(x_1)^2 + 2g_x(x_1)g_{xxx}(x_1)]. \tag{2.34}$$

If we substitute the solution $\mathbf{b}_1 = \mathbf{A}_{11}^{-1}[\mathbf{c}_1 - \mathbf{A}_{12}\mathbf{b}_2]$ of the first pair of equations in (2.32), into the second pair of equations, we obtain

$$(\mathbf{A}_{22} - \mathbf{A}_{21}\mathbf{A}_{11}^{-1}\mathbf{A}_{12})\mathbf{b}_2 = \mathbf{c}_2 - \mathbf{A}_{21}\mathbf{A}_{11}^{-1}\mathbf{c}_1. \tag{2.35}$$

The solution of the system of two equations (2.35) is zero, i.e. $B_3 = B_4 = 0$, if

$$\mathbf{c}_2 = \mathbf{A}_{21}\mathbf{A}_{11}^{-1}\mathbf{c}_1, \tag{2.36}$$

provided that

$$\det[\mathbf{A}_{22} - \mathbf{A}_{21}\mathbf{A}_{11}^{-1}\mathbf{A}_{12}] \neq 0 \text{ and } \det[\mathbf{A}_{11}] \neq 0. \tag{2.37}$$

The two conditions in (2.36) express the natural boundary conditions $m(x_1)$ and $r(x_1)$ as a function of the essential boundary conditions $v(x_1)$ and $v_x(x_1)$. The explicit expressions are

$$\begin{aligned} m(x_1) &= EJ\frac{-i\beta^2 g_x^3(x_1)v(x_1) + [-g_{xx}(x_1) + (1-i)\beta g_x^2(x_1)]v_x(x_1)}{g_x^4(x_1)}, \\ r(x_1) &= EJ\frac{(1+i)\beta^3 g_x^5(x_1)v(x_1) + [\eta_1(x_1) + (i-1)\beta^2 g_x^4(x_1)]v_x(x_1)}{g_x^5(x_1)}, \end{aligned} \quad (2.38)$$

where η_1 is given in Eq. (2.34). We note that the two determinants in Eq. (2.37) can be always set different from zero for every β by modulating the quantity $g(x_1)$.

The Perfectly Matched Layer and the optimal boundary conditions given in Eq. (2.38) have been implemented in the Finite Element code *Comsol Multiphysics*®. In particular, we consider the infinite body time-harmonic Green's function, which has the analytical expression

$$V_g(X, X_c; \omega) = \frac{1}{4EJ\beta^3}[e^{-\beta|X-X_c|} + \sin(\beta|X - X_c|)], \quad (2.39)$$

as in [19]. The analytical expression is compared with numerical simulations. We considered the following structural parameters: $EJ = 1\,\mathrm{MPa}$, $\rho A = 1\,\mathrm{kg/m}$, $X_C = 0\,\mathrm{m}$, $X_0 = x_0 = \pm 8\,\mathrm{m}$ and $x_1 = \pm 10\,\mathrm{m}$. The implemented inverse transformation is

$$\begin{aligned} g(x) = x &\mp \frac{35(x_1 - 2x_0)}{(x_1 - x_0)^4}(x \mp x_0)^4 + \frac{84(x_1 - 2x_0)}{(x_1 - x_0)^5}(x \mp x_0)^5 \mp \\ &\frac{70(x_1 - 2x_0)}{(x_1 - x_0)^6}(x \mp x_0)^6 + \frac{20(x_1 - 2x_0)}{(x_1 - x_0)^7}(x \mp x_0)^7 + i(x \mp x_0)^n, \end{aligned} \quad (2.40)$$

where $\mp$ stands for the PML domains at $x \in (\pm x_0, \pm x_1)$ and $\alpha = 5$. Transformation (2.40) has been obtained applying conditions (2.30), where x_0 stands for $\pm x_0$ and conditions

$$g^R(\pm x_1) = \pm 2x_0, \; g_x^R(\pm x_1) = 1, \; g_{xx}^R(\pm x_1) = 0, \; g_{xxx}^R(\pm x_1) = 0 \quad (2.41)$$

on the real part of the transformation. Additional conditions on the imaginary part of the transformation g^I at $x = \pm x_1$ have not been applied since they lead to larger amplitude reflected fields.

The deformed shapes are given in gray lines in Figure 2.6a for different discretizations, while the dashed black line indicates the analytical solution as in Eq. (2.39).

The comparative analysis shows that the results converge towards the analytical solution in the central region increasing the number of elements. In the PML regions it is evident the damping of the wave.

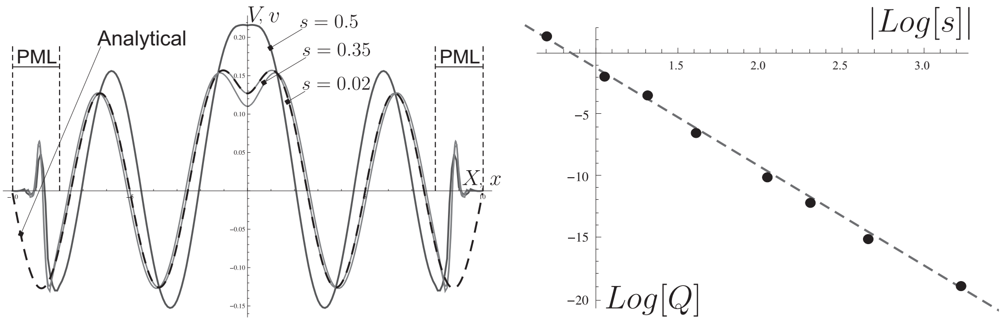

(a) (b)

FIGURE 2.6: (a) Time-harmonic Green's function. The analytical displacement of Eq. (2.39) is given in black dashed line. The numerical results are given in continuous gray lines. Different curves correspond to different size s of the elements given in meter; the elements have constant length within the domain $(-x_1, x_1) = (-10\text{m}, 10\text{m})$ (b) *Quality factor* $\mathcal{Q}$ as a function of the size s of the element. Results are given in logarithmic scale.

We define the *quality factor*, the measure

$$\mathcal{Q} = \int_{-X_0}^{+X_0} \left(\frac{V(X) - V_g(X, 0; \omega)}{V_g(0, 0; \omega)} \right)^2 dX, \tag{2.42}$$

where $V(X)$ is the solution in the untransformed domain $X \in (-X_0, X_0)$. $\mathcal{Q}$ is a quantitative description of the quality of the PML, which tends to 0 for perfect PML, indicating the absence of perturbation within the central domain $X \in (-X_0, X_0)$. In Figure 2.6b the *quality factor* $\mathcal{Q}$ is shown as a function of the size s of the elements in double logarithmic scale. For simplicity, in each computation we considered elements of the same size s. The results show an excellent convergence of the numerical results toward the analytical solution. The linear regression, indicated with a dashed line in Figure 2.6b, indicates that the quality factor $\mathcal{Q}$ goes to zero as $6.78\, s^{8.14}$.

2.2.7 Perfectly Matched Layers with standard boundary conditions

In Section 2.2.6 we detailed how to implement perfect PML proposing an optimal solution for the additional boundary conditions introduced in the finite domain implemented numerically. Such a model gives excellent results, but has two limitations: first, it is difficult to implemen in a standard Finite Element code and second, boundary conditions are frequency dependent. Specifically, relations (2.38) between different boundary conditions depend on the parameter $\beta \propto \sqrt{\omega}$ and the frequency dependence limits the applicability of the proposed model to transient problems.

Here, we propose a simpler solution with frequency independent boundary conditions. In particular, we implement classical boundary conditions at $x = \pm x_1$, namely clamped, free and simply supported.

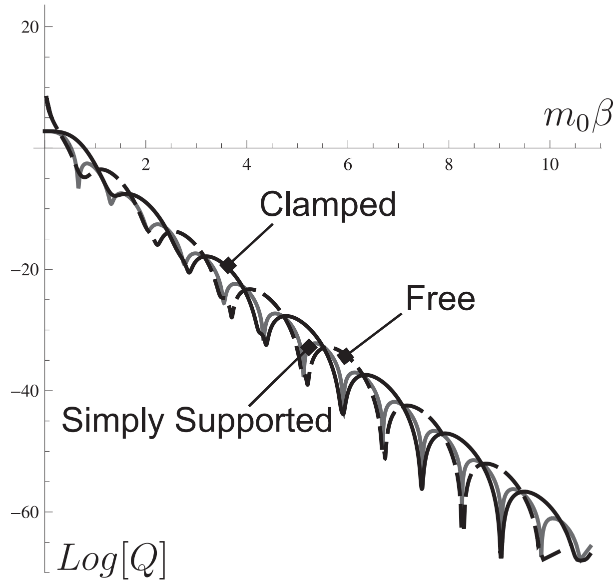

FIGURE 2.7: *Quality factor* $\mathcal{Q}$ as a function of the normalized frequency $m_0\beta$. Results are given for the same mechanical parameters of Figure 2.6. Continuous black line corresponds to simply supported boundary conditions, continuous gray line to free boundaries and dashed black line to clamped boundaries.

When these classical boundary conditions are implemented in *Comsol Multiphysics®* the obtained displacement fields, not reported here for brevity, show again an excellent agreement with the analytical results in the central region. In Figure 2.7 we report the *quality factor* $\mathcal{Q}$ as a function of the normalized frequency $m_0\beta = (x_1 - x_0)\beta$ for $n = 4$ in Eq. (2.40). The *quality factor* $\mathcal{Q}$ has been computed from the analytical solutions for the infinite medium and the finite medium with PML in order to check the effect of the boundary conditions independently on the influence of the discretization. The convergence increases with frequency and the three boundary conditions give equivalent results with a preference on the simply supported case at the lowest frequencies. Increasing the exponent n in the imaginary part of $g(x)$ in Eq. (2.40) gives equivalent results with the difference that the frequency oscillations for the *quality factor* $\mathcal{Q}$ curves as a function of β increases with n.

2.2.8 Dimension of the Layer

In order to estimate the error introduced by the layer of dimension $m_0 = |x_1 - x_0|$, we consider an incident plane wave $w_I(X) = e^{i\beta X}$ impinging the interface between the homogeneous domain and the PML at $X_0 = x_0 = 0$ and generating the reflected wave $w_R(X) = R_1 e^{-i\beta X} + R_2 e^{\beta X}$ and the transmitted wave $w_T(x) = T_1 e^{i\beta g(x)} + T_2 e^{-\beta g(x)} + T_3 e^{-i\beta g(x)} + T_4 e^{\beta g(x)}$, where the six constants R_1, R_2, T_1, T_2, T_3, T_4 can be easily found by imposing the four interface conditions at $x = x_0 = 0$ and two boundary conditions at $x = x_1 = x_0 + m_0$. The solution, for different boundary conditions has the form $T_1 = 1$, $T_2 = 0$, indicating the perfect match at the interface, and $R_1 = T_3$, $R_2 = T_4$, showing that the reflected wave is generated by the boundary conditions at $x = x_1$. In particular, for perfect boundary conditions as in Eq. (2.38) there is no reflection, i.e. $R_1 = T_3 = R_2 = T_4 = 0$, and, in principle, the only boundary conditions (2.38) are sufficient to avoid reflection without the need to introduce a PML. For clamped, simply supported and free boundary conditions the reflected amplitudes

$$|R_1| = f_1(m_0, \beta) e^{-2m_0^4 \beta}, \qquad |R_2| = f_2(m_0, \beta) e^{-m_0^4 \beta}, \tag{2.43}$$

where $f_1(m_0, \beta)$ and $f_2(m_0, \beta)$ are $\mathcal{O}(1)$ in m_0 and β and α is the exponent of the imaginary part of the transformation (2.40). For all boundary conditions, including the perfect ones, the displacement amplitudes decays exponentially as $e^{-m_0^\alpha}$, while [81] indicates that for problems governed by Helmhotz equations the reflection coefficients decay exponentially as e^{-2m_0}.

2.2.9 Transient Load Results

The PMLs with simply supported boundary conditions has been tested for the transient load as given in Figure 2.8. For the transient regime the following equations of motion have been solved numerically:

$$[EJ\, V_{XX}(X,t)]_{XX} + \varrho A\, V_{tt}(X,t) = 0, \tag{2.44}$$

in the untransformed domain D_1 and

$$\left[(\overline{EJ}(x)v_{xx}(x,t))_x - n(x)v_x(x,t)\right]_x + \overline{\varrho A}(x)\, v_{tt}(x,t) = 0, \tag{2.45}$$

in the transformed one D_2, where $\overline{EJ}$ and $\overline{\varrho A}$ are given in Eq (2.19) and $n(x)$ is given in Eq. (2.18) and they are the same as in the time-harmonic regime. Zero initial boundary conditions have been applied, namely

$$V(X,0) = v(x,0) = 0, V_t(X,0) = v_t(x,0) = 0, \quad X \in D_1, x \in D_2, \tag{2.46}$$

The time dependent point load

$$F(t) = \sum_{i=1}^{6} \left[(-1)^{i+1} 10i \; e^{1000(t-0.08i)^2}\right] \tag{2.47}$$

is shown in Figure 2.8 and it has been applied at $X = 0$. Two geometries have been implemented in Finite Elements: a larger one with homogeneous properties $EJ = 1\,\mathrm{Pa}$, $\varrho A = 1\,\mathrm{kg/m}$ and $X \in [-20\,\mathrm{m}, 20\,\mathrm{m}]$ and a shorter one with the same homogeneous properties in $X \in [-4\,\mathrm{m}, 4\,\mathrm{m}]$ and PMLs in $|X| \in [4\,\mathrm{m}, 7\,\mathrm{m}]$. The transformation is given in Eq. (2.40) with $\alpha = 5$ and it is unchanged with respect to time-harmonic regime since it involves only a spatial transformation. The two initial boundary value problems have been solved in *Comsol Multiphysics®* using a backward differentiation formula; a total of $5s$ has been analyzed and standard convergence analysis has been considered on the time steps and element size; the initial step has been set to 10^{-4} and elements of uniform size $s = 5cm$ have been implemented.

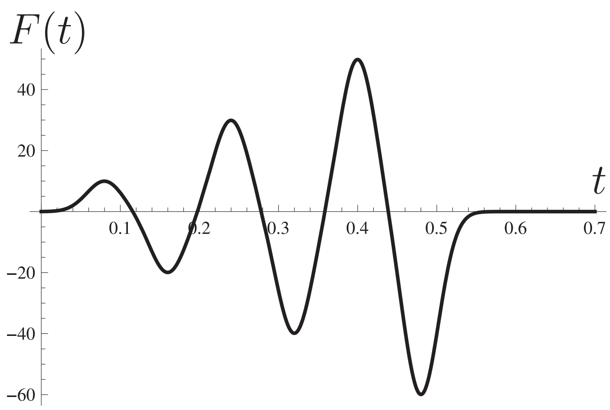

FIGURE 2.8: Time distribution of the point load applied at $X = 0$ in the transient analysis.

The transverse displacement is given in Figure 1.1 at $t = 0.5\,\mathrm{s}$, when the propagating wave has reached the fictitious boundary at $x_1 = \pm 7\mathrm{m}$ but not the boundaries $X = \pm 20\,\mathrm{m}$ for the larger domain. In the Figure only the region $X \in [-10\,\mathrm{m}, 10\,\mathrm{m}]$ is shown for visualization purposes. The comparison between the two numerical solutions evidences an excellent agreement in the central region where PML are not present. Such an example reveals the competitive behavior of the proposed technique in the transient regime; this is expected since only a spatial transformation $g(x)$ is implemented. Nevertheless, a complete analysis of the transient response requires a different type of study which is left for a future work.

Chapter 3

PML for flexural waves in Kirchhoff-Love plates

Here, we give the analytical form of PMLs for flexural waves in Kirchhoff-Love plates, we describe the implementation and we perform a deep quantitative analysis on the dependance of the perturbation on several parameters.

3.1 Equation of motion

We consider flexural vibrations in a thin Kirchhoff-Love plate as in Figure 3.1. The plate has thickness h, bending stiffness $B = Eh^3/(12(1-\nu^2))$, with E the Young's modulus and ν the Poisson's ratio, and density ϱ.

Time-harmonic regime is considered and the time dependence $e^{-i\omega t}$, with ω the radian frequency, is neglected in the following for simplicity. Transverse displacement is $W(\mathbf{X})$, where $\mathbf{X} = (X_1, X_2)$. Rotation is the vector $\mathbf{\Phi}(\mathbf{X}) = \nabla_{\mathbf{X}} W(\mathbf{X})$ and curvature is the tensor $\chi(\mathbf{X}) = \nabla_{\mathbf{X}} \nabla_{\mathbf{X}} W(\mathbf{X})$.

The static quantities are the bending moment symmetric tensor $\mathbf{M}$ and the shear force vector $\mathbf{V} = \nabla_{\mathbf{X}} \cdot \mathbf{M}$. The constitutive relation between the bending moment tensor $\mathbf{M}$ and the curvature $\chi(\mathbf{X})$ is given by

$$\mathbf{M} = -\mathbb{D}^{(0)} \chi \tag{3.1}$$

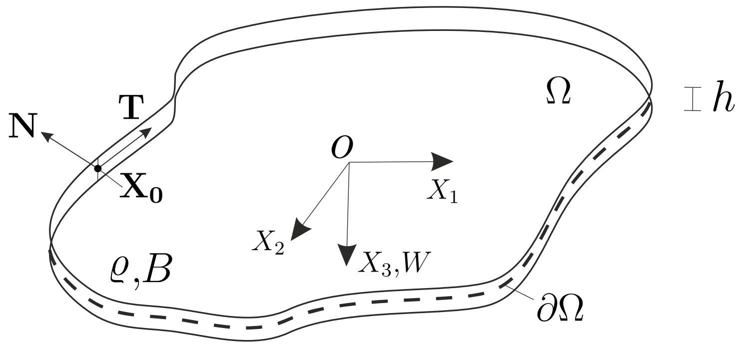

FIGURE 3.1: Plate structure. The transverse displacement, in direction X_3, is W. The plate has thickness h, bending stiffness B and density ϱ.

where, for isotropic plates, the constitutive tensor $\mathbb{D}^{(0)}$ has components

$$\mathbb{D}^{(0)}_{IJKL} = B\left[\nu\,\delta_{IJ}\delta_{KL} + \frac{1-\nu}{2}(\delta_{IK}\delta_{JL} + \delta_{IL}\delta_{JK})\right], \quad (I,J,K,L=1,2), \tag{3.2}$$

with δ_{IJ} the Kronecker delta.

Explicitly, the moment-curvature relations are:

$$\begin{aligned} M_{11} &= -B\left(W_{,11} + \nu W_{,22}\right), \\ M_{22} &= -B\left(W_{,22} + \nu W_{,11}\right), \\ M_{12} &= -B(1-\nu)W_{,12}, \end{aligned} \tag{3.3}$$

where M_{IJ} $(I,J=1,2)$ are the components of the moment tensor.

Then, the equation of motion for the plate in the domain Ω has the form

$$\nabla_{\mathbf{X}}\cdot[\nabla_{\mathbf{X}}\cdot\mathbf{M}(\mathbf{X})] + \varrho h\omega^2 W(\mathbf{X}) = \nabla_{\mathbf{X}}\cdot\mathbf{V}(\mathbf{X}) + \varrho h\omega^2 W(\mathbf{X}) = 0, \tag{3.4}$$

which, in the isotropic case, simplifies to the well-known bi-harmonic form

$$(\nabla^2_{\mathbf{X}}\nabla^2_{\mathbf{X}} - \beta^4)W(\mathbf{X}) = 0, \qquad \beta^4 = \frac{\varrho h}{B}\omega^2. \tag{3.5}$$

3.1.1 Boundary conditions

At a point $\mathbf{X}_0$ on the boundary $\partial\Omega$, having normal $\mathbf{N}$ and tangent $\mathbf{T}$, the essential boundary conditions are imposed on $W(\mathbf{X}_0)$ and $\Phi_N(\mathbf{X}_0) = \nabla_{\mathbf{X}}W(\mathbf{X}_0)\cdot\mathbf{N}$ and the natural boundary conditions are imposed on $M_{NN}(\mathbf{X}_0) = \mathbf{M}(\mathbf{X}_0)\mathbf{N}\cdot\mathbf{N}$ and $R_N(\mathbf{X}_0) = \mathbf{R}(\mathbf{X}_0)\cdot\mathbf{N}$, with $\mathbf{R} = \mathbf{V} + \nabla_{\mathbf{X}}\mathbf{M}(\mathbf{T}\otimes\mathbf{T})$ (see, for example, [115]). [1]

3.2 Perfect Boundary Conditions

A common approach implemented to cancel reflection is the definition of non-reflecting boundary conditions. Here we show that, consistently with problem governed by Helmholtz equations, non reflecting conditions depend on the incident wave and, therefore, are not an optimal solution strategy.

We consider a wave reflected by a straight boundary at $X_1 = a$. The general solution of Eq. (3.5) is $W(\mathbf{X}) = e^{ik_2X_2}(Q_1e^{ik_1X_1} + Q_2e^{-k_1X_1} + Q_3e^{-ik_1X_1} + Q_4e^{k_1X_1})$ representing propagating and evanescent waves in direction $\pm X_1$ and a propagating wave in direction X_2, with the wave vector $\mathbf{k} = (k_1, k_2)$.

The essential and natural boundary conditions at $X_1 = a$ are

$$
\begin{aligned}
W(a, X_2) &= \overline{W}e^{ik_2X_2},\\
\Phi_1(a, X_2) &= \overline{\Phi}_1e^{ik_2X_2},\\
M_{11}(a, X_2) &= \overline{M}_{11}e^{ik_2X_2},\\
R_1(a, X_2) = V_1(a, X_2) + M_{12,2}(a, X_2) &= \overline{R}_1e^{ik_2X_2},
\end{aligned}
\tag{3.6}
$$

where $\overline{W}$, $\overline{\Phi}_1$, $\overline{M}_{11}$ and $\overline{R}_1$ are values at $X_1 = a$.

The boundary conditions (3.6) can be written in the partitioned form

$$
\left[\begin{array}{c|c} \mathbf{A}_{11} & \mathbf{A}_{12} \\ \hline \mathbf{A}_{21} & \mathbf{A}_{22} \end{array}\right]
\left(\begin{array}{c} \mathbf{q}_1 \\ \hline \mathbf{q}_2 \end{array}\right) =
\left(\begin{array}{c} \mathbf{c}_1 \\ \hline \mathbf{c}_2 \end{array}\right)
\tag{3.7}
$$

where

$$
\begin{aligned}
\mathbf{q}_1 &= \begin{pmatrix} Q_1 \\ Q_2 \end{pmatrix}, \quad \mathbf{q}_2 = \begin{pmatrix} Q_3 \\ Q_4 \end{pmatrix},\\
\mathbf{c}_1 &= \begin{pmatrix} \overline{W} \\ \overline{\Phi}_1 \end{pmatrix}, \quad \mathbf{c}_2 = \begin{pmatrix} \overline{M}_{11} \\ \overline{R}_1 \end{pmatrix},
\end{aligned}
\tag{3.8}
$$

[1] In index notation $[\nabla_{\mathbf{X}}\mathbf{M}(\mathbf{T}\otimes\mathbf{T})\cdot\mathbf{N}]_N = M_{NT,T}$.

and

$$\mathbf{A}_{11} = \begin{bmatrix} e^{ik_1a} & e^{-k_1a} \\ ik_1e^{ik_1a} & -k_1e^{-k_1a} \end{bmatrix},$$

$$\mathbf{A}_{12} = \begin{bmatrix} e^{-ik_1a} & e^{k_1a} \\ -ik_1e^{-ik_1a} & k_1e^{k_1a} \end{bmatrix},$$

$$\mathbf{A}_{21} = B \begin{bmatrix} e^{ik_1a}(k_1^2 + \nu k_2^2) & -e^{-k_1a}(k_1^2 - \nu k_2^2) \\ i\,k_1e^{ik_1a}[k_1^2 + (2-\nu)k_2^2] & k_1e^{-k_1a}[k_1^2 - (2-\nu)k_2^2] \end{bmatrix},$$

$$\mathbf{A}_{22} = B \begin{bmatrix} e^{-ik_1a}(k_1^2 + \nu k_2^2) & -e^{k_1a}(k_1^2 - \nu k_2^2) \\ -ik_1\,e^{-ik_1a}[k_1^2 + (2-\nu)k_2^2] & -k_1e^{k_1a}[k_1^2 - (2-\nu)k_2^2] \end{bmatrix}. \tag{3.9}$$

The solution $\mathbf{q}_1 = \mathbf{A}_{11}^{-1}[\mathbf{c}_1 - \mathbf{A}_{12}\,\mathbf{q}_2]$ of the first pair of equations in (3.7) can be substitute in the second pair of equations, yielding

$$(\mathbf{A}_{22} - \mathbf{A}_{21}\mathbf{A}_{11}^{-1}\mathbf{A}_{12})\,\mathbf{q}_2 = \mathbf{c}_2 - \mathbf{A}_{21}\mathbf{A}_{11}^{-1}\mathbf{c}_1. \tag{3.10}$$

Then, zero reflection corresponds to $\mathbf{q}_2 = \mathbf{0}$, i.e. $Q_3 = Q_4 = 0$, a condition resulting from

$$\mathbf{c}_2 = \mathbf{A}_{21}\mathbf{A}_{11}^{-1}\mathbf{c}_1, \tag{3.11}$$

provided that

$$\det[\mathbf{A}_{22} - \mathbf{A}_{21}\mathbf{A}_{11}^{-1}\mathbf{A}_{12}] \neq 0 \text{ and } \det[\mathbf{A}_{11}] \neq 0. \tag{3.12}$$

Note that we impose equal to zero not only the reflected propagating wave ($Q_3 = 0$) as in [90], but also the reflected evanescent wave ($Q_4 = 0$) associated with short range effects.

The two scalar conditions in (3.11) express the natural boundary conditions $\overline{M}_{11}$ and $\overline{R}_1$ as a function of the essential boundary conditions $\overline{W}$ and $\overline{\Phi}_1$. The explicit expressions are

$$\begin{aligned} \overline{M}_{11} &= B\left[(-ik_1^2 + \nu k_2^2)\overline{W} + (1-i)k_1\overline{\Phi}_1\right], \\ \overline{R}_1 &= B\left[(1+i)k_1^3\overline{W} + (ik_1^2 + k_2^2(2-\nu))\overline{\Phi}_1\right]. \end{aligned} \tag{3.13}$$

As opposite to flexural waves in one-dimensional beam structures [77], given in

Chapter 2, perfect boundary conditions (3.13) for plates depend on the direction of the incident wave, namely on the wave vector components k_1 and k_2. Therefore, it is not possible to obtain a set of relations independent on the incident wave, solution of a specific boundary value problem. In the following, we outline a different approach based on geometry transformation.

3.3 Transformed Equation of Motion

We introduce a smooth coordinate transformation $\mathbf{x} = \mathbf{G}(\mathbf{X})$ and we indicate with $\mathbf{g}(\mathbf{x})$ the inverse transformation from $\mathbf{x}$ to $\mathbf{X}$. Transformation gradients are defined as $\mathbf{F} = \nabla_{\mathbf{X}}\mathbf{G}$ and $\mathbf{f} = \nabla\mathbf{g} = \mathbf{F}^{-1}$, with Jacobians $J = \det(\mathbf{F})$ and $j = \det(\mathbf{f}) = J^{-1}$. Gradient operators are related by

$$\nabla = \mathbf{f}\,\nabla_{\mathbf{X}}. \tag{3.14}$$

Applying coordinate transformation, the transformed equation of motion (see [20, 33, 77]) takes the form

$$\nabla\cdot[\nabla\cdot\mathbf{m}(\mathbf{x}) + \mathbf{p}\nabla w(\mathbf{x})] + \rho h\,\omega^2 w(\mathbf{x}) = 0. \tag{3.15}$$

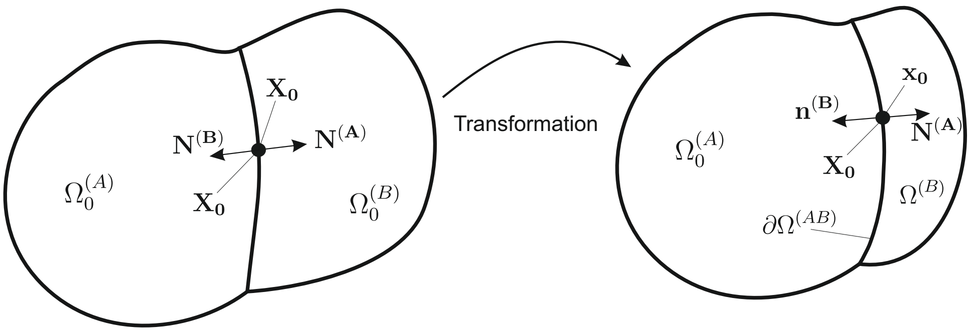

FIGURE 3.2: Geometric transformation of the domain $\Omega_0^{(B)}$ into the domain $\Omega^{(B)}$. The domain $\Omega_0^{(A)}$ is not transformed.

In Eq. (3.15) we assume the transformed transverse displacement $w(\mathbf{x}) = w(\mathbf{G}(\mathbf{X})) = W(\mathbf{X})$. The moment-curvature relation is transformed into

$$\mathbf{m}(\mathbf{x}) = -\mathbb{D}(\mathbf{x})\nabla\nabla w(\mathbf{x}), \tag{3.16}$$

where the inhomogeneous anisotropic constitutive tensor has components

$$\mathbb{D}_{ijkl} = \frac{1}{J} F_{iI} F_{jJ} F_{kK} F_{lL} \, \mathbb{D}^{(0)}_{IJKL}. \tag{3.17}$$

Shear forces are $\mathbf{v}(\mathbf{x}) = \nabla \cdot \mathbf{m}(\mathbf{x})$ and the density is transformed as

$$\rho = \varrho / J. \tag{3.18}$$

Finally, we note that it is possible to give a physical meaning to the transformed equation (3.15) by defining the longitudinal axial force tensor $\mathbf{p}(\mathbf{x})$ having components

$$\begin{aligned} p_{kl} = \mathbb{D}^{(0)}_{IJKL} \Bigg\{ \left(\frac{1}{J} F_{iI} F_{jJ,i} F_{kK} F_{lL} \right)_{,j} - \frac{1}{J} F_{jJ} \Big[F_{lI} (F_{kK,i} F_{iL})_{,j} + \\ F_{kI} (F_{lK,i} F_{iL})_{,j} + \frac{1}{2} (F_{lI,j} F_{kK,i} F_{iL} + F_{kI,j} F_{lK,i} F_{iL}) \Big] \Bigg\}. \end{aligned} \tag{3.19}$$

We note that a physical interpretation is not a necessary condition for the PML, which is a numerical artifice introduced to have a finite domain without reflection. Nevertheless, we are going to show that such an interpretation is useful during the implementation in a numerical code; in addition, it can be used as a guide in the creation of absorbing layers in experimental devices.

3.3.1 Interface conditions

Geometric transformation and the physical interpretation of the transformed equation of motion introduce a specific definition of the transformed fields, which affect continuity conditions on the boundary of the domains where transformation is applied. Here, we detail the constraints on the transformation law that have to be imposed in order to satisfy automatically the interface and the boundary conditions. We start focussing on the interface between the untransformed domain $\Omega_0^{(A)}$ and the transformed domain $\Omega^{(B)}$ and we consider the continuity conditions at a point $\mathbf{X}_0$ on the boundary $\partial\Omega_0^{(A)}$, with normal $\mathbf{N}^{(A)}(\mathbf{X}_0)$ (see Figure 3.2). The point $\mathbf{X}_0$ coincides with the point $\mathbf{x}_0$ on the boundary $\partial\Omega^{(B)}$, with normal $\mathbf{N}^{(B)} = -\mathbf{N}^{(A)} = \mathbf{N}$. After transformation the normal vector $\mathbf{N}$ transforms following Nanson's formula $\mathbf{n} = J(\mathbf{X}_0)\mathbf{F}(\mathbf{X}_0)^{-T}\mathbf{N} = j^{-1}(\mathbf{x}_0)\mathbf{f}^T(\mathbf{x}_0)\mathbf{N}$, where we have indicated $\mathbf{n}^{(B)}$ with $\mathbf{n}$ for ease of notation. Since the point $\mathbf{X}_0$ before transformation must coincide with the point $\mathbf{x}_0$ after transformation

$$\mathbf{x}_0 = \mathbf{g}(\mathbf{x}_0), \qquad \text{or} \qquad \mathbf{G}(\mathbf{X}_0) = \mathbf{X}_0. \tag{3.20}$$

Additionally, since $\mathbf{N}(\mathbf{X}_0) = \mathbf{n}(\mathbf{x}_0)$ the condition

$$tr\mathbf{F}(\mathbf{X}_0) = 1 + J, \qquad \text{or} \qquad tr\mathbf{f}(\mathbf{x}_0) = 1 + j, \tag{3.21}$$

must be satisfied. Clearly, conditions (3.20) and (3.21) are satisfied by $\mathbf{f}(\mathbf{x}_0) = \mathbf{F}(\mathbf{X}_0) = \mathbf{I}$ and the absence of any translation in $\mathbf{X}_0 = \mathbf{x}_0$.

Indicating with (A) and (B) the fields in the domains $\Omega_0^{(A)}$ and $\Omega^{(B)}$, respectively, we have the following essential conditions

$$\begin{cases} W^{(A)}(\mathbf{X}_0) = w^{(B)}(\mathbf{x}_0), \\ \Phi_N^{(A)}(\mathbf{X}_0) = \phi_n^{(B)}(\mathbf{x}_0) = \nabla w^{(B)}(\mathbf{x}_0) \cdot \mathbf{n}, \end{cases} \tag{3.22}$$

and natural conditions

$$\begin{cases} M_{NN}^{(A)}(\mathbf{X}_0) = m_{nn}^{(B)}(\mathbf{x}_0) = \mathbf{m}^{(B)}(\mathbf{x}_0)\mathbf{n} \cdot \mathbf{n}, \\ R_N^{(A)}(\mathbf{X}_0) = r_n^{(B)}(\mathbf{x}_0), \end{cases} \tag{3.23}$$

on the interface $\partial\Omega^{(AB)} = \Omega_0^{(A)} \cap \Omega^{(B)}$. In Eq. (3.23) $R_N^{(A)} = \mathbf{R}^{(A)} \cdot \mathbf{N}$ and $r_n^{(B)} = \mathbf{r}^{(B)} \cdot \mathbf{n}$, with $\mathbf{r}^{(B)} = \mathbf{v}^{(B)} + \nabla\mathbf{m}^{(B)}(\mathbf{t} \otimes \mathbf{t}) + \mathbf{p}^{(B)}\nabla w^{(B)}$.

Conditions for transformed fields in $\Omega^{(B)}$ can be expressed in term of original untransformed coordinates $\mathbf{X} = \mathbf{g}(\mathbf{x})$ in the untransformed domain $\Omega_0^{(B)}$. We impose that in the untransformed domain, interface conditions must be satisfied automatically since the material in $\Omega_0^{(A)} \cup \Omega_0^{(B)}$ is homogeneous.

Then, in $\mathbf{X}_0$

$$\phi_n^{(B)} = J\nabla_{\mathbf{X}} W^{(B)} \cdot \mathbf{F}^{-1}\mathbf{F}^{-T}\mathbf{N} = j^{-1}\nabla_{\mathbf{X}} W^{(B)} \cdot \mathbf{f}\,\mathbf{f}^T\mathbf{N} \tag{3.24}$$

and

$$\phi_n^{(B)} = \Phi_N^{(B)} \qquad \text{if} \qquad \mathbf{f}(\mathbf{x}_0) = \mathbf{F}(\mathbf{X}_0) = \mathbf{I}. \tag{3.25}$$

Also, $M^{(B)}_{NN} = m^{(B)}_{nn}$ if

$$
\begin{aligned}
&(N_1^2 + \nu N_2^2) f_{11,1} + (1-\nu) N_1 N_2 f_{11,2} + (\nu N_1^2 + N_2^2) f_{12,2} = 0,\\
&(N_1^2 + \nu N_2^2) f_{21,1} + (1-\nu) N_1 N_2 f_{21,2} + (\nu N_1^2 + N_2^2) f_{22,2} = 0,
\end{aligned} \tag{3.26}
$$

which are satisfied by the sufficient condition

$$
\nabla \mathbf{f}(\mathbf{x}_0) = \mathbf{0} \qquad \text{or} \qquad \nabla_{\mathbf{X}} \mathbf{F}(\mathbf{X}_0) = \mathbf{0}. \tag{3.27}
$$

Finally $r^{(B)}_n = R^{(B)}_N$, if the lengthy expression

$$
\begin{aligned}
&\mathbb{D}^{(0)}_{IJKL} F_{jJ} F_{kK} F_{jJ,i} F_{lL} f_{Mk,lj} f_{Mk,lj} N_I W_{,M} +\\
&F_{jJ} F_{jN} \mathbb{D}^{(0)}_{MJKL} F_{kK} F_{mO} F_{lL} f_{Pk,lm} N_M T_N T_O W_{,P}\\
&+ \Big(\mathbb{D}^{(0)}_{IJNM} F_{iI} F_{jJ,ij} - \mathbb{D}^{(0)}_{MJKL} F_{jJ} F_{kK,il} f_{Nk} F_{iL}\\
&- \mathbb{D}^{(0)}_{NJKL} f_{Ml} F_{jJ} F_{lK,ij} F_{iL} \Big) W_{,M} N_N = 0.
\end{aligned} \tag{3.28}
$$

involving first and second gradient of $\mathbf{f}$, or $\mathbf{F}$, is set to zero. Such expression is satisfied by

$$
\nabla \nabla \mathbf{f}(\mathbf{x}_0) = \mathbf{0} \qquad \text{and} \qquad \nabla \mathbf{f}(\mathbf{x}_0) = \mathbf{0} \tag{3.29}
$$

or

$$
\nabla_{\mathbf{X}} \nabla_{\mathbf{X}} \mathbf{F}(\mathbf{X}_0) = \mathbf{0} \qquad \text{and} \qquad \nabla_{\mathbf{X}} \mathbf{F}(\mathbf{X}_0) = \mathbf{0}. \tag{3.30}
$$

To summarize, we stress that the conditions

$$
\begin{cases}
\mathbf{f}(\mathbf{x}_0) = \mathbf{I},\\
\nabla \mathbf{f}(\mathbf{x}_0) = \mathbf{0},\\
\nabla \nabla \mathbf{f}(\mathbf{x}_0) = \mathbf{0},
\end{cases} \tag{3.31}
$$

on the geometric transformation, assure that the boundary fields remain unchanged. Such constraints must be intended as sufficient conditions in order to avoid any reflection. In principle, less restrictive conditions could be find.

By assuring that the relevant boundary fields remain unchanged, it is also guaranteed that the same boundary conditions (simple support, clamped, free, etc.) are imposed before and after the transformation; a property that will be used in the next Section to show the invariance of eigenfrequencies after transformation.

Transformed bending stiffness and linear density, defined in Eqs. (3.17) and (3.18) respectively, are homogeneous only for affine transformations. However, the only admissible affine transformation is the identity in view of the constraints $\mathbf{f}(\mathbf{x}_0) = \mathbf{I}$ and $\mathbf{g}(\mathbf{x}_0) = \mathbf{x}_0$, which means that a inhomogeneous material is needed in the transformed domain.

3.4 Eigenfrequency Anlaysis

We show a comparison between eigenfrequency analyses for plates before and after transformation. Such examples are a useful tool to check the error-free implementation of the PML in a numerical code and they fully show the correct physical interpretation of the transformed equations, which involves both the equation of motion and the boundary conditions.

Here we compare eigenfrequencies and eigenmodes between a homogeneous rectangular plate with edges of length $2A_1$ and $2A_2$ and a second inhomogeneous rectangular plate with edges of length $2a_1$ and $2a_2$. The inhomogeneous plate is obtained transforming the domains $A_{i+2} \leq |X_i| \leq A_i$ into the domains $A_{i+2} \leq |x_i| \leq a_i$, $i = 1, 2$, as shown in Figure 3.3. In particular, defining the monotonically increasing function

$$\eta_\pm(x_i) = x_i + (1-\zeta)(a_i - A_{i+2})\left(\mp 35\tilde{x}_i^4 + 84\tilde{x}_i^5 \mp 70\tilde{x}_i^6 + 20\tilde{x}_i^7\right),$$
$$\tilde{x}_i = \frac{x_i \mp A_{i+2}}{a_i - A_{i+2}}, \qquad \zeta = \frac{A_i - A_{i+2}}{a_i - A_{i+2}}, \qquad i = 1, 2, \tag{3.32}$$

with $a_i > A_{i+2}$, we apply the transformations

$$g_1(\mathbf{x}) = \begin{cases} \bar{\eta}_-(x_1) & \text{in } \Omega^{(1)},\ \Omega^{(4)},\ \Omega^{(7)}, \\ x_1 & \text{in } \Omega^{(2)},\ \Omega^{(5)},\ \Omega^{(8)}, \\ \bar{\eta}_+(x_1) & \text{in } \Omega^{(3)},\ \Omega^{(6)},\ \Omega^{(9)}, \end{cases} \tag{3.33}$$

and the transformations

$$g_2(\mathbf{x}) = \begin{cases} \bar{\eta}_+(x_2) & \text{in } \Omega^{(1)},\ \Omega^{(2)},\ \Omega^{(3)}, \\ x_2 & \text{in } \Omega^{(4)},\ \Omega^{(5)},\ \Omega^{(6)}, \\ \bar{\eta}_-(x_2) & \text{in } \Omega^{(7)},\ \Omega^{(8)},\ \Omega^{(9)}, \end{cases} \tag{3.34}$$

with $\bar{\eta}_\pm(x_i) = \eta_\pm(x_i)$.

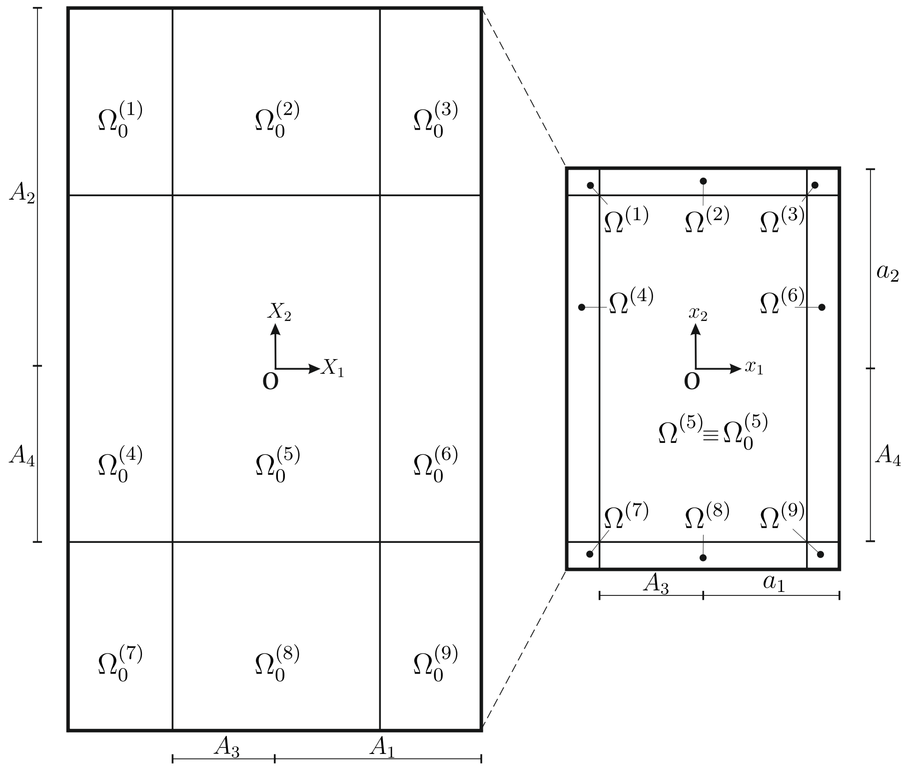

FIGURE 3.3: Geometry of a plate before and after coordinate transformation. The domains $\Omega_0^{(1)}, \cdots, \Omega_0^{(4)}, \Omega_0^{(6)}, \cdots, \Omega_0^{(9)}$ are trasformed into the domains $\Omega^{(1)}, \cdots, \Omega^{(4)}, \Omega^{(6)}, \cdots, \Omega^{(9)}$, as described in Eqs. (3.33) and (3.34). The lengths A_1 and A_2 are transformed into a_1 and a_2, respectively, while A_3 and A_4 remain unchanged after transformation.

The transformation ratio ζ in $\eta_\pm$ indicates the geometrical transformation of the PML region, so that an initial layer of thickness $A_1 - A_3$ is shrunk into a layer of thickness $(a_1 - A_3) < (A_1 - A_3)$ when $\zeta > 1$, while, for $\zeta = 1$, no transformation is introduced.

The septic polynomial transformation (3.32) is obtained as follows. Restricting the attention to the domain $\Omega^{(6)}$, we note that the transformation $\mathbf{g}(\mathbf{x})$ satisfies conditions (3.31) at $\mathbf{x}_0 = (A_3\ x_2)^T$, $|x_2| \leq A_2$, reducing to the 3 scalar conditions $\eta_+'(A_3) = 1$, $\eta_+''(A_3) = \eta_+'''(A_3) = 0$ and assuring the absence of reflection at the interface $\partial\Omega^{(5,6)}$ between $\Omega^{(5)}$ and $\Omega^{(6)}$.

The fourth condition $\mathbf{g}(\mathbf{x}_0) = \mathbf{x}_0$, reducing to $\eta_+(A_3) = A_3$, imposes that $\Omega^{(5)}$ and $\Omega^{(6)}$ share the same boundary $\partial\Omega^{(5,6)}$.

Additional conditions are imposed at $\mathbf{x}_0 = (a_1\ x_2)^T$, $|x_2| \leq A_2$, in order to assure that the initial simply supported boundary condition, normal rotation $\Phi_1(\mathbf{g}(\mathbf{x}_0))$ and reaction force $R_1(\mathbf{g}(\mathbf{x}_0))$ remain unchanged after transformation. Conditions

(3.31) at $\mathbf{x}_0 = (a_1\ x_2)^T$ have the explicit form $\eta'_+(a_1) = 1$, $\eta''_+(a_1) = \eta'''_+(a_1) = 0$. The final condition $\mathbf{g}(\mathbf{x}_0) = \mathbf{X}_0$, with $\mathbf{X}_0 = (A_1\ X_2)^T$, which reduces to $\eta_+(a_1) = A_1$, imposes the transformation ratio ζ.

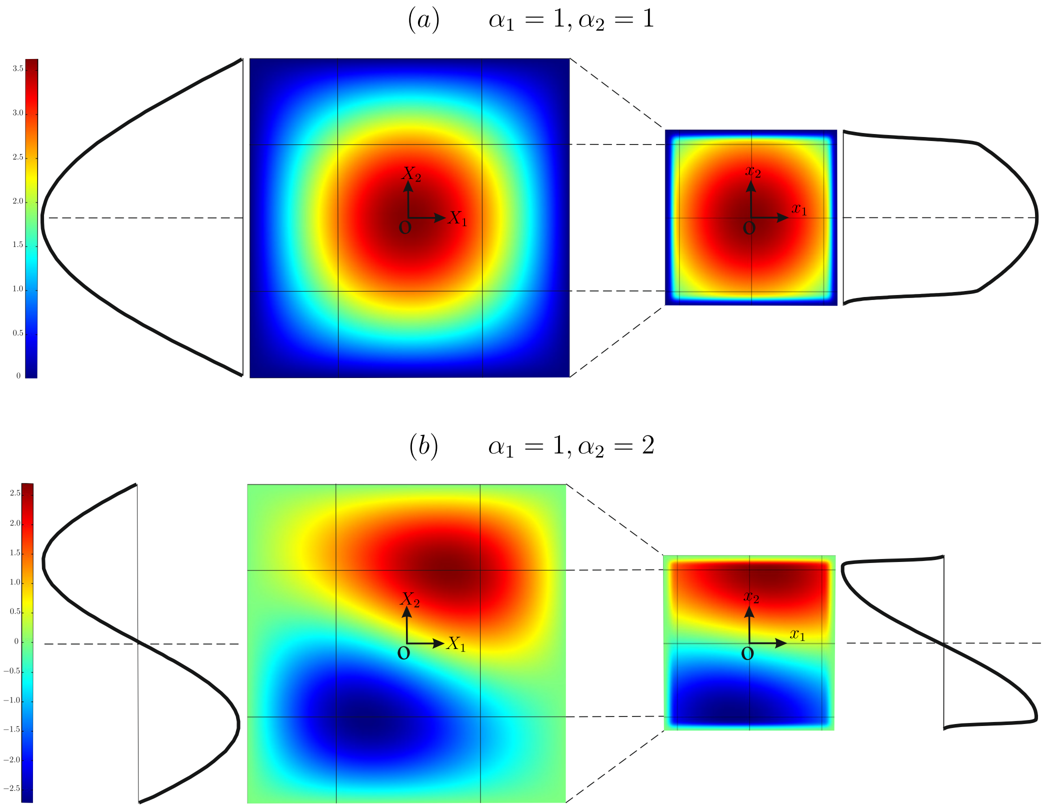

FIGURE 3.4: Eigenmodes of homogeneous (left column) and transformed inhomogeneous (right column) square plates. Contour plots of the transverse displacement and displacement distribution along vertical direction for $X_1 = x_1 = 0$ are shown. The structures have been implemented in *Comsol Multiphysics*® and the plates have edge lengths $A = 10$ m and $a = 6$ m, respectively. Numerical values of the natural frequencies: (a) $\bar{\omega}_{11} = 0.937263$ rad/sec — homogeneous plate — and $\bar{\omega}_{11} = 0.939462$ rad/sec — inhomogeneous plate —. (b) $\bar{\omega}_{12} = 2.34325$ rad/sec — homogeneous plate — and $\bar{\omega}_{12} = 2.34501$ rad/sec — inhomogeneous plate —.

For the homogeneous simply supported plate, natural frequencies are given by $\omega_{\alpha_1\alpha_2} = \pi^2(\alpha_1^2/A_1^2 + \alpha_2^2/A_2^2)\sqrt{B/(\varrho h)}$ and the corresponding eigenmodes are $W_{\alpha_1\alpha_2}(\mathbf{X}) = \sin[\frac{\alpha_1\pi}{2A_1}(X_1+A_1)]\ \sin[\frac{\alpha_2\pi}{2A_2}(X_2+A_2)]$, with α_1, α_2 positive integer numbers (see, for example [56]).

The solution $e^{ik_\imath X_\imath}$ ($\imath = 1$ or 2) of the untransformed equation of motion (3.5) is transformed into the solution $e^{ik_\imath g_\imath(\mathbf{x})}$ of the transformed equation of motion (3.15).

The solution is obtained studying only one quarter of the plate, i.e. $0 \le |x_i| \le a_i$, $i = 1, 2$, and applying symmetric and antisymmetric conditions at x_1, $x_2 = 0$. The final solution can be found solving before in x_2-direction (one solution for

$0 \leq x_2 \leq A_2/2$ and another one for $A_2/2 \leq x_2 \leq a_2$, with 4 boundary and 4 interface conditions) and then in x_1 direction (one solution for $0 \leq x_1 \leq A_1/2$ and another one for $A_1/2 \leq x_1 \leq a_1$, with 4 boundary and 4 interface conditions) in order to obtain the characteristic equation giving the natural frequencies.

Then, it is easy to show that exactly the same natural frequencies are obtained and the eigenmodes are $w_{\alpha_1\alpha_2}(\mathbf{x}) = \xi_{\alpha_1}(x_1)\xi_{\alpha_2}(x_2)$, where

$$\xi_{\alpha_1}(x_1) = \begin{cases} \sin\left[\frac{\alpha_1\pi}{2A_1}\left(\eta_-(x_1) + A_1\right)\right] & \text{in } \Omega^{(1)},\ \Omega^{(4)},\ \Omega^{(7)}, \\ \sin\left[\frac{\alpha_1\pi}{2A_1}\left(x_1 + A_1\right)\right] & \text{in } \Omega^{(2)},\ \Omega^{(5)},\ \Omega^{(8)}, \\ \sin\left[\frac{\alpha_1\pi}{2A_1}\left(\eta_+(x_1) + A_1\right)\right] & \text{in } \Omega^{(3)},\ \Omega^{(6)},\ \Omega^{(9)}, \end{cases} \tag{3.35}$$

and

$$\xi_{\alpha_2}(x_2) = \begin{cases} \sin\left[\frac{\alpha_2\pi}{2A_2}\left(\eta_+(x_2) + A_2\right)\right] & \text{in } \Omega^{(1)},\ \Omega^{(2)},\ \Omega^{(3)}, \\ \sin\left[\frac{\alpha_2\pi}{2A_2}\left(x_2 + A_2\right)\right] & \text{in } \Omega^{(4)},\ \Omega^{(5)},\ \Omega^{(6)}, \\ \sin\left[\frac{\alpha_2\pi}{2A_2}\left(\eta_-(x_2) + A_2\right)\right] & \text{in } \Omega^{(7)},\ \Omega^{(8)},\ \Omega^{(9)}, \end{cases} \tag{3.36}$$

with α_1, α_2 positive integer numbers. The analytical expression of the eigenmodes shows that the transformation introduces a shift in the displacement so that $W(\mathbf{X}) = w(\mathbf{x})$.

The eigenfreqeuncy analysis has also been performed in a Finite Element (FEM) code and the homogeneous and inhomogeneous plates have been implemented in *Comsol Multiphysics*®. In the implementation $A_1 = 6$ m, $A_2 = 10$ m, $a_1 = 4$ m, $a_2 = 6$ m, while the others material and geometrical parameters are $\rho = 1.32$ kg/m^3, $E = 1.3 * 10^7$ Pa, $\nu = 0.3$, $h = 0.02$ m, corresponding to $B = 9.524$ Nm. A maximum size $s = 0.02$ m was imposed for the three-nodes triangular elements. Natural frequencies and corresponding eigenmodes were obtained and a maximum relative difference $(\bar{\omega}_{\alpha_1\alpha_2} - \omega_{\alpha_1\alpha_2})/\omega_{\alpha_1\alpha_2} = 0.003\%$ was found between the numerically computed natural frequencies $\bar{\omega}_{\alpha_1\alpha_2}$ and the analytical values $\omega_{\alpha_1\alpha_2}$.

In Figure 3.4 we show the special case of a square plate, where $A = A_1 = A_2 = 10$ m, $A_3 = A_4 = A/2$ and $a = a_1 = a_2 = 6$ m. For a square plate, since eigenfrequencies $\omega_{\alpha_1\alpha_2} = \omega_{\alpha_2\alpha_1}$ coincide, the resulting eigenmodes are a linear combinations of the previously described eigenmodes. The aforementioned correspondence between natural frequencies and eigenmodes before and after transformation is shown. In particular, $\omega_{11} = 0.937288$ rad/sec and $\omega_{12} = 2.34322$ rad/sec with a maximum relative difference of 0.23%.

3.4.1 Additional examples

We consider some additional examples. A homogeneous rectangular plate with edges of length $2A_1$ and $2A_2$ is transformed into a second inhomogeneous rectangular plate with edges of length $2a_1$ and $2a_2$. The inhomogeneous plate is obtained transforming the domains $A_{i+2} \leq |X_i| \leq A_i$ into the domains $A_{i+2} \leq |x_i| \leq a_i$, $i = 1, 2$ (see Figure 3.5).

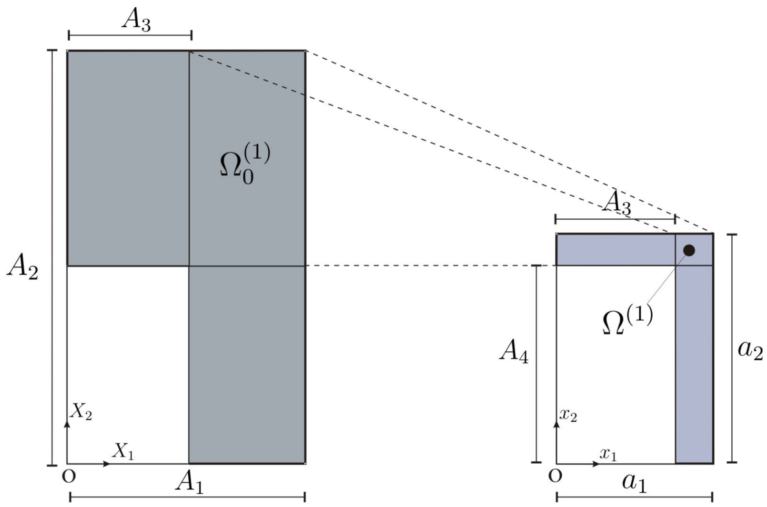

FIGURE 3.5: Geometric transformation of the rectangular plate.

The isotropic homogeneous structure has eigenfrequencies $\omega_{n_1 n_2} = \pi^2(n_1^2/A_1^2 + n_2^2/A_2^2)\sqrt{B/(\varrho h)}$ and corresponding eigenmodes $W_{n_1 n_2}(\mathbf{X}) = \sin[\frac{n_1 X_1 \pi}{A_1}]\,\sin[\frac{n_2 \pi X_2}{A_2}]$, with n_1, n_2 positive integer numbers.

We computed numerically eigenfrequencies and eigenmodes for untransformed and transformed plates and we show that the two structures have the same eigenfrequencies while the eigenmodes for the transform domains satisfy $w(\mathbf{x}) = w(\mathbf{G}(\mathbf{X})) = W(\mathbf{X})$.

The eigenfrequencies are reported in Table 3.1.

We also consider a transformation that does not satisfy the above-mentioned constraints in order not to perturb the boundary conditions. In particular, the usually

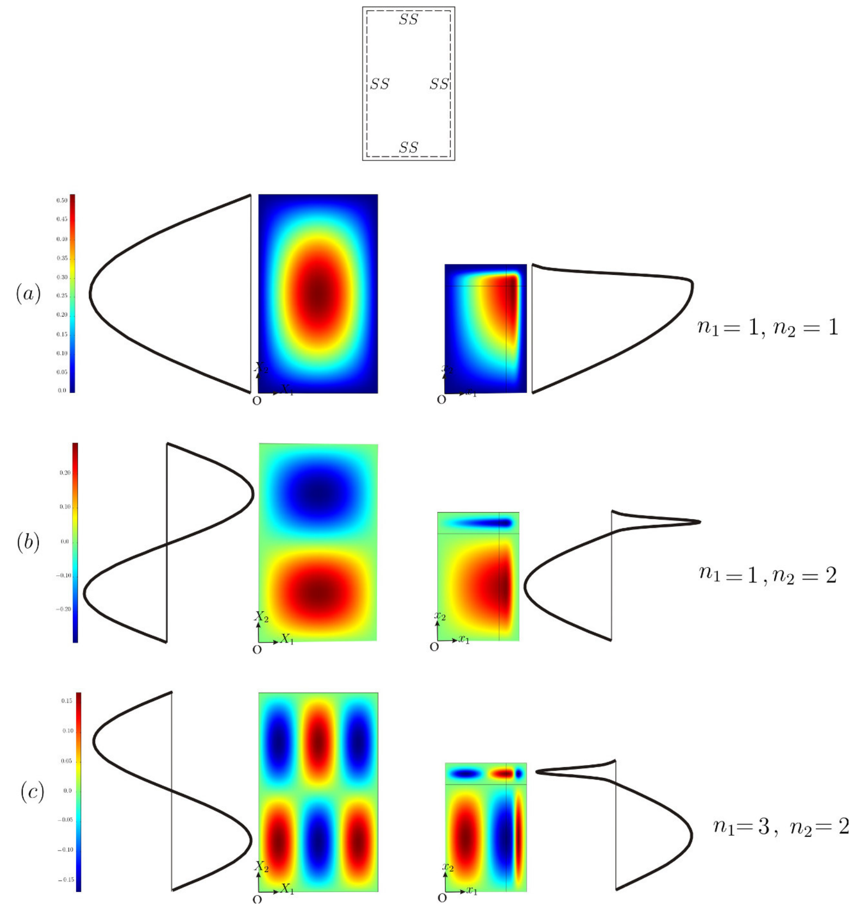

FIGURE 3.6: Eigenmodes of homogeneous (left column) and inhomogeneous (right column) rectangular plate. Contour plots of transverse displacement and displacement distribution along $X_1 = x_1 = A_3 = 6$ m are shown. Simply-supported (SS) boundary conditions are considered. (a) $n_1 = n_2 = 1$, $\omega_{11} = 7.08173$ rad/sec . (b) $n_1 = 1$, $n_2 = 2$, $\omega_{12} = 12.7055$ rad/sec. (c) $n_1 = 3$, $n_2 = 2$, $\omega_{32} = 54.3627$ rad/sec.

	Analytical Homogenoeus	Numerical Homogenoeus	Numerical Transformed
$n_1 = 1$, $n_2 = 1$	7.08173	7.08178	7.08555
$n_1 = 1$, $n_2 = 2$	12.7055	12.7052	12.7172
$n_1 = 1$, $n_2 = 3$	22.0783	22.0785	22.1099
$n_1 = 3$, $n_2 = 2$	54.3627	54.3627	54.3697

TABLE 3.1: Comparison between eigenfrequencies for the simply supported plate.

adopted linear transformation law is

$$g_\imath(x_\imath) = \frac{A_\imath - A_{\imath+2}}{a_\imath - A_{\imath+2}} x_\imath + \frac{a_\imath - A_\imath}{a_\imath - A_{\imath+2}} A_{\imath+2}, \qquad \imath = 1, 2. \tag{3.37}$$

Homogenoeus	Transformed	Relative difference $\|\omega_H - \omega_T\|/\omega_T$
7.0817	6.6319	6.7835%
12.7052	12.9277	1.7211%
22.0785	21.2742	3.7806%

Table 3.2: Comparison between eigenfrequencies for homogeneuos and inhomogeneous plates with 'erroneous' linear transformation law (3.37).

The numerically computed eigenfrequencies in the homogeneous and inhomogeneous plates are reported in Table 3.2. The relative difference $|\omega_H - \omega_T|/\omega_T$ between the eigenfrequency of the homogeneous structure ω_H and the ones of the transformed one ω_T are also reported.

The comparative analysis shows the difference in eigenfrequencies. Such a difference must be attributed to the change of interface conditions between untransformed and transformed domain and to the change of boundary conditions.

We finally show in Figures 3.7, 3.8, 3.9 a comparison for different boundary conditions, where we apply the 'right' transformation law (3.33-3.34). In Table 3.3 we report the corresponding eigenfrequencies and the relative difference.

Homogenoeus ω_H (rad/s)	Transformed ω_T (rad/s)	Relative difference $\|\omega_H - \omega_T\|/\omega_T$
Clamped - Figure 4		
13.661	13.664	0.0219 %
19.664	19.680	0.0813 %
30.031	30.081	0.166 %
C-SS-F - Figure 5		
7.599	7.591	0.105 %
14.172	14.132	0.283 %
24.479	24.336	0.587 %
SS-F - Figure 6		
6.940	6.919	0.303 %
12.538	12.456	0.658 %
21.984	21.792	0.881 %

Table 3.3: Comparison between eigenfrequencies for homogenoeuos and inhomogeneous plates for different boundary conditions. SS=simply supported, C=clamped, F=free. Results correspond to the eigenmodes shown in Figures 3.6, 3.7 and 3.8.

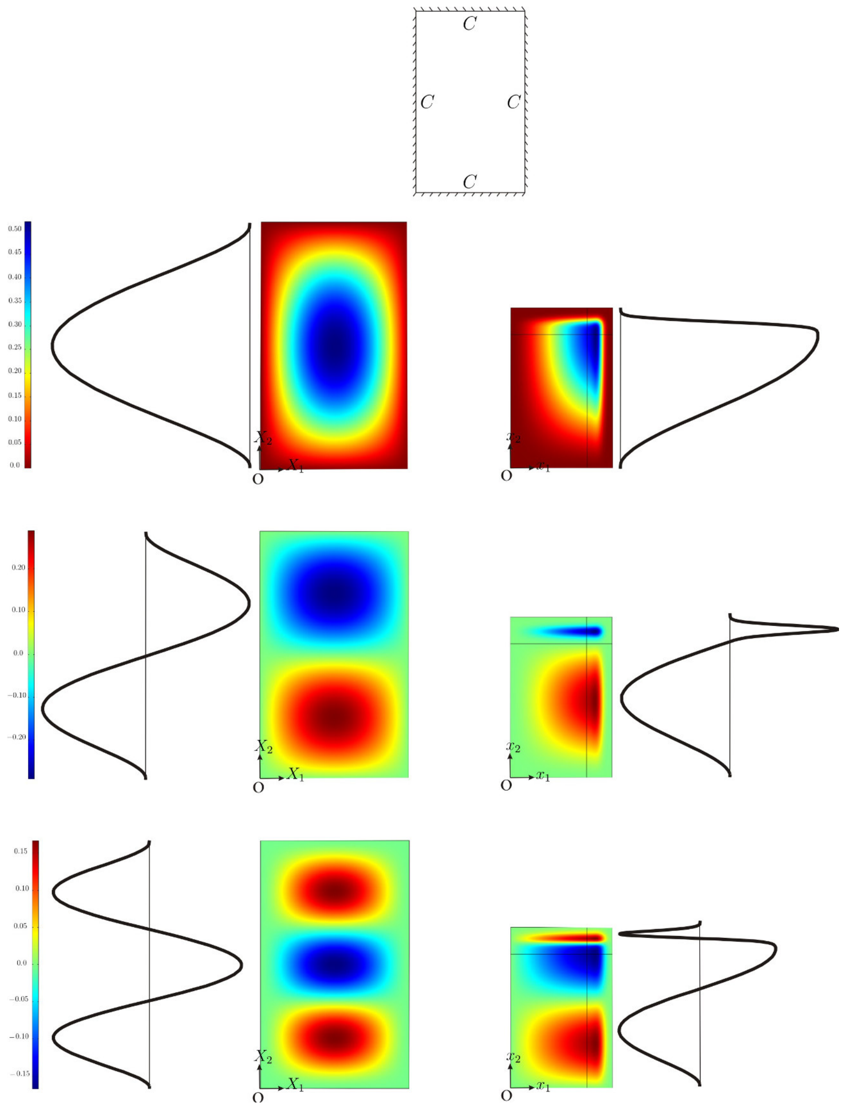

FIGURE 3.7: Eigenmodes of homogeneous (left column) and inhomogeneous (right column) rectangular plate. Contour plots of transverse displacement and displacement distribution along $X_1 = x_1 = A_3 = 6$ m are shown. Clamped (C) boundary conditions are considered.

The results confirm that, independently on the type of boundary conditions, the applied formalism is correct since eigenfrequencies remain unaltered up to numerical approximations and eigenmodes are simply shifted following $w(\mathbf{x}) = W(\mathbf{X})$.

3.5 Perfectly Matched Layers

To introduce numerical dissipation and implement the Perfectly Matched Layers, we define a complex transformation $\mathbf{g}(\mathbf{x}) = \mathbf{g}^R(\mathbf{x}) + i\mathbf{g}^I(\mathbf{x})$, where $\mathbf{g}^R$ and $\mathbf{g}^I$ stand for the real and imaginary parts. Consequently, the deformation gradient

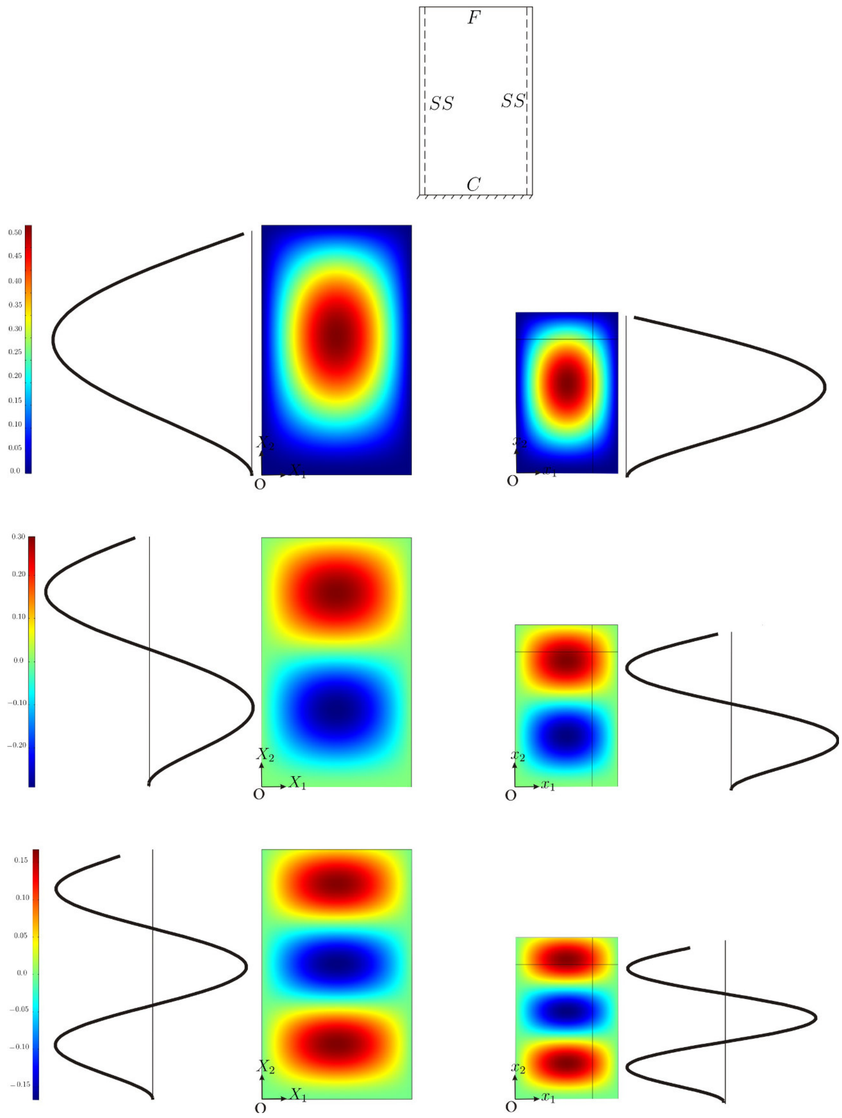

FIGURE 3.8: Eigenmodes of homogeneous (left column) and inhomogeneous (right column) rectangular plate. SS = simply supported, C = clamped, F = free. Contour plots of transverse displacement and displacement distribution along $X_1 = x_1 = A_3 = 6$ m are shown.

$\mathbf{f}(\mathbf{x}) = \nabla\mathbf{g}(\mathbf{x})$ can be split into the real and imaginary parts $\mathbf{f}^R$ and $\mathbf{f}^I$, respectively. Then, in addition to $\mathbf{g}^R(\mathbf{x}_0) = \mathbf{x}_0$, $\mathbf{g}^I(\mathbf{x}_0) = \mathbf{0}$, the sufficient conditions (3.31) at the interface point $\mathbf{x}_0$ are satisfied by

$$\begin{cases} \mathbf{f}^R(\mathbf{x}_0) = \mathbf{I}, \quad \mathbf{f}^I(\mathbf{x}_0) = \mathbf{0}, \\ \nabla\mathbf{f}^R(\mathbf{x}_0) = \nabla\mathbf{f}^I(\mathbf{x}_0) = \mathbf{0}, \\ \nabla\nabla\mathbf{f}^R(\mathbf{x}_0) = \nabla\nabla\mathbf{f}^I(\mathbf{x}_0) = \mathbf{0}. \end{cases} \tag{3.38}$$

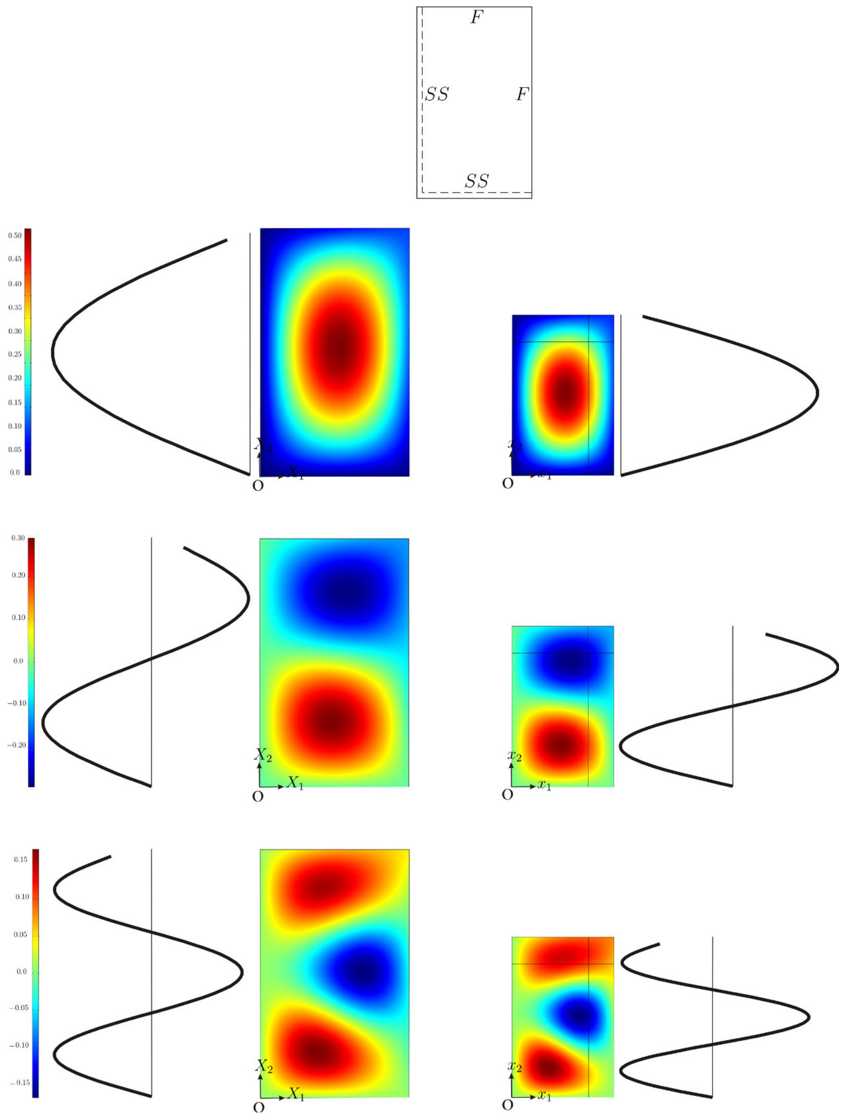

FIGURE 3.9: Eigenmodes of homogeneous (left column) and inhomogeneous (right column) rectangular plate. SS = simply supported, F = free. Contour plots of transverse displacement and displacement distribution along $X_1 = x_1 = A_3 = 6$ m are shown.

It is also possible to impose conditions (3.38) on a point $\mathbf{x}_1$ on the external boundary of the PML to identify the type of boundary conditions (simple support, clamped, free, etc.) after transformation. The additional condition $\mathbf{g}(\mathbf{x}_1) = \mathbf{X}_1$ introduces a stretching of the PML layer if $\mathbf{X}_1 \neq \mathbf{x}_1$.

For simplicity, we restrict our attention to a rectangular geometry as the transformed one in Figure 3.3, where the PMLs are the domains $\Omega^{(1)}, \cdots, \Omega^{(4)}, \Omega^{(6)}, \cdots, \Omega^{(9)}$, while $\Omega_0^{(5)} = \Omega^{(5)}$ is the central domain, which is of interest for a specific computation. We apply a transformation as in Eqs. (3.33) and (3.34), where

$$\begin{aligned} \bar{\eta}_+(x_i) &= \eta_+(x_i) + i(-1)^{\gamma+1}(x_i - A_{i+2})^\gamma, \\ \bar{\eta}_-(x_i) &= \eta_-(x_i) + i(x_i + A_{i+2})^\gamma, \qquad i = 1, 2. \end{aligned} \tag{3.39}$$

In Eq. (3.39), $\eta_\pm(x_i)$ is given in Eq. (3.32), while $\gamma \in \mathbb{N}$ and $\gamma > 3$ to satisfy conditions (3.38). Restricting again the attention to the domain $\Omega^{(6)}$, homogeneous conditions (3.38) for $\mathbf{f}^I$ at $\mathbf{x}_0 = (A_3\ x_2)^T$, $|x_2| \leq A_2$, impose $[\bar{\eta}_+^I(A_3)]' = [\bar{\eta}_+^I(A_3)]'' = [\bar{\eta}_+^I(A_3)]''' = 0$, for the imaginary part of the transformation. The additional condition $\mathbf{g}(\mathbf{x}_0) = \mathbf{x}_0$ gives $\bar{\eta}_+^I(A_3) = 0$. Then, a non-zero imaginary part of the transformation, resulting from the set of the just mentioned 4 homogeneous conditions, requires $\gamma > 3$. We also note that the sign of the imaginary part has been imposed to assure dissipation.

Even if the identification of the external boundary conditions is not necessary for the PMLs, we implemented conditions (3.39) in order to give a better physical interpretation of the PMLs and to facilitate the implementation in a FEM code. We also note that these additional conditions lead to a higher degree polynomial $\bar{\eta}_\pm$, without the introduction of particular difficulties in the implementation.

3.6 Numerical results

The PMLs have been implemented in *Comsol Multiphysics®* and details of the implementation are given below.

3.6.1 Implementation of PMLs equations.

The deformation gradient of the transformation in the different domains $\Omega^{(1)}, \ldots, \Omega^{(9)}$ in the transformed geometry in Figure 3.3 is

$$\mathbf{F} = \begin{bmatrix} F_{11} & 0 \\ 0 & F_{22} \end{bmatrix} = \begin{bmatrix} \frac{1}{f_{11}} & 0 \\ 0 & \frac{1}{f_{22}} \end{bmatrix}, \tag{3.40}$$

where

$$f_{11} = g_{1,1} = \begin{cases} f_{11}^- & \text{in } \Omega^{(1)},\ \Omega^{(4)},\ \Omega^{(7)}, \\ 1 & \text{in } \Omega^{(2)},\ \Omega^{(5)},\ \Omega^{(8)}, \\ f_{11}^+ & \text{in } \Omega^{(3)},\ \Omega^{(6)},\ \Omega^{(9)}, \end{cases} \tag{3.41}$$

and

$$f_{22} = g_{2,2} = \begin{cases} f_{22}^- & \text{in } \Omega^{(1)},\ \Omega^{(2)},\ \Omega^{(3)}, \\ 1 & \text{in } \Omega^{(4)},\ \Omega^{(5)},\ \Omega^{(6)}, \\ f_{22}^+ & \text{in } \Omega^{(7)},\ \Omega^{(8)},\ \Omega^{(9)}. \end{cases} \tag{3.42}$$

Partial derivatives are intended with respect to x_i $(i = 1, 2)$.

In addition,

$$J = F_{11}F_{22} = \frac{1}{f_{11}f_{22}}. \tag{3.43}$$

The expressions in Eqs. (3.41) and (3.42) are

$$\begin{aligned} f_{I\imath}^+ &= 1 + (1-\zeta)\eta_+'(\tilde{x}_\imath) + i(-1)^{\gamma+1}\gamma(x_\imath - A_{\imath+2})^{\gamma-1}, \\ f_{I\imath}^- &= 1 + (1-\zeta)\eta_-'(\tilde{x}_\imath) + i\gamma(x_\imath + A_{\imath+2})^{\gamma-1}, \end{aligned} \tag{3.44}$$

where $I = \imath = 1, 2$ ($\imath$ not summed), while $\tilde{x}_\imath$ and ζ are defined in Eq. (3.32). Assuming $\eta_\pm(\tilde{x}_\imath)$ as in Eq. (3.32)

$$\eta_\pm'(\tilde{x}_\imath) = \mp 140\tilde{x}_\imath^3 + 420\tilde{x}_\imath^4 \mp 420\tilde{x}_\imath^5 + 140\tilde{x}_\imath^6. \tag{3.45}$$

From the deformation gradient it is possible to compute the components of the inhomogeneous anisotropic constitutive tensor. The non zero components are:

$$\begin{aligned} &\mathbb{D}_{1111} = B\, F_{11}^3/F_{22}, \quad \mathbb{D}_{1122} = \mathbb{D}_{2211} = B\nu F_{11}F_{22}, \\ &\mathbb{D}_{2222} = B\, F_{22}^3/F_{11}, \quad \mathbb{D}_{1212} = \mathbb{D}_{2121} = \mathbb{D}_{1221} = \mathbb{D}_{2112} = B\tfrac{1-\nu}{2}F_{11}F_{22}. \end{aligned} \tag{3.46}$$

From the constitutive tensor $\mathbb{D}$ the moment tensor $\mathbf{m}$ can be obtained as in Eq. (3.16). In particular,

$$\begin{cases} m_{11} = -B\dfrac{F_{11}}{F_{22}}\left(F_{11}^2 w_{,11} + \nu F_{22}^2 w_{,22}\right), \\ m_{12} = m_{21} = -B(1-\nu)F_{11}F_{22}\, w_{,12}, \\ m_{22} = -B\dfrac{F_{22}}{F_{11}}\left(\nu F_{11}^2 w_{,11} + F_{22}^2 w_{,22}\right). \end{cases} \tag{3.47}$$

Concerning $\nabla \mathbf{F}$, the only non zero components of the first gradient of $\mathbf{F}$ are

$$F_{11,1} = -\frac{f_{11,1}}{f_{11}^2}, \qquad F_{22,2} = -\frac{f_{22,2}}{f_{22}^2}, \tag{3.48}$$

where, similar to Eqs. (3.41) and (3.42)

$$f_{11,1} = g_{1,11} = \begin{cases} f_{11,1}^- & \text{in } \Omega^{(1)},\ \Omega^{(4)},\ \Omega^{(7)}, \\ 0 & \text{in } \Omega^{(2)},\ \Omega^{(5)},\ \Omega^{(8)}, \\ f_{11,1}^+ & \text{in } \Omega^{(3)},\ \Omega^{(6)},\ \Omega^{(9)}, \end{cases} \tag{3.49}$$

and

$$f_{22,2} = g_{2,22} = \begin{cases} f_{22,2}^- & \text{in } \Omega^{(1)},\ \Omega^{(2)},\ \Omega^{(3)}, \\ 0 & \text{in } \Omega^{(4)},\ \Omega^{(5)},\ \Omega^{(6)}, \\ f_{22,2}^+ & \text{in } \Omega^{(7)},\ \Omega^{(8)},\ \Omega^{(9)}. \end{cases} \tag{3.50}$$

In particular,

$$\begin{aligned} f_{I\imath,\imath}^+ &= (1-\zeta)\eta_+''(\tilde{x}_\imath) + i(-1)^{\gamma+1}\gamma(\gamma-1)(x_\imath - A_{\imath+2})^{\gamma-2}, \\ f_{I\imath,\imath}^- &= (1-\zeta)\eta_-''(\tilde{x}_\imath) + i\gamma(\gamma-1)(x_\imath + A_{\imath+2})^{\gamma-2}, \end{aligned} \tag{3.51}$$

where $I = \imath = 1, 2$ ($\imath$ not summed), and

$$\eta_\pm''(\tilde{x}_\imath) = \mp 420\tilde{x}_\imath^2 + 1680\tilde{x}_\imath^3 \mp 2100\tilde{x}_\imath^4 + 840\tilde{x}_\imath^5. \tag{3.52}$$

Concerning $\nabla\nabla \mathbf{F}$, the only non zero components of the second gradient of $\mathbf{F}$ are

$$F_{11,11} = 2\frac{f_{11,1}^2}{f_{11}^3} - \frac{f_{11,11}}{f_{11}^2}, \qquad F_{22,2} = 2\frac{f_{22,2}^2}{f_{22}^3} - \frac{f_{22,22}}{f_{22}^2}, \tag{3.53}$$

where

$$f_{11,11} = g_{1,111} = \begin{cases} f_{11,11}^- & \text{in } \Omega^{(1)},\ \Omega^{(4)},\ \Omega^{(7)}, \\ 0 & \text{in } \Omega^{(2)},\ \Omega^{(5)},\ \Omega^{(8)}, \\ f_{11,11}^+ & \text{in } \Omega^{(3)},\ \Omega^{(6)},\ \Omega^{(9)}, \end{cases} \tag{3.54}$$

and

$$f_{22,22} = g_{2,222} = \begin{cases} f_{22,22}^- & \text{in } \Omega^{(1)},\ \Omega^{(2)},\ \Omega^{(3)}, \\ 0 & \text{in } \Omega^{(4)},\ \Omega^{(5)},\ \Omega^{(6)}, \\ f_{22,22}^+ & \text{in } \Omega^{(7)},\ \Omega^{(8)},\ \Omega^{(9)}. \end{cases} \tag{3.55}$$

In particular,

$$
\begin{aligned}
f^{+}_{I\imath,\imath\imath} &= (1-\zeta)\eta'''_{+}(\tilde{x}_\imath) + i(-1)^{\gamma+1}\gamma(\gamma-1)(\gamma-2)(x_\imath - A_{\imath+2})^{\gamma-3}, \\
f^{-}_{I\imath,\imath\imath} &= (1-\zeta)\eta'''_{-}(\tilde{x}_\imath) + i\gamma(\gamma-1)(\gamma-2)(x_\imath + A_{\imath+2})^{\gamma-3},
\end{aligned}
\tag{3.56}
$$

where $I = \imath = 1, 2$ ($\imath$ not summed), $\gamma \geq 3$ and

$$
\eta'''_{\pm}(\tilde{x}_\imath) = \mp 840\tilde{x}_\imath + 5040\tilde{x}_\imath^2 \mp 8400\tilde{x}_\imath^3 + 4200\tilde{x}_\imath^4. \tag{3.57}
$$

The components of the axial force tensor (3.19) are

$$
\begin{cases}
p_{11} = -B\dfrac{F_{11}}{F_{22}}\left(F_{11,1}^2 + F_{11}F_{11,11} - \nu F_{22}F_{22,22}\right), \\
p_{12} = p_{21} = -B\nu\, F_{11,1}F_{22,2} \\
p_{22} = -B\dfrac{F_{22}}{F_{11}}\left(F_{22,2}^2 + F_{22}F_{22,22} - \nu F_{11}F_{11,11}\right).
\end{cases}
\tag{3.58}
$$

For the implementation in a FEM code it is convenient to define the components of $\mathbf{f}$ and of its first and second gradient and, in a second step, the components of $\mathbf{F}$ and of its first and second gradient as in Eqs. (3.40)c, (3.48) and (3.53), respectively.

Then, it is possible to implement the constitutive tensor as in Eq. (3.46), or directly the moment as in Eq. (3.47), and the axial force as in Eq. (3.58).

3.6.2 PMLs performances

The numerical results concerning a finite region with PMLs are compared with an analytical solution. In particular, we consider the time-harmonic infinite body Green's function

$$
w_g(\mathbf{x}, \mathbf{x}_0; \omega) = \frac{i}{8B\beta^2}[H_0^{(1)}(\beta r) - H_0^{(1)}(i\beta r)], \tag{3.59}
$$

where $r = |\mathbf{x} - \mathbf{x}_0|$ and $H_0^{(1)}$ is the Hankel function of the first type or order zero.

The geometry is square with $A = A_1 = A_2 = 10$ m, $a = a_1 = a_2 = 6$ m, $A_3 = A_4 = 5$ m and the mechanical properties of the plates are as in Section 3.4.

In order to give a quantitative measure of the performance of the PMLs, we define the *quality factor*

$$\mathcal{Q} = \frac{\int_{\Omega_5} \left[w_{Num}(\mathbf{x}) - w_{Ex}(\mathbf{x})\right]^2 d\Omega}{\int_{\Omega_5} [w_{Ex}(\mathbf{x})]^2 d\Omega}, \tag{3.60}$$

where w_{Ex} is the exact infinite body analytical solution (the real part of the Green's function w_g) and w_{Num} the numerical FEM solution. The integrals on the untransformed domain Ω_5 were done numerically in *Comsol Multiphysics®* [2]

3.6.3 Discretization

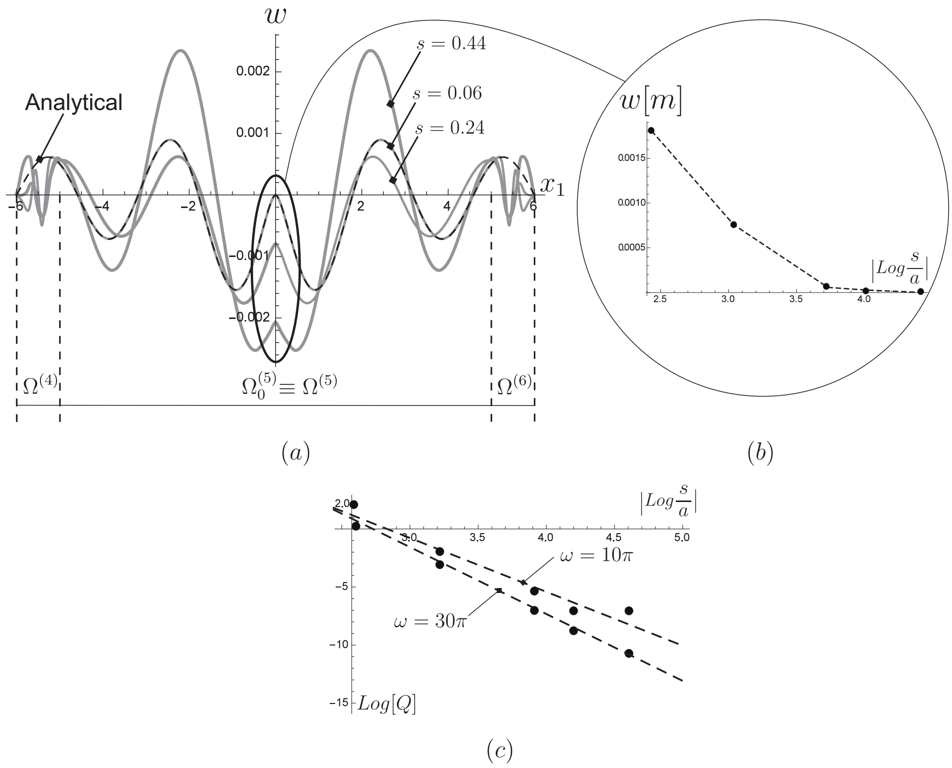

FIGURE 3.10: Comparison between numerical results and the exact solution corresponding to the Green's function (3.59) with $\mathbf{x}_0 = 0$. (a) Displacement along the line $x_2 = 0$ at $\omega = 30\pi$ rad/s. Numerical solutions are given in gray lines for different discretizations; s [m] is the maximum size of the three-nodes triangular elements. The exact solution is given in black dashed line. (b) Displacement in $\mathbf{x} = 0$ as a function of the relative size of the elements s/a (in logarithmic scale). (c) Quality factor $\mathcal{Q}$ as a function of the relative size of the elements. Results are given in logarithmic scales.

In Figure 3.10 we show the comparison between the analytical solution and the numerical ones for different maximum sizes s of the elements of the discretized geometry. From the displacement distribution along the lines $x_2 = 0$, shown in

[2] The precision of the numerical integration was checked by comparing, at different frequencies, the results of the integral at the denominator in Eq. (3.60) with the exact values.

Figure 3.10a, and the displacement w at the center of the domain ($\mathbf{x} = \mathbf{0}$), shown in 3.10b as a function of the relative size of the elements, it is evident that the numerical solution converges to the exact one as the size of the elements decreases. The PML regions Ω_4 and Ω_6 and the damping effect are also visible.

The study of the *quality factor* $\mathcal{Q}$ as a function of the relative size of the elements in Figure 3.10c shows that the numerical solution converges to the exact one approximately as $\mathcal{Q} \sim (s/a)^z$, where $z = -4.63$ for $\omega = 10\pi$ rad/s and $z = -5.76$ for $\omega = 30\pi$ rad/s, respectively.

3.6.4 Frequency dependance

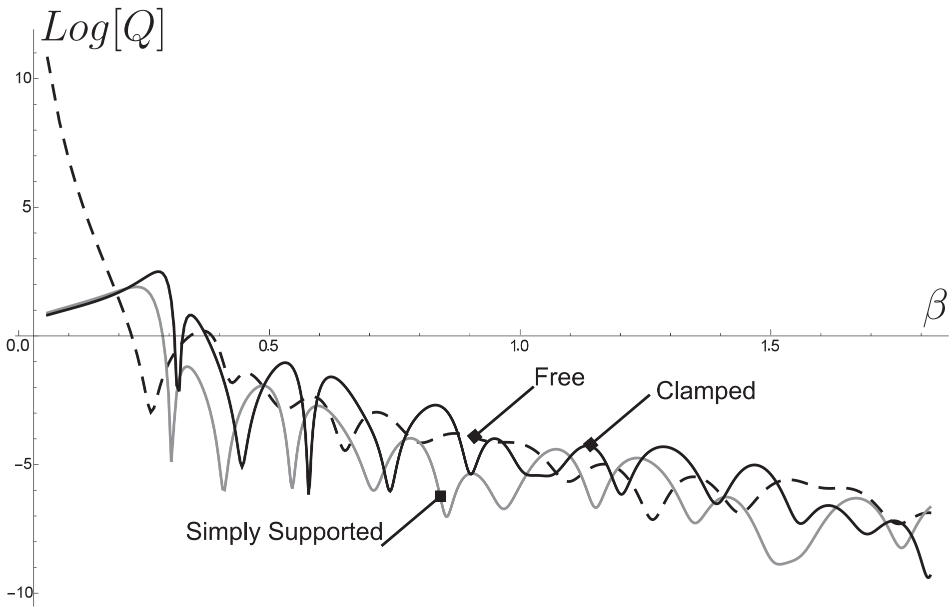

FIGURE 3.11: *Quality factor* $\mathcal{Q}$, in logarithmic scale, as a function of the frequency parameter β. Results are given for different boundary conditions on the external boundary: simple support (gray line), clamped (continuous black line) and free (dashed black line).

The *quality factor* as a function of the frequency parameter β is shown in Figure 3.11. Classical boundary conditions have been implemented on the external boundary of our domain, which, in view of the applied transformation, correspond to the same boundary conditions before transformation, when the plate is homogeneous. Consistently with the results obtained for flexural waves in beams [77], it is shown that the *quality factor* has a tendency to decrease non monotonically at increasing frequency.

The comparative analysis shows that the simple support boundary condition is the preferable choice.

At low frequencies PMLs loose their performance. These can be attributed to the fact that reflection resulting from the introduction of the boundary conditions at $x_{1,2} = \pm a$ prevails on the damping effect of the external layers. In the next figure we prove that this problem can be easily overcome increasing the thickness of the PMLs.

3.6.5 Geometrical parameters of the PMLs

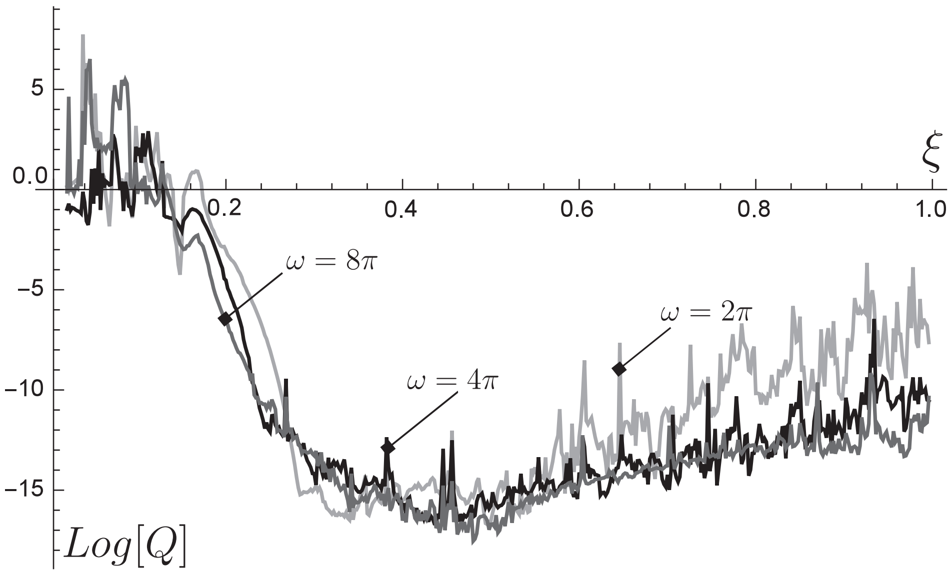

FIGURE 3.12: *Quality factor* $\mathcal{Q}$, in logarithmic scale, as a function of the relative dimension of the layer $\xi = (a - A_3)/A_3$. Results are given for three different radian frequencies. The plate is simply supported.

The *quality factor* as a function of the relative dimension $\xi = (a - A_3)/A_3$ of the PMLs is shown in Figure 3.12. Different frequencies and simple support boundary conditions are considered. For the example under consideration, a minimum thickness $\xi \simeq 0.2$ is needed to reduce the *quality factor* to values for which reflection becomes negligible. It appears that an optimal relative thickness minimizing $\mathcal{Q}$ is $\xi \simeq 0.5$, at this value the dependance of the $\mathcal{Q}$ on the frequency is weak.

In Figure 3.13 the effect of the transformation ratio ζ on the *quality factor* is shown for the same frequencies and boundary conditions of Figure 3.12. The results show oscillations of $\mathcal{Q}$ with respect to ζ, so that it is possible to tune ζ in order to have the optimal filtering at a certain frequency ω. On average we do not

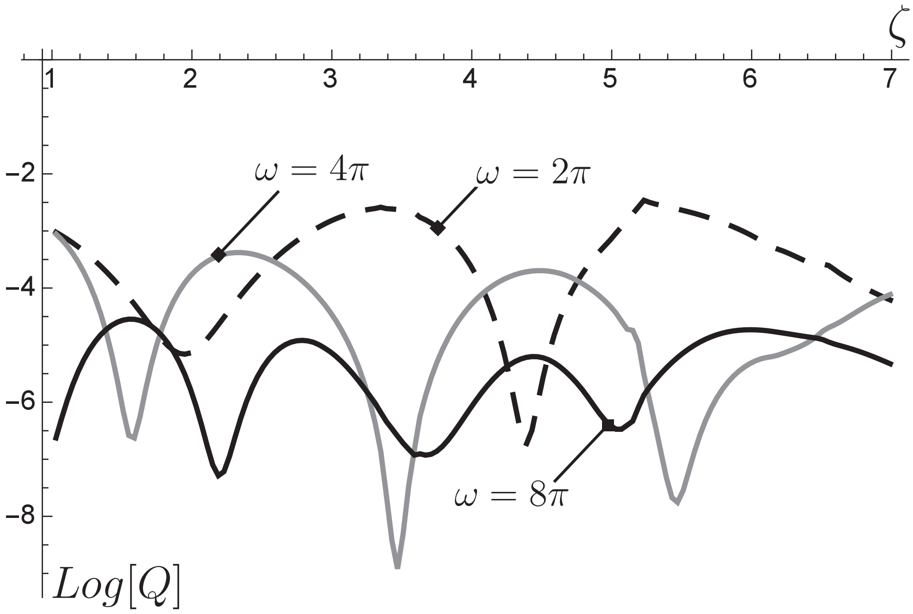

FIGURE 3.13: *Quality factor* $\mathcal{Q}$, in logarithmic scale, as a function of transformation ratio ζ (see eq. (3.32)). Results are given for three different radian frequencies. The plate is simply supported.

note a particular improvement of the results with respect to the amplitude of ζ and, therefore, also the simpler case $\zeta = 1$, for which there is only the introduction of dissipation, is competitive.

Results, not reported here for brevity, show that changing the load source position to $\mathbf{x}_0 = (3.5\text{m}, 1.5\text{m})$ change the amplitude of oscillations, but not the position of the maxima and minima, while changing the dimension a and A_3 varies the position and the numbers of stationary points in the curves. This may suggest a possible correlation with natural frequencies of the untransformed domain; an issue that is left for a future analysis.

3.6.6 Dissipation

The effect of the exponent γ of the imaginary part of the transformation (3.39) is detailed in the contour plots in Figure 3.14. The results, confirmed by the values of the *quality factor* , show that for integer values $\gamma \geq 3$ reflection is strongly reduced. *Quality factor* reduces at increasing γ, and odd values give better results.

We note that the results of Figure 3.14 for $\gamma = 3$ evidence that less restrictive conditions could be applied on the transformation (3.39). In order to inspect this issue we consider an incident wave impinging on a vertical interface at $x_1 = \bar{x}_1$

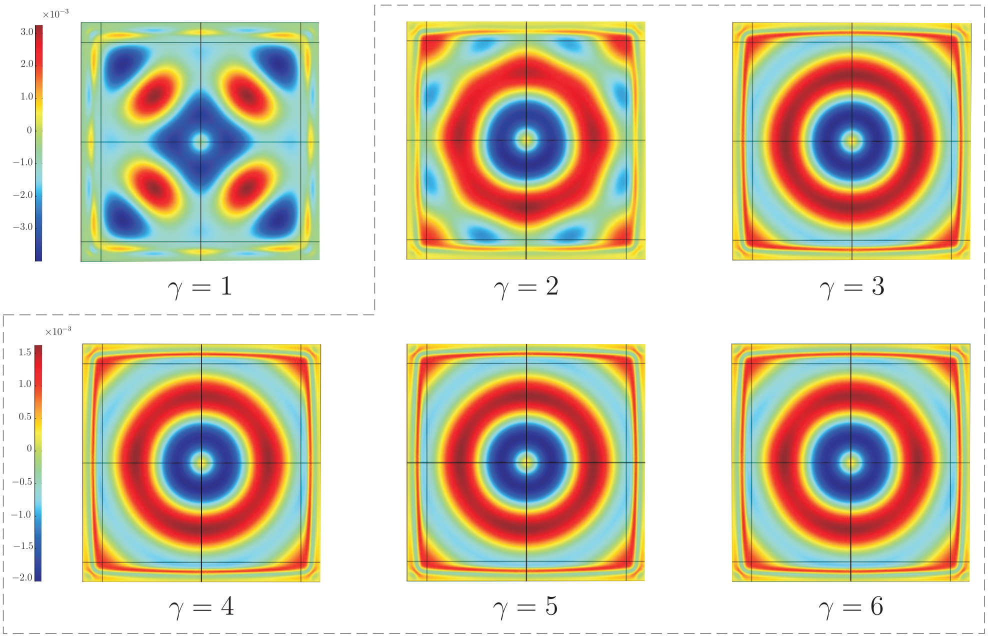

FIGURE 3.14: Contour plots of transverse displacements w for different values of the exponent γ in transformation (3.39). Results are given for simply supported plate and $\omega = 16\pi$.

and generating reflected and transmitted waves. For $x_1 < \bar{x}_1$ the material is homogeneous and isotropic and for $x_1 > \bar{x}_1$ the material is obtained introducing a transformation $\mathbf{g}(\mathbf{x}) = (\bar{\eta}(x_1), 0)$. The incident wave has the form $w^I(\mathbf{x}) = e^{ik_2x_2}(I_1 e^{ik_1x_1} + I_2 e^{-k_1x_1})$ involving both propagating and evanescent parts, with I_1 and I_2 assigned values; the reflected wave has the form $w^R(\mathbf{x}) = e^{ik_2x_2}(Q_1 e^{-ik_1x_1} + Q_2 e^{k_1x_1})$ and the transmitted one is $w^T(\mathbf{x}) = e^{ik_2x_2}(T_1 e^{ik_1\bar{\eta}(x_1)} + T_2 e^{-k_1\bar{\eta}(x_1)})$. By applying the interface conditions

$$\begin{cases} w^I(\bar{x}_1, x_2) + w^R(\bar{x}_1, x_2) = w^T(\bar{x}_1, x_2), \\ w^I_{,1}(\bar{x}_1, x_2) + w^R_{,1}(\bar{x}_1, x_2) = w^T_{,1}(\bar{x}_1, x_2), \\ m^I_{11}(\bar{x}_1, x_2) + m^R_{11}(\bar{x}_1, x_2) = m^T_{11}(\bar{x}_1, x_2), \\ r^I_1(\bar{x}_1, x_2) + r^R_1(\bar{x}_1, x_2) = r^T_1(\bar{x}_1, x_2), \end{cases} \tag{3.61}$$

it results that reflected waves vanish, i.e. $Q_1 = Q_2 = 0$, if

$$\bar{\eta}(\bar{x}_1) = \bar{x}_1, \quad \bar{\eta}'(\bar{x}_1) = 1, \quad \bar{\eta}''(\bar{x}_1) = 0. \tag{3.62}$$

The conditions (3.62) indicate that the constraints on the second gradient of the transformation $\mathbf{f}$, given in Eq. (3.31), are not necessary to cancel reflection. In such a case, restricting the attention to polynomial transformations, it is possible to reduce the degree of the polynomial, since three conditions instead of four must be satisfied.

As an additional comment, we note that in the last condition in Eqs. (3.61), the terms involving shear and axial forces, cancel out the contribution of $\bar{\eta}'''(\bar{x}_1)$.

3.6.7 Load position

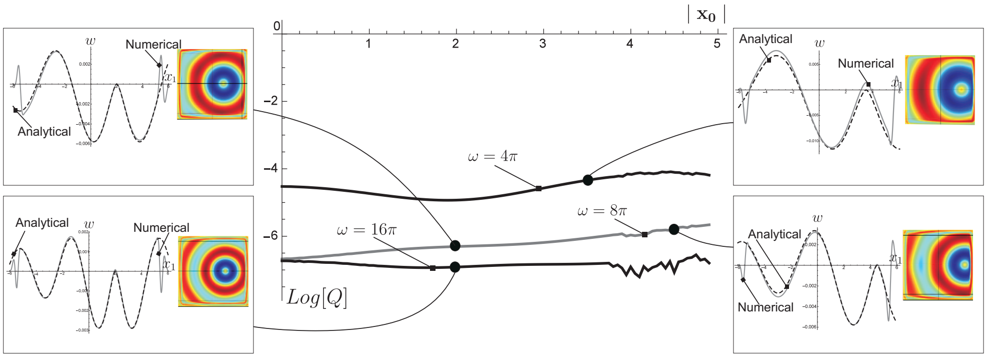

FIGURE 3.15: *Quality factor* $\mathcal{Q}$ in logarithmic scale as a function of the point source position $\mathbf{x}_0 = (x_{01}, 0)$. Results are given for three different radian frequencies. The plate is simply supported. In the four insets the numerical solution (gray lines) is compared with the analytical solution (dashed lines) and the contour plots of the transverse displacement w are given.

Since PMLs can be used for different purposes and often scatterers are placed close to the external boundary of the numerical domain, we investigate the *quality factor* by changing the position of the applied load moving from the center to the proximity of the PML domains. Such analysis cannot be considered as an analysis of far field and near field perfomances since the Green's function (3.59) involves only the monopole term of the Hankel functions. Nevertheless, the Green's function includes both propagating and evanescent effects and the results shown in Figure 3.15 give an indication of the correctness and applicability of the proposed model. In Figure 3.15 it is shown that, when the concentrated load approaches the PML domain, the performances of the PMLs in term of *quality factor* remain practically unaltered. Even when the force is applied at a distance of 0.05 m from the PML boundary, the numerical results are in excellent agreement with the analytical solution.

Chapter 4

Platonic crystal with low-frequency locally resonant snail structures

Here we propose a new type of platonic crystal. The proposed microstructured plate includes snail resonators with low-frequency resonant vibrations. Lowest resonance frequencies are predicted analytically and numerically. We indicate the possibility to attain localization, wave trapping and edge waves. Applications of transmission amplification and suppression of the low-frequency flexural vibrations are illustrated.

4.1 The platonic system of snail resonators

We consider flexural vibrations in Kirchhoff-Love plates. In the time-harmonic regime, the transverse displacement $W(\mathbf{x})$ satisfies the fourth-order biharmonic equation (3.5).

We consider a steel plate, with $\varrho = 7800$ kg/m^3, $E = 2 \times 10^5$ MPa, $\nu = 0.3$ and $h = 1$ mm. The shear modulus is $\mu = E/(2(1+\nu)) = 7.6923 \times 10^4$ MPa, and $B = 1.831 \times 10^{-1}$ Nm, is the flexural stiffness. Rotation is the gradient vector $\phi(\mathbf{x}) = \nabla W(\mathbf{x})$, while the static quantities are the bending moment symmetric tensor $\mathbf{M}$ and the shear force vector $\mathbf{V} = \nabla \cdot \mathbf{M}$.

4.1.1 Geometry of the periodic cell

The unit cell of the square periodic system is shown in Figure 4.1. In the square unit cell of side length $a = 1$ m, a central hole of radius $R_1 = 0.35$ m is introduced with a circular inclusion of radius $R_0 = 0.175$ m. The inclusion is connected to the external structure by a slender spiral of thickness $s = 21.875$ mm.

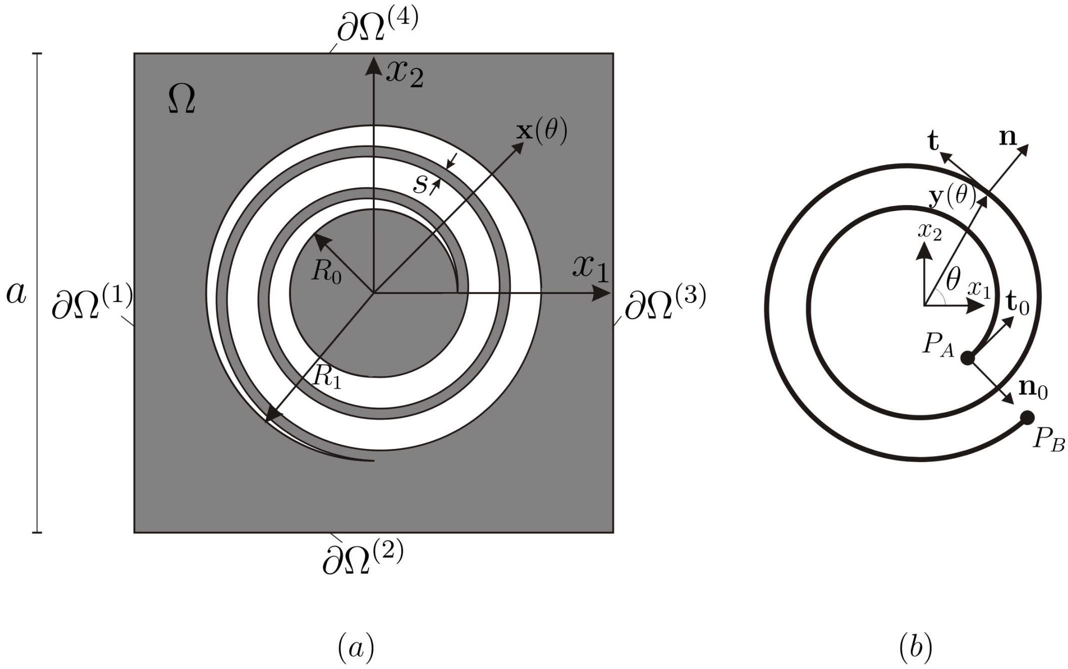

FIGURE 4.1: (a) Geometry of the unit cell of the platonic crystal. (b) Geometry of the central axis of the spiral connection. Normal and tangential directions $\mathbf{n}(\theta)$ and $\mathbf{t}(\theta)$ are indicated, $\mathbf{n}_0 = \mathbf{n}(-\pi/4)$ and $\mathbf{t}_0 = \mathbf{t}(-\pi/4)$.

The radial position of the central axis of the spiral is indicated in Figure 4.1b and given by:

$$y(\theta) = |\mathbf{y}(\theta)| = R_0 + (R_1 - R_0)\frac{\theta + \pi/4}{4\pi}, \quad \theta \in \left[-\frac{\pi}{4}, 4\pi - \frac{\pi}{4}\right]. \tag{4.1}$$

The curve can be given in the parametric form

$$C(\theta) := \mathbf{y}(\theta) = [y_1(\theta), y_2(\theta)] = [y(\theta)\cos(\theta), y(\theta)\sin(\theta)], \tag{4.2}$$

and the normal and tangent vector to the curve are:

$$\mathbf{n}(\theta) = \frac{1}{|C'(\theta)|}\begin{bmatrix} y_2'(\theta) \\ -y_1'(\theta) \end{bmatrix}, \qquad \mathbf{t}(\theta) = \frac{1}{|C'(\theta)|}\begin{bmatrix} y_1'(\theta) \\ y_2'(\theta) \end{bmatrix}, \tag{4.3}$$

with

$$|C'(\theta)| = \sqrt{y'(\theta)^2 + y(\theta)^2} = \sqrt{\left(\frac{R_1 - R_0}{4\pi}\right)^2 + \left[R_0 + (R_1 - R_0)\frac{\theta + \pi/4}{4\pi}\right]^2}. \tag{4.4}$$

The spiral length is

$$\begin{aligned} L = \int_0^{4\pi} \sqrt{y'(\theta - \pi/4)^2 + y(\theta - \pi/4)^2}\, d\theta = \\ \frac{R_1\sqrt{(R_1 - R_0)^2 + (4\pi R_1)^2} - R_0\sqrt{(R_1 - R_0)^2 + (4\pi R_0)^2}}{2(R_1 - R_0)} + \\ \frac{R_1 - R_0}{8\pi} \log\left[\frac{4\pi R_1 + \sqrt{(R_1 - R_0)^2 + (4\pi R_1)^2}}{4\pi R_0 + \sqrt{(R_1 - R_0)^2 + (4\pi R_0)^2}}\right], \end{aligned} \tag{4.5}$$

which takes the value $L = 3.303$ m.

4.2 Dispersion diagram of the model

The band structure of the flexural system is presented in Figure 4.2. The dispersion diagram has been computed performing an eigenfrequency analysis with the Finite Element package *Comsol Multiphysics*® (version 5.2) applying the following Floquet-Bloch conditions on the boundary (shown in Figure 4.1a):

$$\begin{aligned} W|_{\partial\Omega^{(3)}} = e^{ik_1 a} W|_{\partial\Omega^{(1)}},\ \phi_1|_{\partial\Omega^{(3)}} = e^{ik_1 a}\phi_1|_{\partial\Omega^{(1)}}, \\ M_{11}|_{\partial\Omega^{(3)}} = e^{ik_1 a} M_{11}|_{\partial\Omega^{(1)}},\ V_1|_{\partial\Omega^{(3)}} = e^{ik_1 a} V_1|_{\partial\Omega^{(1)}}, \\ W|_{\partial\Omega^{(4)}} = e^{ik_2 a} W|_{\partial\Omega^{(2)}},\ \phi_2|_{\partial\Omega^{(4)}} = e^{ik_2 a}\phi_2|_{\partial\Omega^{(2)}}, \\ M_{22}|_{\partial\Omega^{(4)}} = e^{ik_2 a} M_{22}|_{\partial\Omega^{(2)}},\ V_2|_{\partial\Omega^{(4)}} = e^{ik_2 a} V_2|_{\partial\Omega^{(2)}}, \end{aligned} \tag{4.6}$$

where $\mathbf{k} = (k_1, k_2)^T$ is the wave vector.

The dispersion diagram is given following the path on the boundary of the irreducible Brillouin zone, sketched in Figure 4.2b.

A comparison with the dispersion diagram of a periodic perforated plate with only the internal holes of radius $R_1 = 0.35$ m is given in Figure 4.3a, while a comparison of dispersion diagrams of a perforated and homogeneous plate is given in part (b) of the same Figure. The band structure of perforated plates with free

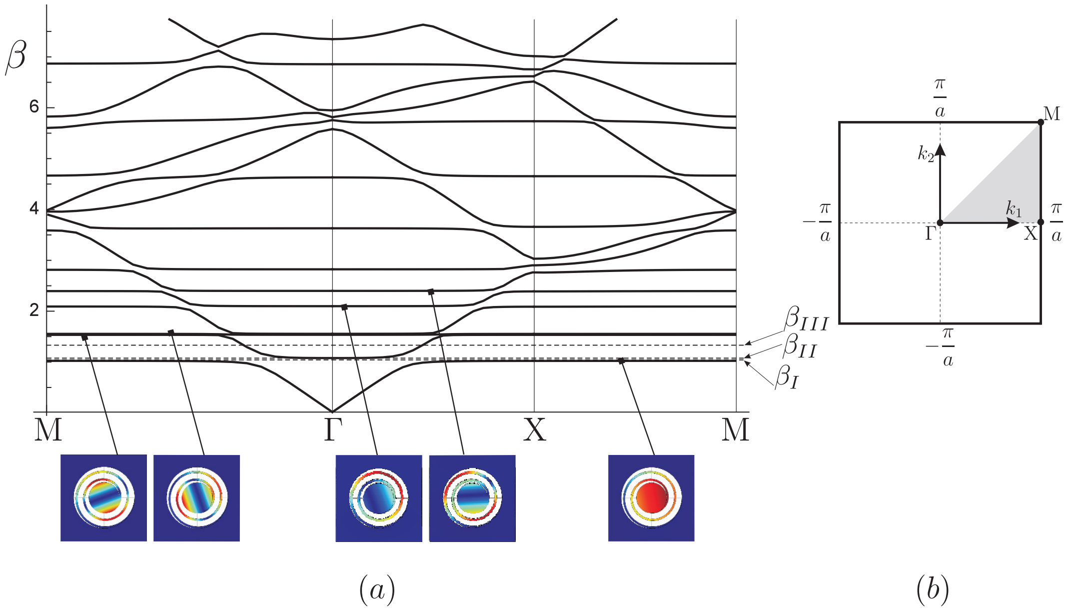

FIGURE 4.2: Dispersion diagram of the platonic crystal with snail resonators. The frequency parameter β is given as a function of the wave vector $\mathbf{k}$ along the boundary of the irreducible Brillouin zone. First five localized modes are illustrated in the bottom part. Colors from blue to red correspond to increasing amplitude of transverse displacement. (b) Sketch of the Brillouin zone in $\mathbf{k}$ space, with the irreducible Brillouin zone shaded. The symmetry points Γ, X and M are shown, corresponding to $\mathbf{k} = (0, 0)$, $\mathbf{k} = (\pi/a, 0)$ and $\mathbf{k} = (\pi/a, \pi/a)$, respectively.

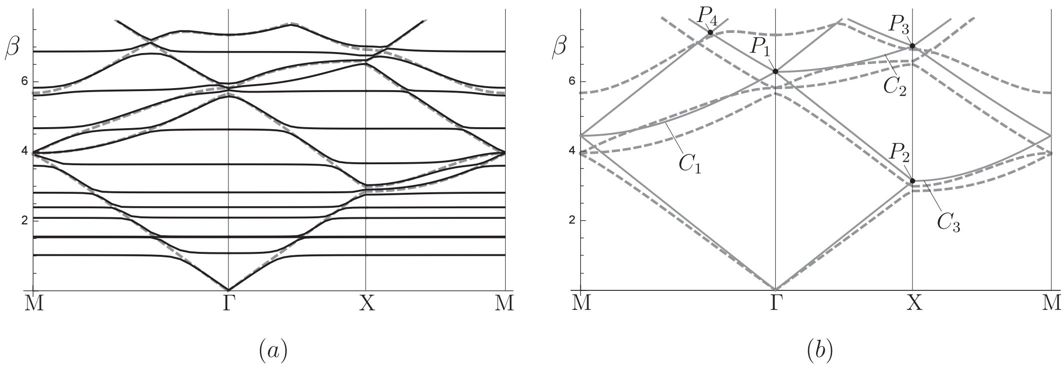

FIGURE 4.3: Comparison of dispersion diagrams. (a) Periodic system with snail resonators as in Figure 4.1 (black continuous lines) vs periodically perforated plate (grey dashed lines). (b) Periodically perforated plate (grey dashed lines) vs homogeneous plate (continuous grey lines).

and clamped boundary conditions have been extensively studied by applying the multipole expansion method in [72, 78, 79, 95, 107].

The comparative analysis in Figure 4.3b shows that the introduction of circular perforation induces a softening in the dynamic behavior of the plate, as expected on physical ground. Additionally, it is evident that dispersion curves split up (see, for examples curves C_1, C_2 and C_3), which leads to the formation of partial band gaps associated with wave propagation along specific directions. Moreover, the band gap opening at intersection points P_1 at Γ and P_2 and P_3 at X is noted, while intersection points P_3 and P_4 change their position (and the frequency) in the Brillouin space.

The presence of internal resonators (Figures 4.2 and 4.3a) gives rise to several localized modes associated with nearly horizontal dispersion curves, whereas the dispersion curves of the corresponding perforated plate remain practically unperturbed. First, we note that the lower localized modes appear at extremely low frequencies in correspondence with the acoustic modes of the perforated plate. Second we stress the possibility to have a large number of such flat curves within, a large frequency interval. This model generalizes the effect on a single frequency previously shown in [12]. It can be also considered as an alternative to the challenging problem of opening large stop bands at low frequencies for vibration isolation in acoustics and elasticity [6, 24, 29, 42].

4.3 Asympotic estimates for resonance frequencies of a single resonator

The frequencies of the first internal resonance modes are estimated analytically. We assess a class of standing waves in a periodic system containing inclusions with the structured spiral coating. We assume that the inclusion at the center is taken as rigid and the connecting spiral is an elastic massless beam. The vibration modes of this simplified mechanical model are obtained via the introduction of the transverse displacement W_m and rotations ϕ_n and ϕ_t of the rigid inclusions. The rotations ϕ_n and ϕ_t are taken around two orthogonal directions, respectively parallel to the normal $\mathbf{n}_0$ and tangent $\mathbf{t}_0$ at the intersection point P_A between the inclusion and the spiral connection (see Figure 4.1b). In the asymptotic approximation of the first three eigenfrequencies, it is feasible to assume the circular contour at $y = R_1$ as rigid, so that the spiral is clamped at P_B.

The kinetic energy of this mechanical system is

$$\mathcal{K}(t) = \frac{1}{2}\rho\pi\, hR_0^2\, \dot{W}_m^2 + \frac{1}{2}\rho\pi \frac{hR_0^4}{4}\left(\dot{\phi}_n^2 + \dot{\phi}_t^2\right), \tag{4.7}$$

while the potential energy of the assumed massless elastic spiral is

$$\mathcal{P}(t) = \frac{1}{2}\kappa_1 W_m^2 + \frac{1}{2}\kappa_2 \phi_n^2 + \frac{1}{2}\kappa_3 \phi_t^2, \tag{4.8}$$

where κ_1, κ_2 and κ_3 are the elastic stiffnesses guaranteed by the spiral to be determined in the following.

The Euler-Lagrange equations, imposing the balance of linear and angular momentum, have the forms

$$\begin{aligned} \rho\pi\, hR_0^2 \ddot{W}_m + \kappa_1 W_m &= 0, \\ \rho\pi \frac{hR_0^4}{4}\ddot{\phi}_n + \kappa_2 \phi_n &= 0, \\ \rho\pi \frac{hR_0^4}{4}\ddot{\phi}_t + \kappa_3 \phi_t &= 0, \end{aligned} \tag{4.9}$$

which in the time-harmonic regime yield the three resonance radian frequencies

$$\begin{aligned} \omega_1 &= \sqrt{\frac{\kappa_1}{\rho\pi\, hR_0^2}}, \\ \omega_2 &= 2\sqrt{\frac{\kappa_2}{\rho\pi\, hR_0^4}}, \\ \omega_3 &= 2\sqrt{\frac{\kappa_3}{\rho\pi\, hR_0^4}}. \end{aligned} \tag{4.10}$$

For the determination of the stiffnesses κ_i $(i = 1, 2, 3)$, we make use of the Virtual Work Principle by considering the effect of flexural, torsional and shear deformation of the spiral considered as a curved beam clamped at P_B (see Figure 4.1b).

We solve the static problem applying different concentrated loads at P_A. For the determination of κ_1 we apply a force $\mathbf{P} = -P\mathbf{e}_3$, with $P = 1$ N. The resulting moment $\mathbf{M}^{(1)}(\theta) = (\mathbf{y}(-\pi/4) - \mathbf{y}(\theta)) \times \mathbf{F}$, with $\mathbf{y}(\theta)$ given in Eq. (4.2), is decomposed into bending and torsional components, $M_b^{(1)}(\theta) = -\mathbf{M}^{(1)}(\theta) \cdot \mathbf{n}(\theta)$ and $M_t^{(1)}(\theta) = -\mathbf{M}^{(1)}(\theta) \cdot \mathbf{t}(\theta)$, respectively. The corresponding transverse displacement $W^{(1)}$ in P_A is computed considering as static and kinematically admissible fields the ones generated by the force $\mathbf{F}$, i.e.

$$W^{(1)} = \int_{-\pi/4}^{4\pi-\pi/4} \left[\frac{(M_b^{(1)}(\theta))^2}{EI} + \frac{(M_t^{(1)}(\theta))^2}{\mu I_p} + \frac{F^2}{\mu A^*} \right] \sqrt{y'(\theta)^2 + y(\theta)^2} d\theta, \tag{4.11}$$

where $I = sh^3/12 = 1.82292$ mm^4 (second moment of area), $I_p = sh^3/3 = 7.29167$ mm^4 (polar moment of area), $A^* = 5/6sh = 18.2292$ mm^2 (shear area). The corresponding transverse stiffness is

$$\kappa_1 = \frac{P}{W^{(1)}} = 1.478\,\mathrm{N/m}. \tag{4.12}$$

For the rotational stiffnesses κ_2 and κ_3, we apply the moment $\mathbf{M}^{(2)} = -M^{(2)}\mathbf{n}_0$ and $\mathbf{M}^{(3)} = -M^{(3)}\mathbf{t}_0$, respectively, at the point P_A and we take the normalized values $M^{(2)} = M^{(3)} = 1$ Nm. Again, we derive the bending and torsional components, namely

$$\begin{aligned} M_b^{(2)} &= -\mathbf{M}^{(2)} \cdot \mathbf{n} = M^{(2)}\mathbf{n}_0 \cdot \mathbf{n}, \quad M_t^{(2)} = -\mathbf{M}^{(2)} \cdot \mathbf{t} = M^{(2)}\mathbf{n}_0 \cdot \mathbf{t}, \\ M_b^{(3)} &= -\mathbf{M}^{(3)} \cdot \mathbf{n} = M^{(3)}\mathbf{t}_0 \cdot \mathbf{n}, \quad M_t^{(3)} = -\mathbf{M}^{(3)} \cdot \mathbf{t} = M^{(3)}\mathbf{t}_0 \cdot \mathbf{t}, \end{aligned} \tag{4.13}$$

while the shear force is zero in these two cases. Then, analogously to Eq. (3.3) the rotations are

$$\phi_{n,t} = \int_{-\pi/4}^{4\pi-\pi/4} \left[\frac{(M_b^{(2,3)}(\theta))^2}{EI} + \frac{(M_t^{(2,3)}(\theta))^2}{\mu I_p} \right] \sqrt{y'(\theta)^2 + y(\theta)^2}\, d\theta, \tag{4.14}$$

which provide the rotational stiffnesses

$$\kappa_2 = \frac{M^{(2)}}{\phi_n} = 0.1337\,\mathrm{Nm}, \quad \kappa_3 = \frac{M^{(3)}}{\phi_t} = 0.1339\,\mathrm{Nm}. \tag{4.15}$$

The corresponding resonance radian frequencies are given by

$$\omega_1 = 1.403\,\mathrm{rad/s}, \quad \omega_2 = 4.823\,\mathrm{rad/s}, \quad \omega_3 = 4.827\,\mathrm{rad/s}. \tag{4.16}$$

We note that while shear deformation is negligible, torsional deformation has a major contribution of $\sim 80\%$ to the displacement (4.11) and a contribution of $\sim 40\%$ to the rotations (4.14). The capacity of the microstructured system to show low-frequency resonance modes is strictly related to the torsional deformation of the ligament, a property that was absent in previously proposed models [3, 31, 48, 121].

In Figure 4.4, we show the radian eigenfrequencies ω_1, ω_2 and ω_3 as functions of the total angular distribution $\bar{\theta}$ for spirals starting at P_A and having different

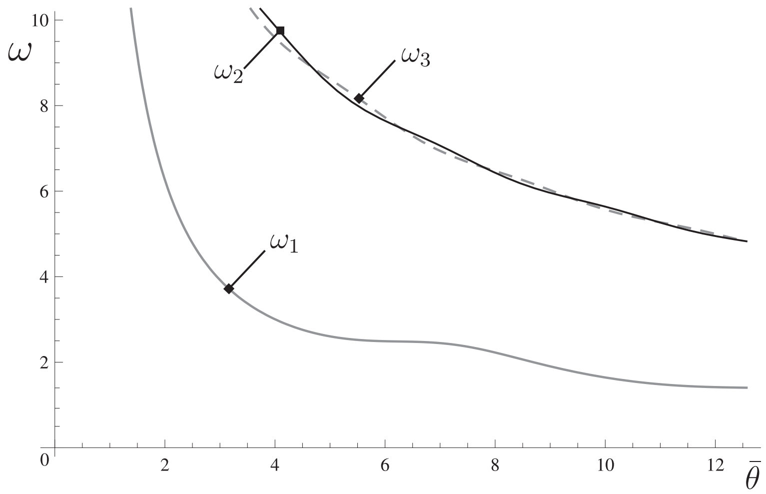

FIGURE 4.4: Radian eigenfrequencies ω_1, ω_2, ω_3 as functions of the total angular distribution $\bar{\theta}$

lengths, i.e.

$$y(\theta,\bar{\theta}) = |\mathbf{y}(\theta,\bar{\theta})| = R_0 + (R_1 - R_0)\frac{\theta + \pi/4}{4\pi}, \theta \in \left[-\frac{\pi}{4}, \bar{\theta} - \frac{\pi}{4}\right]. \tag{4.17}$$

Interestingly, ω_1 shows some oscillations that can lead to some optimal conditions for the stiffness, in the sense that a longer spiral does not necessary give an advantage for the achievement of a targeted low-frequency localized mode. Again, this has to be linked to the influence of torsional deformation that drastically increases the total compliance of the spiral. The torsion is not uniform and depends on the applied load and the geometry, leading to the oscillations of ω_i $(i = 1, 2, 3)$ in Figure 4.4. The results also point out the large reduction rate of ω_1 for $\bar{\theta} < \pi$.

The eigenfrequencies of an isolated continuous elastic resonator made of the spiral ligament, clamped at $y(3.75\pi) = R_1$, and of the central inclusion have also been computed in *Comsol Multiphysics*®. The numerical results confirm the analytical predictions and the out comes of the dispersion analysis with a first translational mode followed by two rotational modes of the central inclusion. Higher modes are associated to beam-like vibration eigenmodes of the spiral ligament [1].

Eigenfrequencies β_i $(i = 1, 2, \ldots)$ estimated analytically are compared in Table 4.1 with the eigenfrequencies of the isolated resonator and the eigenfrequencies of the localized modes in the dispersion diagram of Figure 4.2a, showing a good

[1] The interested reader could estimate analytically the eigenfrequencies of the curved beam by implementing the approximate technique shown in [117, 118, 119].

Eigenmode	(i) FEM IR	(ii) Analytical	(iii) FEM LM
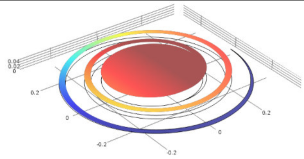	1.0173	0.9570	1.0073
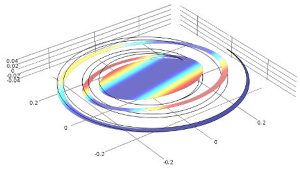	1.5295	1.7741	1.5199
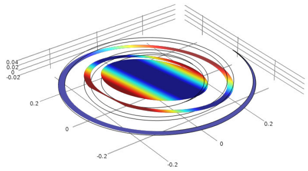	1.5458	1.7749	1.5399
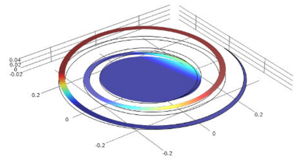	2.0929	-	2.0825
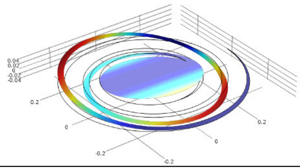	2.4003	-	2.3829

TABLE 4.1: Eigenmodes of the isolated resonator and comparison between eigenfrequencies β_i $(i = 1, 2, \ldots)$ for (i) FEM solution for the isolated resonator (IR), (ii) asymptotic analytical estimates and (iii) frequencies of the localized modes (LM) in the dispersion diagram (Figure 4.1). Colors from blue to red correspond to increasing amplitude of transverse displacement.

correspondence. In particular, the agreement between two FEM analyses for single resonator and localized modes in the dispersion diagram is excellent.

4.3.1 Modified resonator

We report a second FEM analysis for a single resonator in which we show that the difference with the analytical estimated is principally due to the connection between the inclusion and the ligament.

The modified resonator shown in Figure 4.5 has also been implemented in *Comsol Multiphysics*®. It has different connections at the ligament ends which better mimic the constraints of the monodimensional analytical model. The corresponding eigenfrequncy is $\beta_1 = 0.9331$ m^{-1}, which is in excellent agreement with the analytical prediction shown in Table 4.1.

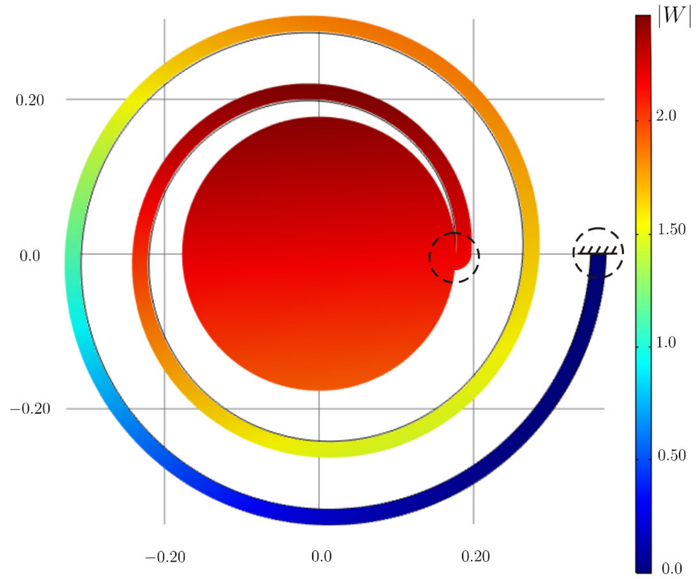

FIGURE 4.5: Modified geometry of the resonator. Spiral ligament ends have been modified. The first eigenmode is shown.

4.4 Numerical Results

In the following we show some numerical results, which highlight the capability of the microstructred platonic crystal to guide waves within the structure.

4.4.1 Trapped modes

We start analysing the macrocell shown in Figure 4.6, which includes 49 unit cells. The structure is subjected to a time-harmonic transverse force of amplitude $F = 1$ N applied at the center of the central resonator and to quasi-periodic boundary conditions.

In Figure 4.6a we show the displacement amplitude field at the frequency $\beta_I = 1.0463\,\mathrm{m}^{-1}$, corresponding to the first stop band opened by the inertial resonators (see Figure 4.2a). The strong exponential decay of the displacement amplitude is verified also for such a tiny stop band. Interestingly, the central inclusion vibrates with a translational mode whereas the next higher frequency mode, characterized

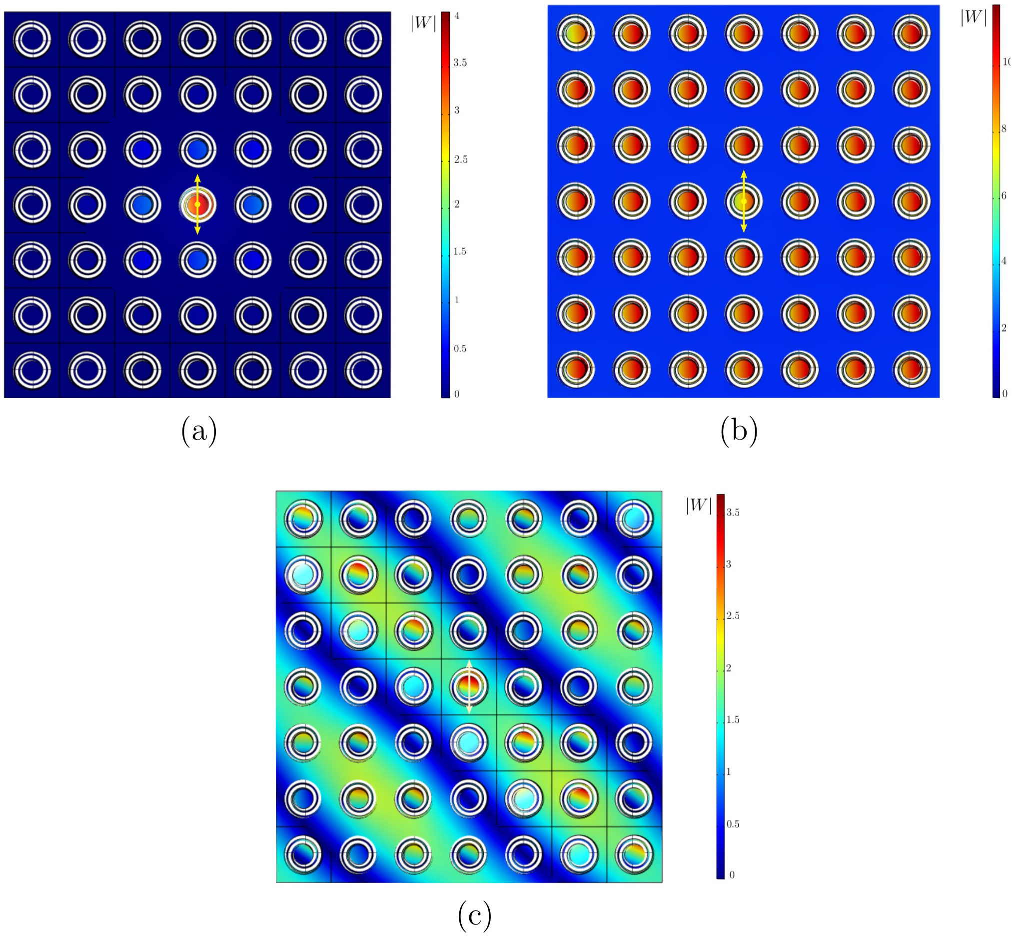

FIGURE 4.6: Periodic macrocell composed of 7×7 unit cells. Vibration modes at $\beta_I = 1.0463\,\mathrm{m}^{-1}$ (a), $\beta_{II} = 1.0619\,\mathrm{m}^{-1}$ (b) and $\beta_{III} = 1.2334\,\mathrm{m}^{-1}$ indicated in Figure 4.2. Displacement magnitude $|W|$ is shown.

by a similar exponential decay, is associated with a rotational vibration of the central inclusion.

In Figure 4.6b the frequency β_I is slightly changed to $\beta_{II} = 1.0632\,\mathrm{m}^{-1}$, corresponding to the flat band around Γ (Figure 4.2a). In this case, the wave propagates within the whole elastic system but only resonators vibrate with large amplitudes, while the plate undergoes a rigid displacement of negligible amplitude. Such an interesting behavior suggests the possibility to trap waves by properly tuning the resonance frequencies of particular sets of resonators. Such a passive system is considered in Figure 4.7, parts (a) and (b), where a number of resonators with inclusions having mass $m = 9\,\mathrm{kg}$ are arranged within the macrocell. These different inclusions are disposed along the letter 'M' in part (a) and along one diagonal in part (b). At the frequencies of $\beta = 0.5646\,\mathrm{m}^{-1}$ of $\beta = 0.5698\,\mathrm{m}^{-1}$, respectively, they show a highly localized vibration field.

In Figure 4.7c we consider a different structure: a finite plate embedding 7×7 unit cells is implemented with Neumann-type boundary conditions. Here, the 24 inclusions placed in the vicinity of the external edges have different mechanical properties (mass $m = 9\,\mathrm{kg}$). It is evident that exciting the mechanical system with a unit harmonic force applied at the bottom-left inclusion, the high amplitude vibration are localized in the vicinity of the edges.

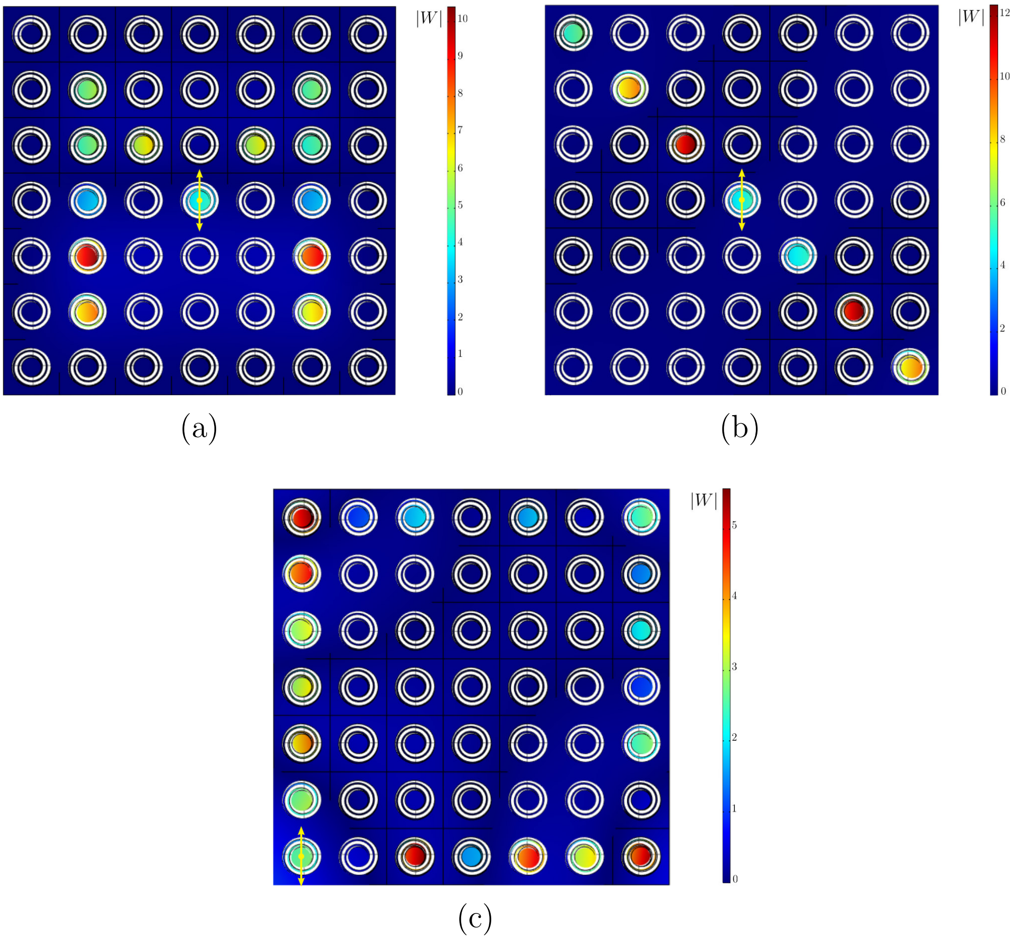

FIGURE 4.7: 'Trapped' and 'edge' modes in the microstructured plate. Trapped modes showing high amplitude vibrations concentrated on a path having the shape of the letter 'M' (a) or on a line (b) in a macrocell of the periodic system. The systems (a) and (b) are excited by a transverse time-harmonic unit force applied to the center of the central inclusion. (c) Edge mode in a finite size plate composed of 7×7 unit cells. The plate is excited by a transverse time-harmonic unit force applied to the center of the bottom left inclusion.

In Figure 4.6c the frequency is $\beta_{III} = 1.233\,\mathrm{m}^{-1}$ (see Figure 4.2). From the comparison between the dispersion diagrams of perforated and homogeneous plates in Figure 4.3, it is evident that at β_{III}, the dispersion curves show similarities with the homogeneous case. The eigenmode illustrated in the Figure evidences that a plane wave propagates within the microstructured medium with low scattering, a behavior that can be linked to perfect transmission [4, 73, 85].

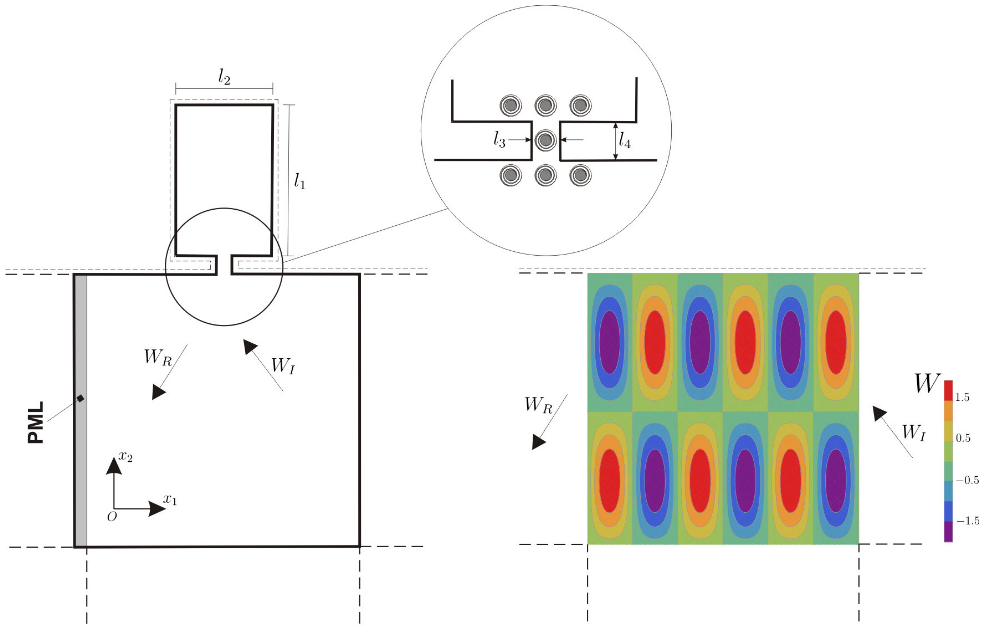

(*a*) (*b*)

FIGURE 4.8: Geometry of the system. (a) A semi-infinite plate is connected to a rectangular plate with a small ligament. Seven snail resonators are placed in the vicinity of the connection. (b) Transverse displacement contours showing the solution $W = W_I + W_R$ for a semi-infinite plate alone without resonators and with Neumann boundary conditions. Results are given for $\beta = 0.5119\,\mathrm{m}^{-1}$.

4.4.2 Transmission amplifier

Here we show how the microstructured plate can be employed in order to amplify low-frequency wave transmission between two plates. In Figure 4.8 we show the implemented geometry. A semi-infinite plate is connected to a second rectangular plate of dimensions $l_1 = 22\,\mathrm{m}$, $l_2 = 14\,\mathrm{m}$ by means of a small ligament of dimensions $l_3 = 2\,\mathrm{m}$, $l_4 = 3\,\mathrm{m}$. The mechanical and geometrical parameter of the plate are such that $\beta = 2.533\sqrt{\omega}\,\mathrm{m}^{-1}$, and Neumann-type boundary conditions are applied.

The system is excited by an incident plane-wave $W_I = e^{i\beta(x_1\cos\alpha + x_2\sin\alpha)}$, with $\alpha = 11/12\pi$, propagating from the semi-infinite plate. In part (b) of Figure 4.8, we also report the analytical solution for the semi-infinite plate alone, which involves the superposition of the incident and reflected wave $W_R = e^{i\beta[x_1\cos\alpha + (\bar{x}_2 - x_2)\sin\alpha]}$, where $x_2 = \bar{x}_2$ defines the boundary of the plate.

In order for the wave to penetrate in the second finite plate and produce high-scattering in the semi-infinite one, the wavelength of the incident wave must be small with respect to the width l_3 of the ligament. Numerical computations, not

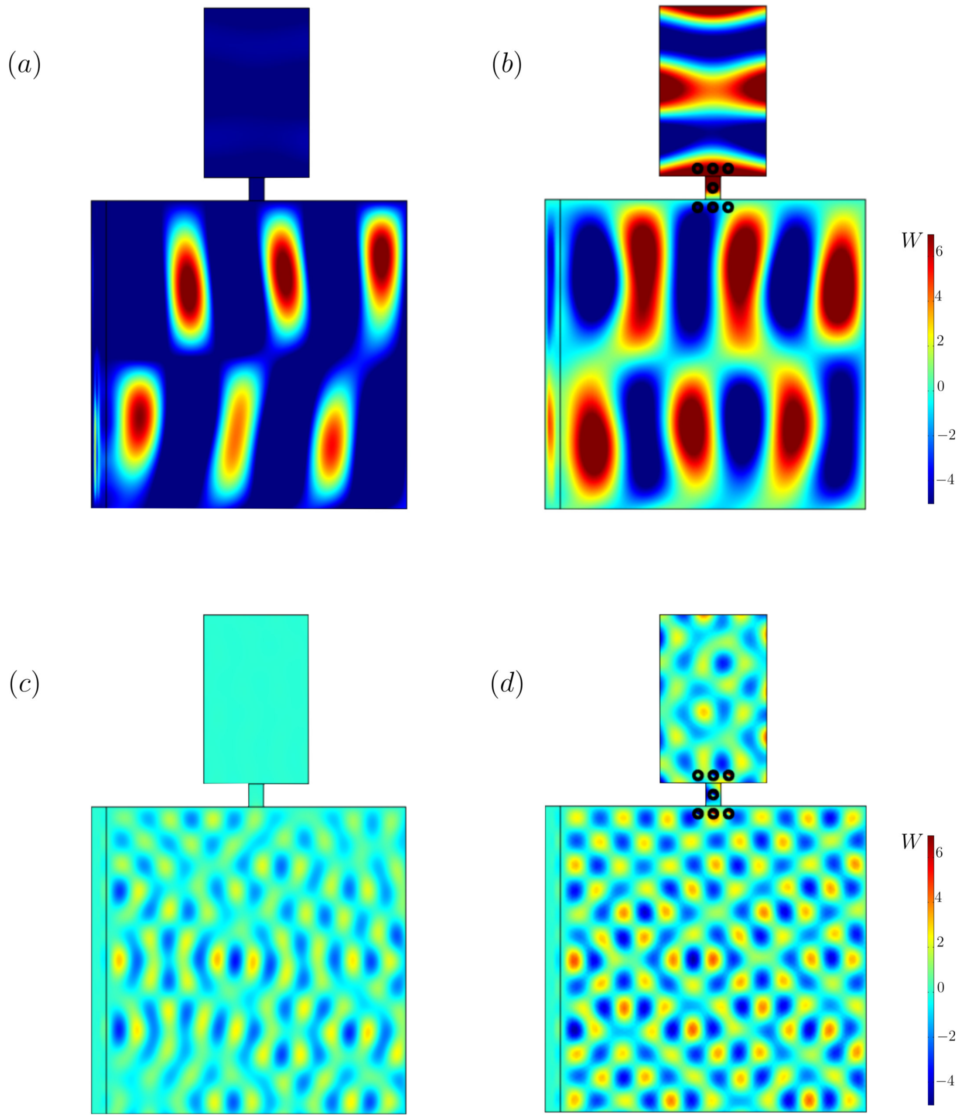

FIGURE 4.9: Vibration of a semi-inifinite plate connected to a finite rectangular plate by means of a small ligament. The geometry of the system is given in Figure 4.8. The structure is excited by the plane wave $W_I = e^{i\beta(x_1 \cos\alpha + x_2 \sin\alpha)}$, with $\alpha = 11/12\pi$. The frequency is $\beta = 0.5119\,\mathrm{m}^{-1}$ in parts (a) and (b) and $\beta = 1.4547\,\mathrm{m}^{-1}$ in parts (c) and (d). (a), (c) Homogeneous plates. (b), (d) Homogeneous plates with the addition of 7 snail resonators.

reported here for brevity, indicate approximatively $(l_3\beta\cos\alpha) > 11$. Therefore, it is needed to reach sufficiently high frequencies in order to enhance transmission of waves into the second plate.

A strongly low-frequency case is shown in Figure 4.9, where $\beta = 0.5119\,\mathrm{m}^{-1}$ ($\omega = 0.0408\,\mathrm{rad/s}$). In part (a) of the figure it is shown that the wave does not propagate in the rectangular plate and the incident wave W_I is almost entirely reflected into W_R. In part (b) of Figure 4.9, we add a system of 7 snail resonators in the vicinity of the ligament, as shown in the inset of Figure 4.8a. The geometry of the resonators is described by Eq. (4.1), with $R_0 = 0.35\,\mathrm{m}$ and $R_1 = 0.7\,\mathrm{m}$. Such a system of resonators, when activated by the incident wave W_I, is capable to excite vibrations in the finite rectangular plate enhancing the transmission. In parts (c) and (d) of Figure 4.9 the same experiment is repeated at the higher frequency $\beta = 1.4547\,\mathrm{m}^{-1}$ and a similar result is obtained, namely negligible vibrations in the finite rectangular plate for the homogeneous case and enhanced vibrations for the case with the addition of resonators.

We stress the fact that $\beta = 1.4547\,\mathrm{m}^{-1}$ is very close to the first eigenfrequency of the snail resonators, namely $\beta = 1.4469\,\mathrm{m}^{-1}$, while $\beta = 0.5119\,\mathrm{m}^{-1}$ is different not only from any eigenfrequency of resonators, but also from the eigenfrequencies of the mechanical system composed by the rectangular plate plus the tiny ligament with or without perforations and resonators.

4.4.3 Vibration suppression in a waveguide

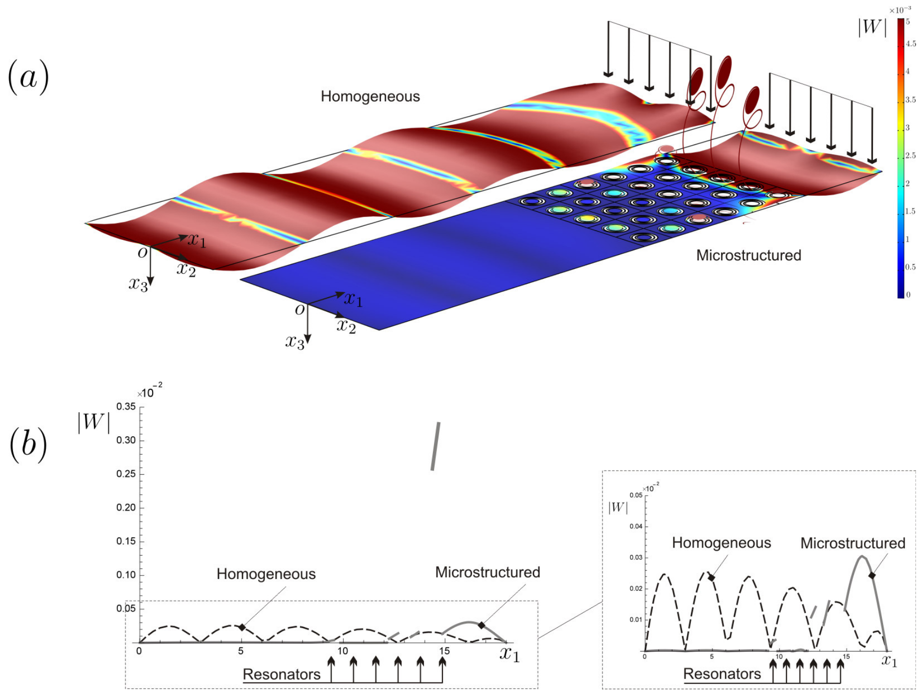

FIGURE 4.10: (a) Vibrations of a homogeneous plate vs plate with microstructured interface composed of 6×5 resonators. (b) Transverse displacement $|W|$ along the axis $x_2 = x_3 = 0$. Homogenous plate is given in black dashed line, plate with microstructured interface in continuous grey line. Displacements in the resonator inclusions are evident.

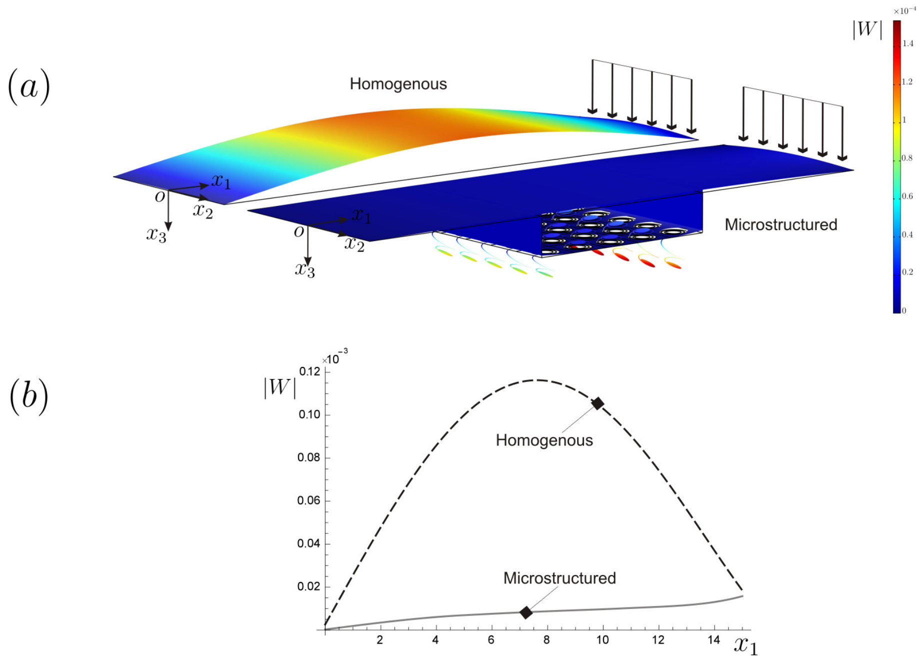

FIGURE 4.11: (a) Vibrations of a homogeneous plate vs plate with microstructured by-pass system composed of 5×5 resonators. (b) Transverse displacement $|W|$ along the axis $x_2 = x_3 = 0$. Homogenous plate is given in black dashed line, plate with by-pass system in continuous grey line.

As a final example of possible applications of the microstructured medium, we propose the design of a lightweight wave bypass structure which is capable to divert large amplitude vibrations away from load-bearing elements.

We start with a more standard approach in Figure 4.10, which involves the study of a finite structure with repetitive units as a perfect periodic structure.

The steel plate has dimensions $18\,\mathrm{m} \times 5\,\mathrm{m}$, thickness $h = 1\,\mathrm{mm}$ and it is simply supported at $x_2 = \pm 2.5\,\mathrm{m}$, $x_1 = 0, 3, 6, 9, 12, 15, 18\,\mathrm{m}$ and $x_2 = 0\,\mathrm{m}$, $x_1 = 0, 18\,\mathrm{m}$. The structure is subjected to a harmonic transverse edge load at $x_1 = 18\,\mathrm{m}$ having magnitude equal to $1\,\mathrm{N/m}$. In Figure 4.10 the load is vibrating with frequency $f = 0.25\,\mathrm{Hz}$, i.e. $\beta = 0.3507\,\mathrm{m}^{-1}$, which corresponds to the first eigenfrequency of the finite plate or to the frequency of the first stationary mode within the dispersion diagram of the periodic homogeneous plate composed by repetitive units of dimensions $3\,\mathrm{m} \times 5\,\mathrm{m}$. The vibration mode is presented on the upper part of Figure 4.10a.

In order to reduce vibration on the left part of the plate, we introduce an interface composed of 6 lines of 5 square units having the geometry shown in Figure 4.1a. The microstructured plate is shown in the lower part of Figure 4.10b. The geometrical parameters of the resonators are predesigned following the asymptotic model reported in Section 4.3 in order to match with the first eigenfrequency $\beta = 0.3507\,\mathrm{m}^{-1}$, associated with a translational vibration of the inclusion. In this step we consider a single isolated snail resonator.

A more refined tuning of the geometrical parameters leads to full coupling between the resonators and the plate. This is done analyzing numerically the full structure with the microstructured interface. In particular, we have chosen to change the in-plane thickness of the ligament in the resonators in order to obtain the desired wave filtering. The final geometrical properties are: $R_0 = 0.175\,\mathrm{m}$, $R_1 = 0.35\,\mathrm{m}$, in plane thickness $s = 21.875\,\mathrm{mm}$.

Such a system of resonators is capable to open a tiny band gap at $\beta = 0.3507\,\mathrm{m}^{-1}$. The vibration amplitudes shown in Figure 4.10 demonstrate the capability of the interface to block wave propagation within the plate. The incoming waves are reflected by the interface and the displacements decay exponentially fast. Such a system is highly effective and does not require a heavy variation of the original structure. In the proposed case the final structure is even lighter than the original one.

The drawback of the proposed approach is that the energy is reflected back by the interface and still excites the region $x_1 \geq 15\,\mathrm{m}$ ahead of the interface. The displacements in the inset of part (b) of Figure 4.10 show that the amplitudes of vibrations in this region are larger than those in the homogeneous case.

In Figure 4.11 we propose an alternative approach, which is capable to re-route wave propagation within the whole structure. In particular, we consider an initial steel rectangular plate having dimensions $15\,\mathrm{m} \times 5\,\mathrm{m}$, thickness $h = 25\,\mathrm{mm}$ and simple supports at $x_1 = 0$, $15\,\mathrm{m}$ and $x_2 = \pm 2.5\,\mathrm{m}$.

The microstructured plate is now connected in 'parallel' to the main structure in the central region $5\,\mathrm{m} \leq x_1 \leq 10\,\mathrm{m}$. The design procedure of the microstructure plate follows the same scheme detailed above, with a first predesign step on a single resonator followed by the analysis of the full structure shown in the bottom part of Figure 4.11a in order to obtain full coupling between the initial plate and the attached by-pass system.

The comparisons between the deformed shapes shown in part (a) of Figure 4.11 and displacement magnitudes along the axis $x_2 = x_3 = 0$ shown in part (b), reveal a drastic reduction in the displacement amplitudes. We stress that the amplitude reduction is extended to the entire initial structure, which has changed the vibration mode under the excitation of the edge load at $x_1 = 15\,\mathrm{m}$. In the modified structure the upper plate displays low amplitude vibrations and wave propagation is forced to be redirected into the system of resonators.

Finally, we stress that the study is within the elastic range and we do not consider any energy dissipation effect. Clearly, the energy diverted to the resonators could be stored or dissipated. It is also evident that damping system can be efficiently placed in correspondence of the resonators.

Conclusions

An analytical PML model for flexural waves in beam structures is proposed. The excellent agreement with analytical Green's function for infinite domain is shown, the error in the case of non-perfect additional boundary conditions is estimated and the influence of discretization is also given.

Particular importance has been given to the physical interpretation of the transformed equations in order to show that the method is simple and can be implemented in standard finite element packages; the eigenfrequency analysis may also be used as a simple check of the correctness of the implementation.

The PMLs for flexural waves can be particularly useful in the analysis of elongated structures like bridges and pipelines and comparisons with analytical results for infinitely long structures

The analytical model of PMLs for flexural waves is then extended to Kirchoff-Love plates. The model is based on geometry transformation techniques and a physical interpretation of the transformed equation is given. The analysis of reflection at the interface between homogeneous and transformed PML domain introduces constraints on the transformation. It also shows the difference with problems governed by Helmholtz equations, where the boundary conditions are automatically satisfied.

The amount of reflection induced by the introduction of fictitious boundary conditions is analysed quantitatively by evaluating the *quality factor*, that measures the difference between a numerical solution in a finite computational domain and an analytical solution in free space. Investigation of the effect of different frequencies, geometrical and dissipative parameters show that the proposed PML performs well and the comparison with the analytical solution is excellent. We also demonstrated that simple support is the best boundary condition.

We envisage applications of the proposed model in several numerical codes for the analysis of vibrations of plate structures and in elastic metamaterials. The physical interpretation of the PMLs can also be used in experimental setups mimicking infinite plates.

The natural development of the proposed model is the implementation of PMLs for flexural waves in the transient regime.

In the second part of the work a *platonic* crystal is proposed. The microstructured medium can lead to wave localization, wave trapping and edge waves. It has also been applied to re-route waves in order to produce low amplitude vibration on the main structure.

The design of the model is simplified by the possibility to estimate analytically or numerically resonance frequencies of the inertial resonators. Simple geometrical parameters may be used to have specific effects at targeted frequencies.

The proposed structured plate is very attractive for technologically applications since it is a single phase material and it can be produced at low cost by existing technologies. Standard techniques are additive manufacturing at small scale and water jet cutting or laser cutting on homogeneous plates at larger scales.

Publications

1) M. Morvaridi and M. Brun. Perfectly Match Layers for flexural waves: An Exact analytical model. International Journal of Solids and Structures. 102-103: 1-9, 2016. doi: 10.1016/j.ijsolstr.2016.10.024

2) M. Morvaridi and M. Brun. Invariance of eigenfrequencies and eigenmodes under geometric transformation in elongated elastic structures. Proceedings of the 7th European Congress on Computational Methods in Applied Sciences and Engineering. 2:4436-4444, 2016.

3) M. Morvaridi and M. Brun. Perfectly Matched Layers for flexural waves in Kirchhoff-Love plates. International Journal of Solids and Structures. In press 2017.

4) M. Morvaridi and M. Brun. Invariance of eigenfrequencies under geometric transformation in plate structures. Proceedings of the XXIII Conference of The Italian Association of Theoretical and Applied Mechanics. 5:2130-2140, 2017.

5) M. Morvaridi and G. Carta and M. Brun. Platonic crystal with low-frequency locally resonant snail structures. In preparation.

Bibliography

[1] G. Acar and C. Yilmaz. Experimental and numerical evidence for the existence of wide and deep phononic gaps induced by inertial amplification in two-dimensional solid structures. *Journal of Sound and Vibration*, 32(24): 6389–6404, 2013. doi: 10.1006/jsvi.1996.0076.

[2] M. H. Aliabadi. *The Boundary Element Method, Applications in Solids and Structures*, volume 2. John Wiley Andamp, Sons, Ltd, West Sussex, England, March 2002. ISBN 978-0-470-84298-0.

[3] T. Antonakakis, R. Craster, and S. Guenneau. Moulding and shielding flexural waves in elastic plates. *European Physics Letters*, 105(4):54004, 2014. doi: 10.1209/0295-5075/105/54004.

[4] T. Antonakakis, R. V. Craster, and S. Guenneau. Homogenisation for elastic photonic crystals and dynamic anisotropy. *The Journal of the Mechanics and Physics of Solids*, 71(1):84–96, 2014. doi: 10.1016/j.jmps.2014.06.006.

[5] R. J. Astley and J. A. Hamilton. The stability of infinite elements schemes for transient wave problems. *Computer Methods in Applied Mechanics and Engineering*, 195(29–32):3553–3571, 2006. doi: 10.1016/j.cma.2005.01.026.

[6] E. Baravelli and M. Ruzzene. Internally resonating lattices for bandgap generation and low-frequency vibration control. *Journal of Sound and Vibration*, 332(25):6562–6579, 2013. doi: 10.1016/j.jsv.2013.08.014.

[7] G. Beer. *Programming the Boundary Element Method: An Introduction for Engineers*, volume 1. Wiley, Chichester, England, March 2001. ISBN 978-0-471-86333-5.

[8] J. P. Berenger. A perfectly matched layer for the absorption of electromagnetic waves. *Journal of Computational Physics*, 114(2):185–200, 1994. doi: 10.1006/jcph.1994.1159.

[9] K. Bertoldi, M. Brun, and D. Bigoni. A new boundary element technique without domain integrals for elastoplastic solids. *International Journal for Numerical Methods in Engineering*, 64:877–906, 2005. doi: 10.1002/nme.1385.

[10] P. Bettess. *Infinite Elements*. Penshaw Press, UK, 1992. ISBN 0-9518806-0-8.

[11] P. Bettess and O. C. Zienkiewicz. Diffraction and refraction of surface waves using finite and infinite elements. *International Journal for Numerical Methods in Engineering*, 11(8):1271–1290, 1977. doi: 10.1002/nme.1620110808.

[12] D. Bigoni, S. Guenneau, A. B. Movchan, and M. Brun. Elastic metamaterials with inertial locally resonant structures: Application to lensing and localization. *Physical Review B*, 87:174303, 2013. doi: 10.1103/PhysRevB.87.174303.

[13] M. Bonnet. *Boundary Integral Equation Methods for Solids and Fluids*. Wiley, Chishester, April 1999. ISBN 978-0-471-97184-9.

[14] L. Brillouin. *Wave propagation in periodic structures*. McGraw-Hill, 1946. ISBN 0486495566.

[15] M. Brun, D. Bigoni, and D. Capuani. A boundary element technique for incremental, non-linear elasticity. part ii: Bifurcation and shear bands. *Computer Methods in Applied Mechanics and Engineering*, 192:2481–2499, 2003. doi: 10.1016/S0045-7825(03)00272-X.

[16] M. Brun, D. Capuani, and D. Bigoni. A boundary element technique for incremental, non-linear elasticity. part i: Formulation. *Computer Methods in Applied Mechanics and Engineering*, 192:2461–2479, 2003. doi: 10.1016/S0045-7825(03)00268-8.

[17] M. Brun, S. Guenneau, and A. B. Movchan. Achieving control of in-plane elastic waves. *Applied Physics Lettters*, 94:061903, 2009. doi: 10.1063/1.3068491.

[18] M. Brun, S. Guenneau, A. B. Movchan, and D. Bigoni. Dynamics of structural interfaces: filtering and focussing effects for elastic waves. *Journal of the Mechanics and Physics of Solids*, 58(9):1212–1224, 2010. doi: 10.1016/j.jmps.2010.06.008.

[19] M. Brun, G. Giaccu, A. Movchan, and N. Movchan. Asymptotics of eigenfrequencies in the dynamic response of elongated multi-structures. *Proceedings of the Royal Society A*, 468(2138):378–394, 2012. doi: 10.1098/rspa.2011.0415.

[20] M. Brun, D. Colquitt, I. Jones, A. Movchan, and N. Movchan. Transformation cloaking and radial approximations for flexural waves in elastic plates. *New Journal of Physics*, 16:093020, 2014. doi: 10.1088/1367-2630/16/9/093020.

[21] D. S. Burnett. A three-dimensional acoustic infinite element based on a generalized multipole expansion. *The Journal of the Acoustical Society of America*, 96(5):2798–2816, 1994. doi: 10.1121/1.411286.

[22] W. Cai and V. Shalaev. *Optical Metamaterials: Fundamentals and Applications*. 2009. ISBN 1441911502.

[23] F. Capolino. *Metamaterials Handbook - Two Volume Slipcase Set*. 2009. ISBN 1420053620.

[24] G. Carta, I. S. Jones, N. V. Movchan, A. B. Movchan, and M. J. Nieves. Gyro-elastic beams for the vibration reduction of long flexural systems. *Proceedings of the Royal Society A*, 473(20170136), 2017. doi: 10.1098/rspa.2017.0136.

[25] C. Cerjan, D. Kosloff, R. Kosloff, and M. Reshef. A nonrefecting boundary condition for discrete acoustic and elastic wave equations. *Geophysics*, 50: 705–708, 1985. doi: 10.1190/1.1441945.

[26] Z. Chang, D. Guo, X. Q. Feng, and G. Hu. A facile method to realize perfectly matched layers for elastic waves. *Wave Motion*, 51(7):1170–1178, 1972. doi: 10.1016/j.wavemoti.2014.07.003.

[27] H. Chen and C. Chan. Acoustic cloaking in three dimensions using acoustic metamaterials. *Applied Physics Letters*, 91:183518, 2007. doi: 10.1063/1.2803315.

[28] W. C. Chew and W. H. Weedon. A 3d perfectly matched medium modified maxwell's equations with stretched coordinates. *Microwave optical Tech. Letters*, 7(13):599–604, 1994. doi: 10.1002/mop.4650071304.

[29] D. Chronopoulos, I. Antoniadis, and T. Ampatzidis. Enhanced acoustic insulation properties of composite metamaterials having embedded negative stiffness inclusions. *Extreme Mechanics Letters*, 12:48–54, 2017. doi: 10.1016/j.eml.2016.10.012.

[30] D. Clouteau, R. Cottereau, and G. Lombaert. Dynamics of structures coupled with elastic media-a review of numerical models and methods. *Journal of Sound and Vibration*, 332(10):2415–2436, 2013. doi: 10.1016/j.jsv.2012.10.011.

[31] A. Colombi, P. Roux, S. Guenneau, and M. Rupin. Directional cloaking of flexural waves in a plate with a locally resonant metamaterial. *The Journal of the Acoustical Society of America*, 137(4):1783, 2015. doi: 10.1121/1.4915004.

[32] D. Colquitt, I. Jones, N. Movchan, A. Movchan, M. Brun, and R. McPhedran. Making waves round a structured cloak: lattices, negative refraction and fringes. *Proceedings of the Royal Society A*, 469(2157):20130218, 2013. doi: 10.1098/rspa.2013.0218.

[33] D. Colquitt, M. Brun, M. Gei, A. Movchan, N. Movchan, and I. Jones. Transformation elastodynamics and cloaking for flexural waves. *Journal of the Mechanics and Physics of Solids*, 72:131–143, 2014. doi: 10.1016/j.jmps.2014.07.014.

[34] R. V. Craster and S. Guenneau. *Acoustic Metamaterials: Negative Refraction, Imaging, Lensing and Cloaking (Springer Series in Materials Science).* 2012. ISBN 9400748124.

[35] L. Cremers and K. R. Fyfe. On the use of variable order infinite wave envelope elements for acoustic radiation and scattering. *The Journal of the Acoustical Society of America*, 97(4):2028–2040, 1995. doi: 10.1121/1.411994.

[36] N. Engheta and R. W. Ziolkowski. *Electromagnetic Metamaterials: Physics and Engineering Explorations.* 2006. ISBN 0471761028.

[37] M. Farhat, S. Guenneau, and S. Enoch. Ultrabroadband elastic cloaking in thin plates. *Physical Review Letters*, 103(2):024301, 2009. doi: 10.1098/rspa.2012.0123.

[38] M. Farhat, S. Guenneau, S. Enoch, and A. Movchan. Cloaking bending waves propagating in thin elastic plates. *Physical Review B*, 79(3):033102, 2009. doi: 10.1103/PhysRevB.79.033102.

[39] M. Farhat, S. Guenneau, and S. Enoch. High directivity and confinement of flexural waves through ultra-refraction in thin perforated plates. *European Physics Letters*, 91(5):54003, 2010. doi: 10.1209/0295-5075/91/54003.

[40] M. Farhat, P. Chen, S. Guenneau, and S. Enoch. *Transformation Wave Physics: Electromagnetics, Elastodynamics, and Thermodynamics*. CRC Press, 2016.

[41] M. Farzanian and F. Arbabi. A pml solution for vibration of infinite beams on elastic supports under seismic loads. *Journal of Seismology and Earthquake Engineering*, 16(1):1–16, 2014.

[42] N. M. M. Frandsen, O. R. Bilal, J. S. Jensen, and M. I. Hussein. Inertial amplification of continuous structures: Large band gaps from small masses. *Journal of Applied Physics*, 119(12):124902, 2016. doi: 10.1063/1.4944429.

[43] L. Gaul, M. Kögl, and M. Wagner. *Boundary Element Methods for Engineers and Scientists: An Introductory Course with Advanced Topics*, volume 1. Springer, Verlag Berlin Heidelberg, 2003. ISBN 978-3-642-05589-8.

[44] L. Geli, P. Bard, and B. Jullien. The effect of topography on earthquake ground motion: a review and new results. *Bulletin of the Seismological Society of America*, 78(1):42–63, 1988.

[45] K. Gerdes. A review of infinite element methods for exterior helmholtz problems. *Journal of Computational Acoustics*, 8(1):43–62, 2000. doi: 10.1016/S0218-396X(00)00004-2.

[46] D. Givoli. Non-reflecting boundary conditions: review article. *Geophysics*, 94(1):1–29, 1991. doi: 10.1016/0021-9991(91)90135-8.

[47] T. Hagstrom and S. Hariharan. A formulation of asymptotic and exact boundary conditions using local operators. *Applied Numerical Mathematics*, 27:403–416, 1998.

[48] S. G. Haslinger, N. V. Movchan, I. S. Jones, and R. V. Craster. Controlling flexural waves in semi-infinite platonic crystals with resonator-type scatterers. *The Quarterly Journal of Mechanics and Applied Mathematics*, 70(3): 216–247, 2017. doi: 10.1093/qjmam/hbx005.

[49] F. D. Hastings, J. B. Schneider, and S. L. Broschat. Application of the perfectly matched layer (pml) absorbing boundary conditions to elastic wave propagation. *The Journal of the Acoustical Society of America*, 100(5):3061–3069, 1996. doi: 10.1121/1.417118.

[50] R. Higdon. Absorbing boundary conditions for elastic waves. *Geophysics*, 56(2):231–241, 1991. doi: 10.1190/1.1443035.

[51] G. H. Hu, A. Rathsfeld, and T. Yin. Finite element method to fluid-solid interaction problems with unbounded periodic interfaces. *Numerical Methods for Partial Differential Equations*, 32(1):5–35, 2016. doi: 10.1002/num.21980.

[52] M. I. Hussein, M. J. Leamy, and M. Ruzzene. Dynamics of phononic materials and structures: Historical origins, recent progress, and future outlook. *Applied Mechanics Reviews*, 66(4):040802, 2014. doi: 10.1115/1.4026911.

[53] F. Ihlenburg. *Finite Element Analysis of Acoustic Scattering.* Springer, Verlag New York, 1998. ISBN 978-0-387-22700-9.

[54] I. S. Jones, M. Brun, N. V. Movchan, and A. B. Movchan. Singular perturbations and cloaking illusions for elastic waves in membranes and kirchhoff plates. *International Journal of Solids and Structures*, 69–70:498–506, 2015. doi: 10.1016/j.ijsolstr.2015.05.001.

[55] M. Kadic, T. Bückmann, R. Schittny, and M. Wegener. Metamaterials beyond electromagnetism. *Reports on Progress in Physics*, 76(12):126501, 2013. doi: 10.1088/0034-4885/76/12/126501.

[56] K.F.Graff. *Wave motion in elastic solids.* Oxford University Press, 1975. ISBN 0198561180.

[57] J. Kim and H. S. Kim. Finite element analysis of piezoelectric underwater transducers for acoustic characteristics. *Journal of Mechanical Science and Technology*, 23(1):452–460, 2009. doi: 10.1007/s12206-008-1126-x.

[58] D. Komatitsch and J. Tromp. A perfectly matched layer absorbing boundary condition for the second-order seismic wave equation. *Geophysical Journal International*, 154(1):146–153, 2003. doi: 10.1046/j.1365-246X.2003.01950.x.

[59] J. Kristek, P. Moczo, and M. Galis. A brief summary of some pml formulations and discretizations for the velocity-stress equation of seismic motion. *Studia Geophysica et Geodaetica*, 53(1):459–474, 2009. doi: 10.1007/s11200-009-0034-6.

[60] Y. Lai, Y. Wu, P. Sheng, and Z. Q. Zhang. Hybrid elastic solids. *Nature Materials*, 10(5):620–624, 2011. doi: 10.1038/nmat3043.

[61] G. Lancioni. Numerical comparison of high-order absorbing boundary conditions and perfectly matched layers for a dispersive one-dimensional medium. *Computer Methods in Applied Mechanics and Engineering*, 209-212:74–86, 2012. doi: 10.1016/j.cma.2011.10.015.

[62] N. Landy and D. Smith. A full-parameter unidirectional metamaterial cloak for microwaves. *Nature Materials*, 12:25–28, 2013. doi: 10.1038/nmat3476.

[63] J. H. Lee and J. L. Tassoulas. Foam structure with a negative poisson's ratio. *Computer Methods in Applied Mechanics and Engineering*, 200(13-16):1509–1525, 2011. doi: 10.1016/j.cma.2011.01.004.

[64] R. Leis. *Initial Boundary Value Problems in Mathematical Physics*. Teubner Verlag, Wiesbaden, 1986. ISBN 978-3-663-10649-4.

[65] U. Leonhardt. Optical conformal mapping. *Science*, 312(5801):1777–1780, 2006. doi: 10.1126/science.1126493.

[66] G. Liu and J. S. Quek. A non-reflecting boundary for analyzing wave propagation using the finite element method. *Finite Element in Analysis and Design*, 39(5–6):403–417, 2003. doi: 10.1016/S0168-874X(02)00081-1.

[67] Z. Liu, X. Zhang, Y. Mao, Y. Y. Zhu, Z. Yang, C. T. Chan, and P. Sheng. Locally resonant sonic materials. *Science*, 289(5485):1734–1736, 2000. doi: 10.1126/science.289.5485.1734.

[68] S. H. Lo and W. X. Wang. Generation of finite element mesh with variable size over an unbounded 2d domain. *Computer Methods in Applied Mechanics and Engineering*, 194(45–47):4668–4684, 2005. doi: 10.1016/j.cma.2004.12.011.

[69] J. Lysmer and R. Kuhlemeyer. Finite dynamic model for in
nite media. *Journal of the Engineering Mechanics Division, Proc. ASCE*, 95 (4):859–878, 1969. doi: 10.1002/pssb.201084223.

[70] G. Ma, C. Fu, G. wang, P. D. Hougne, J. Christensen, Y. Lai, and P. Sheng. Polarization bandgaps and fluid-like elasticity in fully solid elastic metamaterials. *Nature Communications*, 7(13536), 2016. doi: 10.1038/ncomms13536.

[71] G. Maier, S. Miccoli, U. Perego, and G. Novati. Symmetric galerkin boundary element method in plasticity and gradient plasticity. *Computational Mechanics*, 17(1):115–129, 1995. doi: 10.1007/BF00356484.

[72] R. McPhedran, A. Movchan, and N. Movchan. Platonic crystals: bloch bands, neutrality and defects. *Mechanics of Materials*, 41(4):356–363, 2009. doi: 10.1016/j.mechmat.2009.01.005.

[73] R. McPhedran, A. Movchan, N. Movchan, M. Brun, and M. Smith. Parabolic trapped modes and steered dirac cones in platonic crystals. *Proceedings of the Royal Society A*, 471(2177):20140746, 2015. doi: 10.1098/rspa.2011.0415.

[74] D. M. Mead. Wave propagation in continuous periodic structures: Research contributions from southampton, 1964–1995. *Journal of Sound and Vibration*, 190(3):495–524, 1996. doi: 10.1006/jsvi.1996.0076.

[75] G. W. Milton, M. Briane, and J. R. Willis. On cloaking for elasticity and physical equations with a transformation invariant form. *New Journal of Physics*, 8:248, 2006. doi: 10.1088/1367-2630/8/10/248.

[76] D. Misseroni, D. J. C. A. B. Movchan, N. V. Movchan, and I. S. Jones. Cymatics for the cloaking of flexural vibrations in a structured plate. *Scientific Reports*, 6(23929), 2016. doi: 10.1038/srep23929.

[77] M. Morvaridi and M. Brun. Perfectly match layers for flexural waves: An exact analytical model. *International Journal of Solids And Structures*, 102–103:1–9, 2016. doi: 10.1016/j.ijsolstr.2016.10.024.

[78] A. B. Movchan, N. V. Movchan, and R. C. McPhedran. Bloch-floquet bending waves in perforated thin plates. *Proceedings of the Royal Society A*, 463 (2):2505–2518, 2007. doi: 10.1098/rspa.2007.1886.

[79] N. V. Movchan, R. C. McPhedran, A. B. Movchan, and C. G. Poulton. Wave scattering by platonic grating stacks. *Proceedings of the Royal Society A*, 465(4):3383–3400, 2009. doi: 10.1098/rspa.2009.0301.

[80] F. Nataf. New constructions of perfectly matched layers for the linearized euler equations. *Comptes Rendus Mathematique*, 340(10):775–778, 2005. doi: 10.1016/j.crma.2005.04.013.

[81] F. Nataf. Absorbing boundary conditions and perfectly matched layers in wave propagation problems. *Radon Series on Computational and Applied Mathematics*, 11:219–231, 2013. URL https://hal.archives-ouvertes.fr/hal-00799759.

[82] A. Norris. Acoustic cloaking theory. *Proceedings of the Royal Society A*, 464 (2097):2411–2434, 2008. doi: 10.1098/rspa.2008.0076.

[83] A. N. Norris and A. L. Shuvalov. "elastic cloaking theory. *Wave Motion*, 48 (6):525–538, 2011. doi: 10.1016/j.wavemoti.2011.03.002.

[84] G. Novati and C. A. Brebbia. Boundary element formulation for geometrically nonlinear elastostatics. *Applied Mathematical Modelling*, 6(2):136–138, 1982. doi: 10.1016/0307-904X(82)90025-7.

[85] J. O'Neill, O. Selsil, S. G. Haslinger, N. V. Movchan, and R. V. Craster. Active cloaking for finite clusters of pins in kirchhoff plates. *SIAM Journal on Applied Mathematics*, 77(4):1115–1135, 2017. doi: 10.1098/rspa.2014.0746.

[86] W. Parnell, A. Norris, and T. Shearer. Employing pre-stress to generate finite cloaks for antiplane elastic waves. *Applied Physics Letters*, 100(17): 171907, 2012. doi: 10.1063/1.4704566.

[87] S. L. Parvanova, P. S. Dineva, G. D. Manolis, and P. N. Kochev. Dynamic response of a solid with multiple inclusions under anti-plane strain conditions by the bem. *Computers & Structures*, 139:65–83, 2014. doi: 10.1016/j.compstruc.2014.04.002.

[88] J. Pendry, D. Schurig, and D. Smith. Controlling electromagnetic fields. *Science*, 312(5781):1780–1782, 2006. doi: 10.1126/science.1125907.

[89] N. Phan-Thien. Rubber-like elasticity by boundary element method: Finite deformation of a circular elastic slice. *Rheologica Acta*, 27(3):230–240, 1988. doi: 10.1007/BF01329739.

[90] A. Piccolroaz, A. Movchan, and L. Cabras. Rotational inertia interface in a dynamic lattice of flexural beams. *International Journal of Solids and Structures*, 112:43–53, 2017. doi: 10.1016/j.ijsolstr.2017.02.023.

[91] A. Piccolroaz, A. Movchan, and L. Cabras. Dispersion degeneracies and standing modes in flexural waves supported by rayleigh beam structures. *International Journal of Solids and Structures*, 109:152–165, 2017. doi: 10.1016/j.ijsolstr.2017.01.017.

[92] C. Polizzotto. An energy approach to the boundary element method. part ii: Elastic-plastic solids. *Computer Methods in Applied Mechanics and Engineering*, 69(3):263–276, 1998. doi: 10.1016/0045-7825(88)90043-6.

[93] C. Polizzotto. A symmetric galerkin boundary/domain element method for finite elastic deformations. *Computer Methods in Applied Mechanics and Engineering*, 189(2):481–514, 2000. doi: 10.1016/S0045-7825(99)00303-5.

[94] E. Post. *Formal Structure of Electromagnetics: General Covariance and Electromagnetics*. 1962. ISBN 9780486654270. URL http://books.google.it/books?id=zXeuy8psmegC.

[95] C. G. Poulton, R. C. McPhedran, N. V. Movchan, and A. B. Movchan. Convergence properties and flat bands in platonic crystal band structures using the multipole formulation. *Waves in Random and Complex Media*, 20(4):702–716, 2010. doi: 10.1080/17455030903203140.

[96] Q. Qi and T. L. Geers. Evaluation of the perfectly matched layer for computational acoustics. *Journal of Computational Physics*, 139(1):166–183, 1998.

[97] A. Quarteroni, A. Tagliani, and E. Zampieri. Generalized galerkin approximations of elastic waves with absorbing boundary conditions. *Computer Methods in Applied Mechanics and Engineering*, 163(1–4):323–341, 1998.

[98] C. M. Rappaport. Interpreting and improving the pml absorbing boundary condition using anisotropic lossy mapping of space. *IEEE Transactions on Magnetics*, 32(3):968–974, 1996. doi: 10.1109/20.497403.

[99] D. Robinovich, D. Givoli, J. Bielak, and et al. A finite element scheme with a high order absorbing boundary condition for elastodynamics. *Computer Methods in Applied Mechanics and Engineering*, 200(23–24):2048–2066, 2011. doi: 10.1016/j.cma.2011.03.006.

[100] A. Romero, A. Tadeu, P. Galvin, and J. Antonio. 2.5d coupled bem-fem used to model fluid and solid scattering wave. *International Journal for Numerical Methods In Engineering*, 101(2):148–164, 2015. doi: 10.1002/nme.4801.

[101] D. V. S. Guenneau, C. Amra. Transformation thermodynamics: cloaking and concentrating heat flux. *Proceedings of the Royal Society A: Mathematical, Physical and Engineering Sciences*, 20(7):8207–8218, 2012. doi: 10.1364/OE.20.008207.

[102] D. S. S.A. Cummer. One path to acoustic cloaking. *New Journal of Physics*, 9(45):45, 2007. doi: 10.1088/1367-2630/9/3/045.

[103] Z. S. Sacks, D. M. Kingsland, R.Lee, and J-F.Lee. A perfectly matched anisotropic absorber for use as an absorbing boundary condition. *IEEE Transaction on Antennas and Propagation*, 43(12):1460–1463, 1995. doi: 10.1109/8.477075.

[104] R. Schittny, M. Kadic, S. Guenneau, and M. Wegener. Experiments on transformation thermodynamics: molding the flow of heat. *Physical Review Letters*, 110:195901, 2013. doi: 10.1364/OE.20.008207.

[105] D. Schurig, J. Mock, B. Justice, S. Cummer, J. Pendry, A. Starr, and D. Smith. Metamaterial electromagnetic cloak at microwave frequencies. *Science*, 314(5801):977–980, 2006. doi: 10.1126/science.1133628.

[106] M. J. A. Smith, R. C. McPhedran, C. G. Poulton, and M. H. Meylan. Negative refraction and dispersion phenomena in platonic clusters. *Waves Random Complex Media*, 22(4):435–458, 2012. doi: 10.1080/17455030.2012.711495.

[107] M. J. A. Smith, M. H. Meylan, A. B. Movchan, and C. G. Poulton. A short remark on the band structure of free-edge platonic crystals. *Waves in Random and Complex Media*, 24(4):421–430, 2014. doi: 10.1080/17455030.2014.936534.

[108] J. Sochacki, R. Kubichek, J. George, W. Fletcher, and S. Smithson. Absorbing boundary conditions and surface waves. *"Geophysics*, 52:60–71, 1987. doi: 10.1190/1.1442241.

[109] R. Song, J. Ma, and K. Wang. The application of the non splitting perfectly matched layer in numerical modeling of wave propagation in poroelastic media. *Applied Geophysics*, 2(4):216–222, 2005. doi: 10.1007/s11770-005-0027-3.

[110] C. Steele. A critical review of some traffic noise prediction models. *Applied Acoustics*, 62(3):271–287, 2001. doi: 10.1016/S0003-682X(00)00030-X.

[111] N. Stenger, M. Wilhelm, and M. Wegener. Experiments on elastic cloaking in thin plates. *Physical Review Letters*, 108(1):014301, 2012. doi: 10.1103/PhysRevLett.108.014301.

[112] J. L. Tassoulas and E. Kausel. Elements for the numerical analysis of wave motion in layered strata. *International Journal for Numerical Methods in Engineering*, 19(7):1005–1032, 1983. doi: 10.1002/nme.1620190706.

[113] J. C. F. Telles and C. A. Brebbia. On the application of the boundary element method to plasticity. *Applied Mathematical Modelling*, 3(6):466–470, 1979. doi: 10.1016/S0307-904X(79)80030-X.

[114] D. J. Thompson and C. J. C. Jones. A review on the modelling of wheel/rail noise generation. *Journal of Sound and Vibration*, 231(3):519–536, 2000. doi: 10.1006/jsvi.1999.2542.

[115] S. Timoshenko and S. Woinowsky-Krieger. *Theory of plates and shells*. McGraw-Hill, New York, April 1964. ISBN 978-0070858206.

[116] D. Torrent, D. Mayou, and J. Sanchez-Dehesa. Elastic analog of graphene: Dirac cones and edge states for flexural waves in thin plates. *Physical Review B*, 87(115143), 2013. doi: 10.1103/PhysRevB.87.115143.

[117] E. Volterra and J. D. Morell. Lowest natural frequencies of elastic hinged arc. *The Journal of the Acoustical Society of America*, 33(12):1787, 1961. doi: 10.1121/1.1908576.

[118] E. Volterra and J. D. Morell. Lowest natural frequency of elastic arc for vibrations outside the plane of initial curvature. *The Journal of Applied Mechanics*, 27(4):744–746, 1961. doi: 10.1115/1.3641794.

[119] E. Volterra and J. D. Morell. Erratum: Lowest natural frequency of elastic arc for vibrations outside the plane of initial curvature. *The Journal of Applied Mechanics*, 34(4):1046, 1961. doi: 10.1115/1.3607821.

[120] L. Wrobel. *The Boundary Element Method*, volume 1. Wiley, Chichester, West Sussex, England, March 2002. ISBN 9780471720393.

[121] Y. Xiao, J. wen, and X. Wen. Flexural wave band gaps in locally resonant thin plates with periodically attached spring–mass resonators. *Journal of Physics D: Applied Physics*, 45(19), 2012. doi: 10.1088/0022-3727/45/19/195401.

[122] Y. Xiao, J. wen, D. Yu, and X. Wen. Flexural wave propagation in beams with periodically attached vibration absorbers: Band-gap behavior and band formation mechanisms. *Journal of Sound and Vibration*, 332(4):867–893, 2013. doi: 10.1016/j.jsv.2012.09.035.

[123] Y. Zheng and X. Huang. Anisotropic perfectly matched layers for elastic waves in cartesian and curvilinear coordinates. *Earth Resources Laboratory Industry Consortia*, pages 1–18, 2002.